Simulation of a search for the narrow graviton resonance at the LHC

Mustafa Hussain
University of Oslo
May 2006
Thesis presented for the Cand. Scient. degree
in Experimental Particle Physics

Abstract

A number of theories including extra space dimensions predict massive graviton states. In some such models, like the Randall-Sundrum, the graviton states are well separated and can be detected by the ATLAS detector at the Large Hadron Collider. Only graviton resonances which are narrow compared to the experimental resolution are considered. The ability of the ATLAS detector to identify such resonances is studied. The mass discovery limit for the channels $G^* \to e^+e^-, \mu^+\mu^-$ and $\gamma\gamma$ are derived. Earlier studies in these channels are improved or corrected. Discovery limit for the detection of the decay mode $G^* \to \gamma\gamma$ is derived for the first time. The spin of the graviton resonances is studied through decay angular distributions.

Acknowledgements

First of all I wish to thank my supervisor Professor Farid Ould-Saada for accepting me as his student. During the work with this thesis he was always willing to answer questions and comment my work. Without his tremendous patience, inspiration and support survival would not have been possible.
I also wish to thank Dr. Sigve Haug, Dr. Børge K. Gjelsten, Dr. Samir Ferrag, Olav Mundal, Esben Lund, Katarzyna Pajchel, Marianne Johansen and Robindra Prabhu and all the current and former members of the Experimental Particle Physics group. Their support should not be underestimated.
A great thanks to Professor Jean Philippe Guillet, Professor Torbjorn Sjostrand, Dr. Thomas Binoth and Dr. Marc Escalier for helping me out from abroad whenever I was in trouble.
My friends outside the Physics Department should not be forgotten: Anders Svensson, Erling Outzen, Harald Nicolaisen, Johannes Wilm, Marit Mørch, Marte Jørgensen, Marte Nilsen, Mehran Raja, Peder Joakimsen, Ragna Lindboe, Sapideh Sadegi, Stephanie Reiler, Synøve Solhem, Tanja Askvik, Tonje Larsen, Trond Petter Sætrang and all the others who made life a little bit easier.
Finally, I express my thanks to all my family, especially my mother and father for their moral and financial support, and my sister, Fatima, who provided me with horror movies during the years. A special thanks to my cousin Mal, his wife Tracey and their kids for their hospitality and cheerful spirits.
The bonds I have made to all of you are made of a force infinitely stronger than any graviton, massive or not, can exert.

Introduction

The goal of particle physics is to understand, on a fundamental level, matter and the forces governing it. This understanding, aquired through collider or fixed target experiments, is made possible through technological development of the 20th century. Our knowledge of matter and the forces of nature is integrated into the Standard Model which consists of verified models, theories and discoveries from the last hundred years. Predictions of this theory are found in experiments throughout the world. The most important contribution to particle physics in the near future will be through the experiments at the Large Hadron Collider (LHC). Located at CERN[1] between Switzerland and France it is expected to be operative by 2007. The main goal is the search for the higgs-boson, the particle responsible for the introduction of mass in the Standard Model. However, a substantial effort will be made in the search for evidence of new theories going beyond the Standard Model. The Standard Model is not regarded as the complete description of elementary particles since it lacks, among others, the description of gravity. Also the Standard Model fails to explain why gravity is so weak compared to other forces of nature. This is referred to as the hierarchy problem of the weak-Planck scale. In 1999 Lisa Randall and Raman Sundrum proposed a model based on one extra spatial dimension and localized gravity. It solves the weak-Planck scale hierarchy via an exponentially suppressed warp factor in a five dimensional geometry. The most elegant feature of the model is its predictive powers through only two free parameters. This scenario can be regarded as a proper theoretical model, in the right sense of the term. This is not the case with other theories going beyond the Standard Model. The Minimal Super Symmetric Model (MSSM) has 5 free parameters. These are obtained through a series of assumptions in order to reduce the huge amount of free parameters. If the Randall Sundrum model is correct traces of massive graviton resonances are expected to appear. However other models predict graviton resonances as well. This thesis ignores the details of particular models and concentrates on an analysis that should apply to a large number of models predicting narrow graviton resonances that are well seperated in mass. Thus results derived in this thesis do not depend on the validity of a particular scenario and can be applied to any model with narrow graviton resonances. The Randall-Sundrum model is only used as a guide or as a test model.

The thesis is organized as follows: Chapter 1 introduces the Standard Model and the Randall-Sundrum model. Chapter 2 gives as overview of the detectors at the Large Hadron Collider. A more or less detailed description of the ATLAS detector is given, followed by a rapid introduction to the event generation and detector simulation pro-

[1] European Organization for Nuclear Research

grams used in this thesis. The goal is to establish the mass discovery limits of the gravitons and to discriminate them from other exotic resonances and the Standard Model background. Chapter 3 investigates the most promising channels for discovery. These consist of $G^* \to e^+e^-, \mu^+\mu^-$ and $\gamma\gamma$. A study of radiation effects is conducted in order to improve or correct earlier studies and results. The discovery limit for the $\gamma\gamma$ channel is derived for the first time. In the end the decay angular distributions are studied in order to discriminate the graviton resonances from background and/or other exotic particles. The angular distributions determine the spin of the gravitons. The conclusions and the outlooks for the future are given in Chapter 4.

Contents

Chapter 1

Theory

1.1 The Standard Model

The history of particles and their interactions is a long one. The idea of what the basic elementary particles in nature are has evolved during the centuries. Atoms and later protons and neutrons were viewed as the fundamental elementary particles of nature. Today we believe that quarks and leptons, which matter is made of, and the gauge bosons, which are responsible for the interactions between the matter particles, are the elementary particles of nature, i.e particles which do not have any substructure. These are incorporated in the Standard Model (SM).

Almost all particle physics is described by the SM, which is a relativistic quantum field theory. All particles are seen as excitations of fields. The SM is also almost in perfect agreement with present observations[1]. But there are some more fundamental weaknesses. Gravity is not incorporated into the SM. Gravity is much weaker compared to other SM interactions at the subatomic level. For instance the ratio between gravity and electromagnetic interactions is given by:

$$\frac{F_{gravity}}{F_{coulomb}} \sim \frac{\frac{G}{r^2}}{\frac{1}{\epsilon_0 r^2}} \sim 10^{-21} \tag{1.1}$$

where ϵ_0[2] and G[3] are the permittivity of free space and the gravitational constant, respectively. Gravity is thus ignored. But also the introduction of particle mass in SM is not well understood. These weaknesses are not only theoretical but also experimental. The introduction of particle mass in SM is related to the existence of a scalar particle, the higgs boson. And one assumes that gravity is governed by a massless particle, the graviton. None of these have ever been observed.

[1] The neutrinos which are massless particles in the SM do indeed have a tiny mass.
[2] The permittivity of free space is defined as: $8.85418782 \cdot 10^{-12} \mathrm{m}^{-3}\mathrm{kg}^{-1}\mathrm{s}^4\mathrm{A}^2$
[3] The gravitational constant is defined as: $6.67300 \cdot 10^{-11} \mathrm{m}^3\mathrm{kg}^{-1}\mathrm{s}^{-2}$

1.1.1 Fermions and Bosons

Elementary particles come in two types in the SM. The fermions, which are the building blocks of nature, are spin $\frac{1}{2}$ particles. The bosons, which are responsible for the interactions, have integer spin.

Quarks and leptons, which are fermions, are divided into three families each. Each family is written as a doublet. For leptons each doublet consists of a charged lepton and its corresponding neutral neutrino:

$$\begin{pmatrix} \nu_e \\ e \end{pmatrix} \quad \begin{pmatrix} \nu_\mu \\ \mu \end{pmatrix} \quad \begin{pmatrix} \nu_\tau \\ \tau \end{pmatrix}$$

The leptons have their anti-particles, which for the charged leptons have opposite additive quantum numbers, like charge. The quarks; down, up, strange, charm, bottom and top are set up in the same way:

$$\begin{pmatrix} u \\ d \end{pmatrix} \quad \begin{pmatrix} c \\ s \end{pmatrix} \quad \begin{pmatrix} t \\ b \end{pmatrix}$$

here u, c, t have charge of $\frac{2}{3}$e and d, s, b have a charge of -$\frac{1}{3}$e. Each of the quarks can be assigned a quantum number called colour; Red, Green and Blue. The quarks, like leptons, have their anti-particles, which have the same properties but opposite additive quantum numbers. The classification of fermions in doublets are due to $\mathbf{SU(2)_L}$ weak isospin symmetry which is discussed later. Each member of a family has the same value of isospin.

Particles which consist of three quarks or three anti-quarks are called baryons. Particles can also be made of a single quark and an anti-quark. These unstable particles are called mesons. Since both baryons and mesons interact strongly they are commonly known as hadrons.

Gauge bosons are the so-called force carriers in the SM. Interactions occur when bosons are exchanged between two particles, with a strength given by a coupling constant which is a function of energy transfer, Q^2, during the interaction. Theoretically, bosons appear when we require that the Lagrangian of the system, given by L=T-V, where T and V are the kinetic and potential energies of the system, is invariant under a local gauge transformation i.e. the physics should be the same even though the phase of the the wavefunction of the particles has changed. This is called Gauge Symmetry. The Lagrangian for quarks and leptons are invariant under global symmetry transformations. By requiring invariance under local symmetry transformations, the vector fields, interpreted as force carriers, are introduced as counter terms. The particle interactions in the SM are governed by local gauge symmetries. The model is built on the symmetries of the $\mathbf{SU(3)_C \times SU(2)_L \times U(1)_Y}$ group[4]. These symmetries imply the existence of

[4]U(n)-groups are unitary Lie groups with corresponding special unitary subgroups, SU(n), special in the sense that determinants in the fundamental matrix representation are one.

conserved currents and charges. The source of interaction is the conserved charge of the related symmetry of that interaction. The gauge groups in SM include:

• $\mathbf{SU(3)_C}$: A set of 3×3 matrices form the group $\mathbf{SU(3)_C}$ with corresponding eigenvectors which define the strong charge. The $\mathbf{SU(3)_C}$ symmetry governs strong intercations. The conserved charge is called colour. There are eight bosons called gluons, described by the fields A_a^μ, where a is a colour index running from 1 to 8. Each of the gluons have a colour and an anti-colour. The strength of the strong interaction is given by the constant $\alpha_s = \frac{g_s^2}{4\pi}$, where g_s is the strong coupling constant. Since α_s is asymptotic, it is large at low energies and vanishes at the limit $\alpha_s(Q \to \infty) \to 0$

• $\mathbf{SU(2)_L}$: The $\mathbf{SU(2)_L}$ gauge fields couple only to left-handed fermions, in order to incorporate parity violation. $\mathbf{SU(2)_L}$ consists of three fields: $W_1^\mu, W_2^\mu, W_3^\mu$. In addition this symmetry conserves a weak charge which is the third component of the weak isospin, I_3, defined as:

$$I_3 \equiv Q - \frac{Y}{2} \tag{1.2}$$

where Q and Y are the electric charge and the hypercharge, respectively.

• $\mathbf{U(1)_Y}$ is the hypercharge symmetry and the corresponding gauge neutral boson field is described by B^μ. The conserved charge, the hyper charge, is denoted by:

$$Y \equiv B + S + C + \tilde{B} + T \tag{1.3}$$

where B, S, C, $\tilde{B}$ and T are the baryon number, strangeness, charm, beauty and truth. The $\mathbf{U(1)_Y}$ group consists of phase transformations of the type $\mathbf{U}(\alpha) \equiv e^{i\alpha}$ and is an Abelian[5] group.

• $\mathbf{SU(2)_L \times U(1)_Y}$ is the symmetry group of the unified electromagnetic and weak interactions, called electroweak interactions. The strength of electromagnetic interactions, which are mediated by the photon, is given by $\alpha = \frac{e^2}{4\pi}$ where e is the electromagnetic coupling constant. The weak interactions, which are mediated by $W^\pm$ and Z^0, have a strength given by Fermi's constant $G_F = 1.167 \cdot 10^{-5}\ GeV^{-2}$. At unification the strength of the weak interactions become as strong as electromagnetic interactions. As a consequence of the electroweak unification the weak and electromagnetic interactions are described by the same formalism. The exchange of Z^0 and γ, at high enough energies, occurs at the same rate in neutral current processes, like the Drell-Yan process, $q\bar{q} \to \gamma^*, Z^0 \to l^+ l^-$.

1.1.2 Spontanous Symmerty Breaking

The manifeststation of two forces rather than one single unified is due to spontanous symmetry breaking of the $\mathbf{SU(2)_L \times U(1)_Y}$ symmetry group through the Higgs mechanism. Through this mechanism the massless gauge bosons given by the different gauge

[5]Multiplication of group members is commutative.

symmetries, except for gluons and photons, aquire mass. The neutral field W_3^μ from the $\mathbf{SU(2)_L}$ part mixes with B^μ from $\mathbf{U(1)_Y}$ giving rise to the massless photon, γ and the massive Z^0, while a mixing of W_1^μ and W_2^μ is identified as the massive $W^\pm$.

The Higgs field, which is introduced through the Higgs Mechanism, is a complex scalar field, denoted by a $\mathbf{SU(2)}$ doublet, with a non-zero vacuum expectation value. It has four degrees of freedom. The particles acquire masses by interacting with this field. Three of these freedoms generate the masses of the Z^0 and $W^\pm$ bosons. There remains a massive scalar with one degree of freedom after symmetry breaking which is identified as the higgs boson. The higgs boson has not been discovered and constitutes the only missing particle of the SM.

1.2 Extra Dimensions

A fundamental theory for particle physics is expected to describe all fundamental forces of nature. However the SM fails to describe the gravitational force, and hence cannot be a fundamental theory. In addition, in energy scales of order the Planck mass[6] or 10^{19} GeV, a theory of quantum gravitation is required. This shows that the SM needs to be replaced by an alternative theory at higher energy scales. Among the various theories beyond the SM some require extra spatial dimensions. Historically the concept of extra dimensions first appeared in 1914 when Gunnar Nordstrom [43] introduced a 5-dimensional electromagnetic potential to describe both electromagnetism and gravity. In 1919 Theodor Kaluza [43] constructed a similar unified theory. Oscar Klein [43] rediscovered and completed the theory in 1926, giving it a geometrical interpretation and finding charge quantization. The so-called Kaluza-Klein Excitations are now a common feature of the extra dimension theories. The idea of extra dimensions is used to address some of the unsolved issues in the SM. To mention a few [16]:

- The hierarchy problems
- Producing electroweak symmetry breaking without a higgs boson
- New Dark Matter candidates
- Neutrino masses

The hierarchy problems in particle physics relate to some huge mass scale differences which are difficult to explain. The difference in mass between the top quark and the electron is of order $\frac{M_{top}}{M_{electron}}$=3.5·$10^5$. The difference between the Planck scale and the electroweak scale is $\frac{M_{planck}}{M_W}$=10^{16}. The latter problem is translated into the question: Why is gravity so weak? At Planck scale gravity is as strong as the gauge interactions of the Standard Model. Several solutions have been offered. Lisa Randall and Raman Sundrum gave answer to this question through their Randall-Sundrum model(RS) which has one small extra dimension [15]. Before going into details we look at the Kaluza-Klein towers.

[6]The Planck mass is the natural unit of mass, defined as: $\sqrt{\frac{1}{G}}$, where G is the gravitational constant.

1.2.1 Kaluza-Klein Excitations

In the Kaluza-Klein theory an extra spatial dimension is compactified on a circle at every point in space-time, in order to 'hide' it. This is not surprising since this dimension is not observed. The concept of compactification is better understood by looking at a particle in a box with a length πL, a situation where the potensial is zero for $0 \leq y \leq \pi L$, and infinite elsewhere [16]. The solution is written as $\psi \sim Ae^{ipx} + Be^{-ipx}$. Since the physical region is of a finite size it is called compact [16]. Using the boundry conditions $\psi(0) = \psi(\pi L) = 0$ the particle momentum becomes p=$\frac{n}{L}$, with n as an integer i.e. the particle momentum is quantized. This gives rise to a solution of the form $\psi \sim e^{\pm\frac{in}{L}}$. This is analogous to the finite extra dimension in the Kaluza-Klein theory, but it has different boundry conditions since it is compactified on a circle [16].

A fifth dimensional massless scalar field $\phi(X)$, which is periodic because of the extra dimension i.e. $\phi(X^\mu, y)$=$\phi(X^\mu, y + 2\pi nR)$, where μ = 0,1,2,3, gives the space-time dimensions, y is the fifth dimension with radius R and n is an integer, is expanded in Fourier modes:

$$\phi(X^\mu, y) = \sum_{n=-\infty}^{n=\infty} \phi_{(n)}(X^\mu) e^{\frac{iny}{R}} \tag{1.4}$$

The Fourier expansion gives an infinite set of four dimensional fields $\phi_n(x)$ called Kaluza Klein modes. Imposing the 5. dimensional Klein Gordon equation, $\partial_A \partial^A \phi = 0$ where $\partial_A \partial^A$ is the fifth dimensional D'Alembertian operator, yields:

$$\partial_A \partial^A \phi = g^{AB} \partial_A \partial_B \phi = (g^{\mu\nu} \partial_\mu \partial_\nu \phi + g^{yy} \partial_y \partial_y)\phi = 0 \tag{1.5}$$

where $g^{\mu\nu}$ is the metric tensor. Operating in flat space the components of g^{AB} are given by $g^{\mu\nu} = \eta^{\mu\nu}$ which is the Minkowski metric, and g^{yy}=-1. Orthogonal fields yield:

$$(\partial_\mu \partial^\mu + (\frac{n}{R})^2)\phi_n = 0 \tag{1.6}$$

for each mode ϕ_n. Each ϕ_n has a fixed momentum, p=$\frac{n}{R}$. This equation is the Klein-Gordon equation for a massive scalar. In other words the fifth dimensional field manifests itself as a infinite tower of states with increasing masses in four dimensions. The masses are given by:

$$E^2 = (\frac{n}{R})^2 + \mathbf{p^2} \tag{1.7}$$

where $(\frac{n}{R})^2$ is the mass of the n^{th} Kaluza Klein mode.

1.2.2 The RS model

The RS model assumes only one extra dimension. The fifth dimension, denoted by y, is compactified on a circle S^1 with radius r_c . The points y=-πr_c and y=π_r are the same i.e. there are periodic boundary conditions [16]. By demanding that the fields remain the same under the parity operation y→ -y, together with the translation y→ y+$2\pi r_c$, only two points remain invariant: y=0, πr_c. These are called the fixed points. This symmetry is denoted by Z_2. The total symmetry of the extra dimension is denoted by S^1/Z_2.

There are two branes in the set up. The branes are located at the fixed points. The brane at y=0, is the 'hidden' Planck brane with Planck scale, and the TeV or SM brane, is at y=πr_c. While SM particles and forces are confined to the TeV brane[7], gravity can exist everywhere. The branes are connected by y. This is reflected in the metric, which is based on a slice of a space with negative curvature, called Anti-de Sitter:

$$ds^2 = e^{-2kr_c\phi}\eta_{\mu\nu}dx^\mu dx^\nu - r_c^2 d\phi^2 \tag{1.8}$$

where k is the curvature parameter, $\eta_{\mu\nu}$ is the Minkowski metric and ϕ is the coordinate of the extra dimension, thus y=ϕr_c. The metric, as the geometry, is called non-factorizable because the four dimensional space-time is dependent on y. The effective four dimensional Planck mass, the so called reduced Planck mass is given by:

$$\bar{M}_{pl}^2 = \frac{M^3}{k}(1 - e^{-2kr_c\pi}) \tag{1.9}$$

where M is the fifth dimensional Planck mass. The reduced four dimensional Planck mass is derived from the five dimensional paramenters r_c, k, M. Because of the smallness of the exponential, $\bar{M}_{pl}$ depends weakly on r_c when kr_c is large. This means that $\bar{M}_{pl}$, M and k are of same order. So there is no fine-tuning. In addition k is smaller than M since the 5 dimensional curvature is small compared to M in the non-quantum limit [24]. This implies constraints on the ratio given by [24]:

$$0.01 \leq \frac{k}{\bar{M}_{pl}} \leq 0.1 \tag{1.10}$$

This is the first free parameter in the RS Model.

For a massive scalarfield on the visible TeV brane, following action yields:

$$S_{vis} = \int d^4x\sqrt{|g|}(g^{\mu\nu}\partial_\mu\phi\partial_\nu\phi - M^2\phi^2) \tag{1.11}$$

here $\sqrt{|g|} = e^{-4ky}$, where g is the determinant of the matrice, $g^{\mu\nu} = e^{2ky}\eta^{\mu\nu}$. This yields:

[7] At TeV scale the SM breaks down.

$$S_{vis} = \int d^4x e^{-4ky}(e^{2ky}\partial_\mu\phi\partial^\mu\phi - M^2\phi^2) \tag{1.12}$$

By rescaling the field, $\phi \to e^{ky}\phi$, the action becomes:

$$S_{vis} = \int d^4x \partial_\mu\phi\partial^\mu\phi - m^2\phi^2 \tag{1.13}$$

where m=e^{-ky}M is the mass measured on the TeV brane. If $e^{-ky} \simeq 10^{-15}$ then m$\simeq$ 1 TeV and hierarcy is reproduced between the Planck scale and the electroweak scale. There are no longer two fundamental scales, but only one, the fifth dimensional Planck scale, which the warp factor generates TeV scales from. But what about the gravitons? How will they look in this model? Gravitons are spin-2 particles and their fields are not given by scalarfields. But it turns out that their masses and wave functions are identical to the case of a scalar field in the RS bulk since they yield the same equation of motion [16]. Thus using a scalarfield in the bulk shows how gravitons look like in the RS model [16]. What is required is the fifth dimensional Klein-Gordon equation in a curved space. This equation falls out by varying the action i.e. requiring that small variations do not lead to changes of first order in the action:

$$S = \frac{1}{2}\int d^5x\sqrt{|g|}(g^{AB}\partial_A\phi\partial_B\phi - M^2\phi^2) \tag{1.14}$$

$$\delta S = \int d^5x\sqrt{|g|}(g^{AB}\partial_A\phi\partial_B\delta\phi - M^2\delta\phi) = 0 \tag{1.15}$$

Integration by parts yields:

$$\delta S = -\int d^5x[\frac{\partial_B}{\sqrt{|g|}}(\sqrt{|g|}g^{AB}\partial_A\phi) + M^2\phi]\sqrt{|g|}\delta\phi = 0 \tag{1.16}$$

$$\Rightarrow \frac{\partial_B}{\sqrt{|g|}}(\sqrt{|g|}g^{AB}\partial_A\phi) = 0 \tag{1.17}$$

when the mass of the field is set to zero. With $\sqrt{|g|} = e^{-4ky}$, where g is the determinant of the matrice g^{AB}, $g^{\mu\nu} = e^{2ky}\eta^{\mu\nu}$, $g^{yy} = -1$, the expansion of the field in Fourier modes yields:

$$-e^{2ky}\partial_y(e^{-4ky}\partial_y\chi_n) = m_n^2\chi_n \tag{1.18}$$

The wave functions χ_n are linear combinations of the J_2, Y_2 Bessel functions and not sines and cosines as was the case with flat space. Equation 1.6 is reproduced by setting the curvature parameter equal to zero. The masses of KK states of gravitons are given by:

$$m_n = x_n k e^{-kr_c\pi} \tag{1.19}$$

x_n are roots of the Bessel function $J_1(X_n)$, where the first excitation is given by x_1=3.83.

m_n is the second basic parameter in the RS Model. Theoretically, for a fixed value of m_n for some excitation, $\frac{k}{\bar{M}_{pl}}$ completely determine all properties in the RS model. The widths of the gravitons are proportional to a dimensionsless coupling $\sqrt{2}x_n k/\bar{M}_{pl}$. While the cross-sections are proportional to $(k/\bar{M}_{pl})^2$. Experimenatlly, all fundamental model parameters are completely determined by the measurement of the mass and the width of the graviton excitations. The RS model is thus highly predictive.

The interaction of the massive gravitons with the SM-fields is given by [16]:

$$\mathcal{L}_{int} = -(\frac{G_0^{\mu\nu}}{\bar{M}_{pl}} + \sum_{n>0} \frac{G_n^{\mu\nu}}{\Lambda_\pi})T_{\mu\nu} \tag{1.20}$$

where $T_{\mu\nu}$ is the energy-momentum tensor and $\Lambda_\pi = e^{-kr_c\pi}\bar{M}_{pl}$.

The zero mode field $G_0^{\mu\nu}$ is massless and is supressed, see equation 1.20, by a factor $\bar{M}_{pl}$. This is why gravity is so weak. The excited modes $G_n^{\mu\nu}$ are the massive gravitons and they are only suppressed by a factor of Λ_π, which is of order 1 TeV. Thus massive gravitons interact or couple stronger than the massless graviton. But more important is the fact that the massive gravitons can be directly produced at the Large Hadron Collidor(LHC) which have a centre of mass energy of 14 TeV. The massive gravitons are resonances i.e. particles which are too shortlived to be directly observed in the ATLAS detector at LHC. Their existence must be inferred from the particles they decay into. This thesis looks at the channels G*$\rightarrow e^+e^-, \mu^+\mu^-, \gamma\gamma$.

Only the first excited massive graviton, which is given by equation 1.19 for x_n=3.83, is considered. Before moving on to the analyses of these channels we take a look at the ATLAS detector where these discoveries are expected to be made.

Chapter 2

Experiment

2.1 LHC

The Large Hadron Collider (LHC) at CERN is a circular proton-proton collider with a center of mass energy ($\sqrt{s}$) of 14 TeV. 2835 bunches of protons, with each bunch containing $n_b = 10^{11}$ protons are used. The time interval between each colliding bunch is 25 ns. This gives a bunchrate, or a collisions rate, of 40 million per second or 40 Mhz. The number of collisions per square centimeter per second is given by $\mathcal{L} = 10^{34} cm^{-2} s^{-1}$, called the luminosity. The LHC is expected to reach this high luminosity after three years of running.

Since protons have substructure and consist of quarks and gluons, which are commonly named partons, the hard collision is not between the two incoming protons as whole but between the partons. Each of the partons carries a fraction of the proton momentum. Thus the energy available in the collisions are given by $x_1 x_2 \sqrt{s}$ where x_1 and x_2 are the fraction of the proton momentum carried by the two incoming partons. So the effective center of mass energy is lower than 14 TeV but this is still sufficient in our search for massive gravitons.

To achieve energies of 7 TeV the protons go through a complex system of accelerators at CERN (Fig. 2.1) where they are accelerated by strong electric fields and bent and focussed by magnetic fields, before the Super Proton Synchrotron (SPS) accelerates them to 450 GeV, and injects them into the LHC ring in both directions. Here they are accelerated up to 7 TeV. Large magnetic field are required to bend 7 TeV protons. To achieve this goal superconducting dipoles, at a temperature of 2 K, provide a magnetic field of 8 Tesla.

There are four LHC experiments with corresponding detectors, located at points where the protons collide. The largest of these detectors, ATLAS (Fig. 2.2) and CMS, are multi purpose detectors. The two smaller ones, LHCb and ALICE, are specifically built for B-physics and heavy ion physics, respectively.

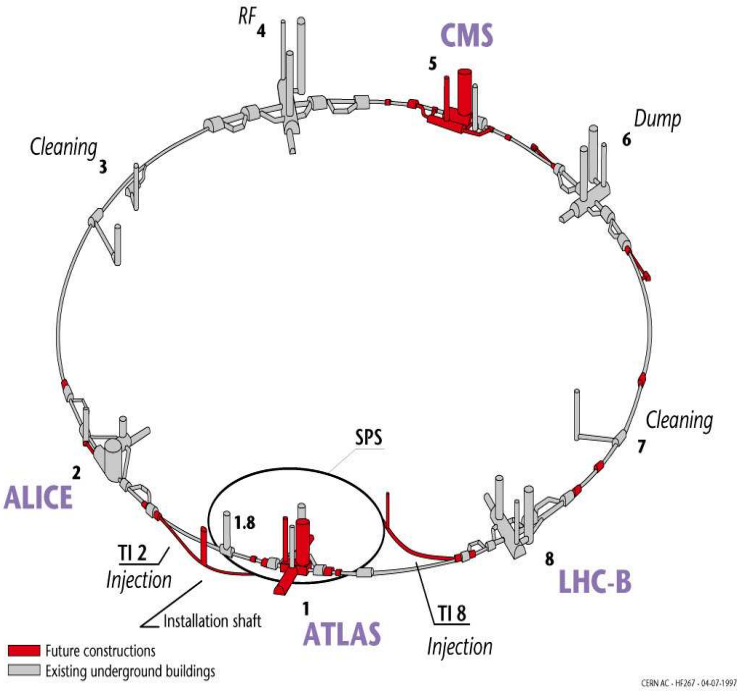

Figure 2.1: The LHC underground accelerator setup at CERN.

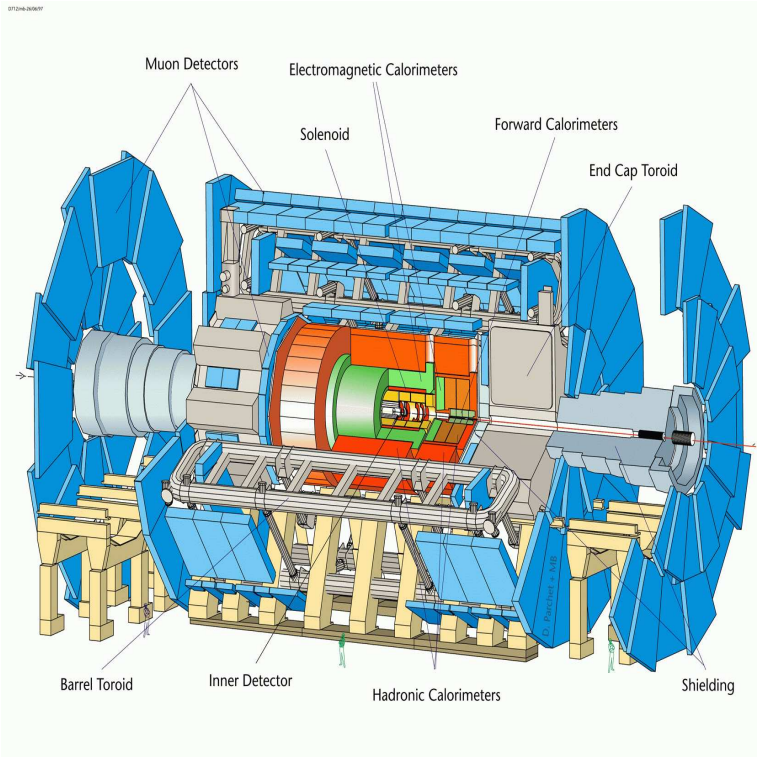

Figure 2.2: The ATLAS detector.

2.2 The ATLAS detector

The purpose of the ATLAS detector, which stands for **A** **T**orodial **L**HC **A**pparatu**S**, is to reconstruct the physical events that happen when the protons collide. Then comparison is made with some theoretical framework including theories which go beyond the SM. Collisions have an event rate given by N= Lσ, where L is the integrated luminosity and σ is the cross section. For a given luminosity the cross section is measured and compared to different theories. In order to do that the detector has to identify each particle and measure its energy and momentum, and be able to seperate particles in space and time in order to determine the associated event. In most cases the particles which are produced are not the ones that are reconstructed by the detector because they have too short lifetime. When a heavy particle like the graviton is created it decays rapidly into other stable particles which are detected by the detector, e.g. the process where the graviton decays into leptons in final state, G*$\rightarrow e^+e^-$. The particle we want to study is called the signal. A hard collision occurs when two partons with the largest fraction of the original proton momentum collide. But the decay of the heavy particles is accompanied by other SM decays or processes which dilutes the decay of the particle we want to study. These processes come from collisions that are hard and collisions that are not. Because of combinatorics the signal signature is not always unique and one encounters processes in the final state that can mimic G* $\rightarrow e^+e^-$. Processes which have the same signature as the signal are called background. A major task of detectors in particle physics is to seperate or discriminate signal and background. The main concern is the background from strong interactions with large cross sections which dominate the high P_t [1] events. As shown later on this is not a huge problem in the search for gravitons in the different leptonic and photonic channels considered.

Because of the complexity of the events ATLAS consists of different parts, each with a specific task. The main parts consist of the Inner tracking Detector, the calorimeters and the Muon Spectrometer. All of them consist of smaller more specialized and complementary detectors.

2.2.1 Coordinates

We need a well defined coordinate system in order to describe the events in the detector in the most exact way. The z-axis of the ATLAS detector is defined by the x and y-directions. The x-axis points to the center of the ring from the interaction point and y-axis points upwards. The azimuthal angle ϕ is measured around the z-axis and defined by the components of the momentum in the x-y plane: tan$\phi \equiv \frac{p_y}{p_x}$. The polar angle θ is the angle between the particle direction and the z-axis. The pseudorapidity is defined as: η=-ln tan$\frac{\theta}{2}$. The pseudorapidity says something about where the events happen in the detector. At ATLAS when the events fully occur inside the detector the pseudorapidity is given by -2.5<η<2.5. The events are said to be inside the acceptance or the geometry of the detector. The pseudorapidity is a good approximation of the true rapidity, given

[1] The transverse momentum is defined as the momentum projection perpendicular to the beam axis z: $P_t = \sqrt{p_x^2 + p_y^2}$

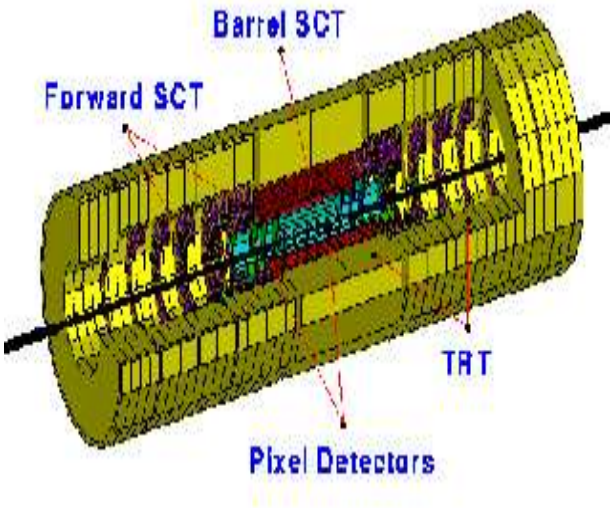

Figure 2.3: The Inner detector

by the energy and z-component of momentum of the particle: Y=$tanh^{-1}(\frac{p_z}{E})$, when the particle mass is not known.

2.2.2 The Inner Detector

The Inner detector (ID), see figure 2.3, which is the closest detector to the beampipe, is contained in a 7 m long cylinder of radius 1.5 m. It has the following main tasks: Electron identification, measure vertices and the momentum of charged particles, which is obtained from the curvature of their tracks in a magnetic field of order 2 Tesla created by a solenoid. The Inner detector consists of 3 subdetectors. The Pixel Detector, the SemiConductor Tracker (SCT), and the Transition Radiation Tracker (TRT).

Pixel detector

This subdetector lies closest to the beampipe and consist of three barrels situated at 5, 9 and 12 cm from the beampipe, respectively. It has 140 milion 50 $\mu m \times$ 400 μm pixels and provides high precision measurement close to the interaction point, but provides only three measurement for each track.

SemiConductor Tracker

The barrel Semi Conductor Tracker provides eight precision measurements per track, contributing to the momentum, impact parameter, and vertex position measurements, in addition to providing good pattern recognition by the use of high granularity. The SCT uses layers of silicon microsstrip detectors and consists of four barrels (Fig. 2.5). The

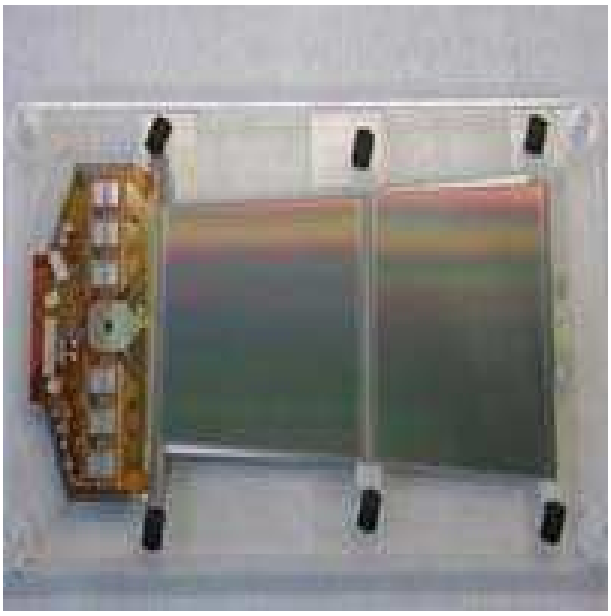

Figure 2.4: The SCT module.

SCT module (Fig. 2.4) consists of two pairs of four 6.36 × 6.40 cm^2 silicon detectors. The end-cap pairs are glued back to back. In order to cover the whole acceptance nine wheels with layers are situated on each side of the barrel.

The pixel and the SCT subdetectors provide high precision measurements and are reffered to as the Precision Trackers.

Transistion Radiation Tracker

The Transition Radiation Tracker (TRT) uses gas filled straw detectors which are 4 mm in diameter. Each straw detector consists of a wire in the center of the gas volume (Xe, CO_2, and O_2), which serves as an anode, and a cylinder as a cathode. Drifting charges are picked up when a charged particle ionises the gas. The TRT provides a large number of measurements, usually 36, on every track. This allows continous tracking and provides a good pattern recognition. Xenon gas gives the detector electron identification capabilities. This is because xenon gas is good for detecting Transition Radiation (TR) photons created by electrons.

The discrimination between tracking hits and TR hits is achieved through two independent thresholds, corresponding to high and low energy deposit in the straws.

Transition Radiation is emitted when a charged particle passes suddenly from one medium to another with different dielectric properties. In TRT this emision happens in plastic layers between the straws. TR energy is inversally proportional to the mass of the charged particle[2]. Because of their small mass TR is only significant for high energetic e^+ and e^-. This gives higher deposition of energy in the straws than tracking

[2]The TR energy is given by: $W \sim \sqrt{\frac{1}{m}}$

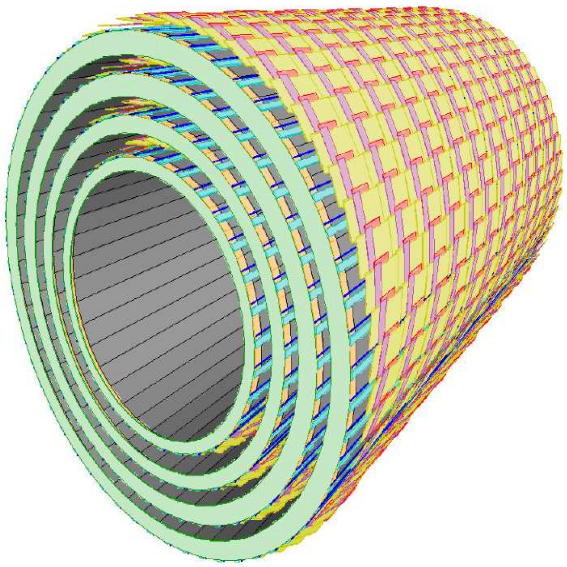

Figure 2.5: The SCT barrel covered with SCT modules.

hits. Thus the TR photons pass the higher threshold while the tracking hits pass the lower one.

2.2.3 The Calorimeters

The ATLAS detector has two calorimeters which have different tasks (Fig.2.7). The Electromagnetic (EM) calorimeter measures the electron, positron and photon energies. The hadronic calorimter measures the energy of hadrons, such as charged pions.

The Electromagnetic Calorimeter

The EM calorimeter (Fig. 2.6) is a sampling calorimeter which consists of accordion shaped layers of lead (absorber material) and Liquid Argon (active material). The energy collected in Liquid Argon (LAr) is measured. The accordion geometry provides complete ϕ symmetry and coverage.

When electrons and positrons hit the absorber plates, electromagnetic (EM) showers, are created through pair production, $\gamma \rightarrow e^+e^-$, and bremsstrahlung $e \rightarrow e\gamma$. These secondary particles then enter into LAr which is ionised. After some radiation lengths[3] the EM showers are contained and the energy of the electrons is measured.

The EM calorimeter consists of a barrel part ($|\eta|<1.475$) and two end-caps ($1.375<|\eta|<3.2$).

The barrel of the EM calorimeter, which is contained in a crystat surrounding the ID, consists of two half barrels. Each end-cap calorimeter is contained in an end-cap cryostat, and is divided into two coaxial wheels.

[3] A radiation length is defined as the thickness of a material for which the particle energy is reduced by a factor of $\frac{1}{e}$.

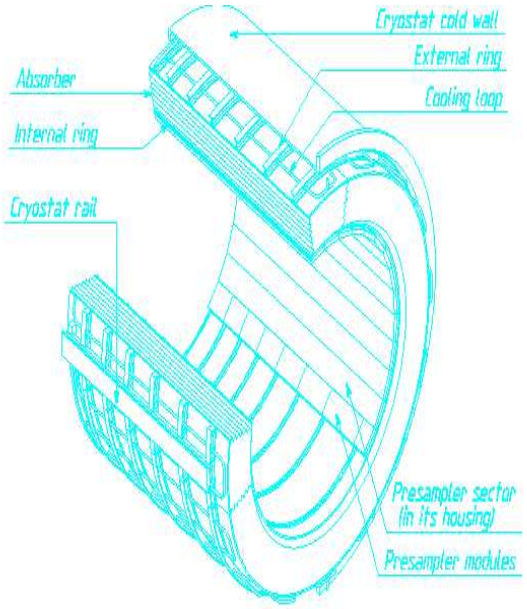

Figure 2.6: The general layout of the EM calorimeter.

The region $|\eta|<2.5$, of interest for our $G \to e^+e^-, \gamma\gamma$ studies, is devoted to precision physics. Here the EM calorimeter is divided into three longitudinal sections, the pre-shower, the pre-sampler and pre-amplifier. The strip section acts as a 'pre-shower' detector, enhancing particle identification and providing a precise position in η. Before particles enter the EM calorimeter they traverse material in ID and cryostats, thus suffering energy loss. At $|\eta|<1.8$ presamplers are placed to correct for the energy lost by the particles, making the energy measurement as accurate as possible.

The Hadronic Calorimeter

The Hadronic calorimeter is, like the EM calorimeter, a sampling detector with active and absorber material. The barrel calorimeter at $|\eta|<1.7$, also called the Tile calorimeter, is made of three sampling layers. It uses iron as obsorber material and plastic scintillating tiles as active material, and is thus a scintillation detector[4]. The 3 mm tiles provide two read out channels on both outer sides via optical fibers and photomultipliers. The Hadronic End-Caps (HEC) at $1.5<|\eta|<3.2$ and the Forward Calorimeter(FCAL) at $3.2<|\eta|<4.9$ are designed to tackle the higher radiation at high rapidity regions. LAr is used as active material instead of scintillators. The HECs, consist of four sampling layers and use copper plates as absorbers. The FCAL consists of three sampling layers. One is made of copper and two of tungsten.

The task of the Hadronic calorimeter is to measure energies of particles like pions and kaons which give rise to hadronic showers. The thickness of the hadronic calorimeter is important due to the fact that it is hard to contain hadronic showers, and it is important

[4]Scintillation detectors consists of material, both organic and inorganic, which emit light when traversed by charged particles.

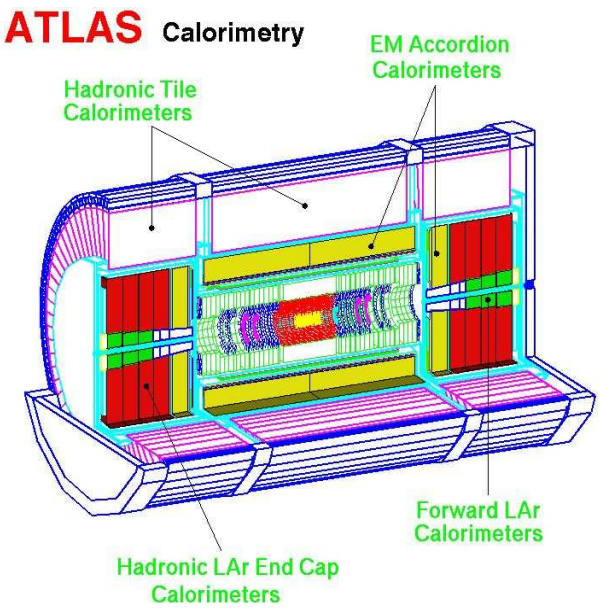

Figure 2.7: The ATLAS calorimetry.

to reduce leakage into the muon system. Because of this the absorption length[5] of the calorimeter is λ=11 at $|\eta|$=0, where 10λ is active material. This gives good resolution for high energy jets. Large pseudorapidity coverage is important in order to measure missing transverse momemtum of events i.e. transverse momentum of particles which escape detection.

2.2.4 The Muon Spectrometer

The Muon Spectrometer is designed to measure muon momentum. This requires the bending of the muon tracks, achieved by the Muon Toroidal Magnets. The tracks are bent by the barrel toroid at $|\eta|<1.0$, and by the end-cap magnets at $1.4\leq|\eta|\leq2.7$. At the transistion region, $1.0\leq|\eta|\leq1.4$, the tracks are bent by a combination of barrel and end-cap fields.

High precision track measurement is needed in order to determine the muon momentum. The tracking system consists of Monitored Drift Tube (MDT) chambers, located in the barrel region and in the end-caps, and Cathode Strip Chambers (CSC), located close to and around the beamline.

Each MDT consists of aluminium tubes filled with Argon and CO_2. Each tube has central a anode wire. The CSC are multiwire chambers with shorter response time and cathode strip read out. All chambers combined provide almost complete coverage of the pseudorapidity range $0<|\eta|<2.7$. All muons pass through three chambers.

The Muon Spectrometer is complemented with an independent Trigger system, covering the range $|\eta|<2.4$. The trigger system consists of Resistive Plate chambers located in

[5] λ is the mean distance a particle travels in the material without suffering collision.

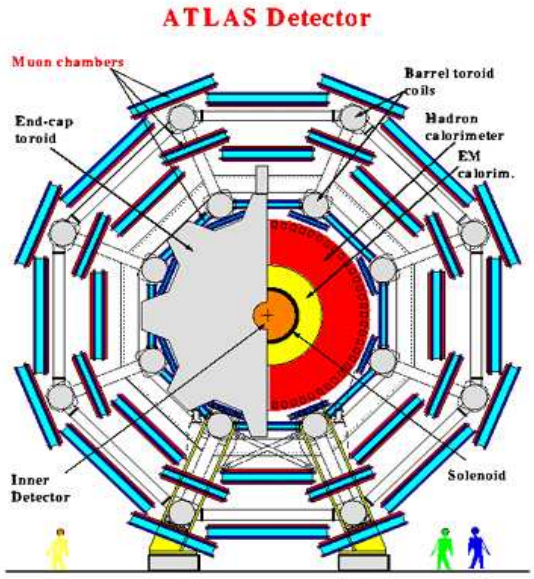

Figure 2.8: The Muon Spectrometer surrounding the rest of the detector.

the barrel region and Thin Gap Chambers located at the end-caps. Each muon passes through three trigger chambers.

2.2.5 The Trigger

A huge amount of interactions cause an enormous data-flow. The bunch crossing rate of 40 MHz gives rise to 10^9 interactions every second at high luminosity. The storage capacity is about 100 events per second. To reduce this huge amount of data ATLAS has a fast and efficient trigger system. The ATLAS Trigger is based on three levels of event selection.

Level 1: This hardware trigger looks for high P_t electrons, photons, jets and τ-leptons as well as large total E_T and E_T^{miss}. The surviving events pass into the level 2 trigger. The event rate is reduced to 100 kHz.

Level 2: At this level (software trigger) information provided by level 1 is used, and more events are rejected. Higher P_t cuts are applied which reduce the event rate to 1 kHz.

Level 3: The level 3 trigger, also called the Event Filter, reconstructs the event. Complex algorithms and more cuts are added and one arrives to an event rate of 100Hz which we can permanently store. Thus only 100 interesting events per second are selected out of 1000 million others.

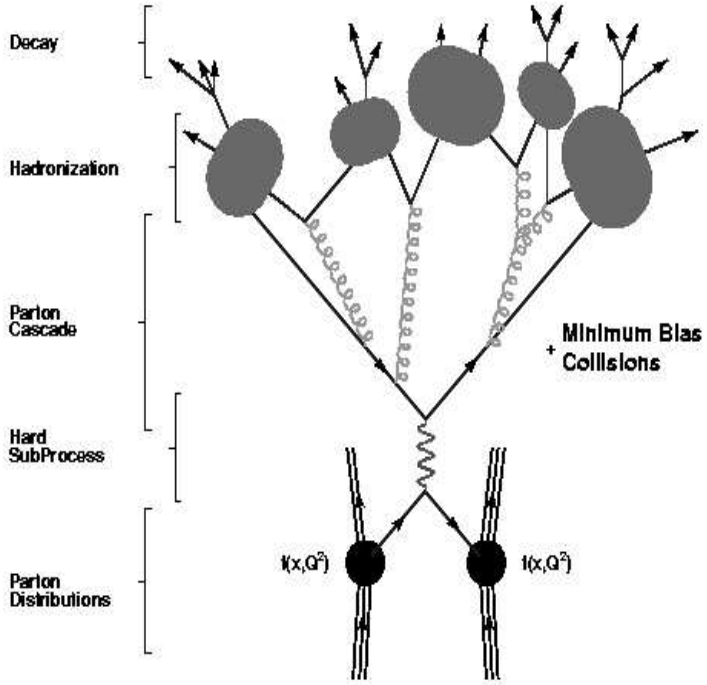

Figure 2.9: The basic structure of a generated proton-proton event in PHYTIA and HERWIG.

2.3 Generation and Simulation Tools

Computer simulations are important. They allow us to study and make predictions about physics in the SM and beyond. They play a major part in the preparations for the Large Hadron Collider, allowing study of the physics processes before the experiment starts.

2.3.1 Event Generators

Event generators are used to mimic physics processes before experimental data are available. They are designed in accordance with the idea in figure 2.9. The event generators starts with the hard subprocess, usually a 2→2 scattering process. Two incoming partons are selected, with energies and momenta distributed according to Parton Distribution Functions[6] (PDF). Higher order effects are added using parton showers. This causes the partons to split into pairs. After a parton cascade the partons are hadronized, and the unstable hadrons are decayed further into stable particles.

PYTHIA [3] and HERWIG [34] are Monte Carlo event generators commonly used for lepton and hadron collisions at leading order (LO). DIPHOX [13] is a 'parton event

[6]A PDF is a parametrization of the energy and momentum distribution shared by the partons in the hadron.

generator' without hadronization. DIPHOX calculates cross-sections at LO and next to leading order (NLO) for processes with hadrons and photons the in final state.

2.3.2 Detector Simulation

A program called ATLFAST [36] is used for simulation of the ATLAS detector in a parametrised way. It reproduces as well as possible full simulation results given by detector simulation programs like ATLSIM. Full simulation is comparable to the real detector in every detail. However full simulation is time consuming unlike ATLFAST which is used for fast simulation. But fast simulation lacks the accuracy of the full simulation. ATLFAST is reasonable to use when speed is demanded rather than accuracy, as is the case in this feasability study. Obtaining discovery limits for gravitons demands a huge amount of simulated data. Consequently ATLFAST is used for detector simulation in this study.

In ATLFAST the energy of the generated particles is assigned to calorimetric cells in the η and ϕ range, forming clusters. Next, ATLFAST identify the clusters. Particles are identified and subsequently their 4-momenta are smeared according to the expected and measured resolution. The smeared particles are then required to satisfy basic acceptance criteria. For each electron and photon this criteria is $|\eta|<2.5$ and $P_t > 5$ GeV. Muons have no associated clusters and are required to satisfy $|\eta|<2.5$ and $P_t > 6$ GeV. In order to isolate the lepton and photon clusters a certain distance to other clusters is required. The distance to other clusters is defined as:

$$\Delta R = \sqrt{\Delta\eta^2 + \Delta\phi^2} \tag{2.1}$$

and is set to $\Delta R>0.4$. In addition E_t deposited in a cone $\Delta R<0.2$ around the particles cannot exceed 10 GeV. Leptons and photons satisfying these cuts are reconstructed. The remaining clusters constitute the jets if they satisfy the criteria $|\eta|<5$ and $P_t > 15$ GeV. These are smeared according to the expected hadronic resolution.

Chapter 3

Analysis and Results

The discovery potential of the graviton is analysed in this chapter through the three channels $G^* \rightarrow e^+e^-, \mu^+\mu^-, \gamma\gamma$. To discover the graviton we need signal and background discrimination. The Randal Sundrum model provides very clear signals, which in real experiments lay above some background which has to be described. Signals and related backgrounds are generated using the PYTHIA generator, while ATLFAST is used for simulating the detector response. The signal and background are fitted with appropriate functions used to extract the information that is needed in the study. The main goal is the establish the discovery mass limit in the decay modes.

However, discriminating the signal from the background only indicate that a resonance, like the graviton or Z', has been discovered. Spin measurement is crucial to confirm the existence of the graviton. In this thesis the spin is studied through the angular distributions of the decay products of the graviton.

The analysis starts with the dielectron decay mode in section 3.6 - 3.7. The dimuon and diphoton channels are analysed in section 3.8 and 3.9 respectively. The analysis rounds off with graviton discrimination in ATLAS in section 3.10.

3.1 The Channels

Graviton resonances, which are unstable excited particles, cannot be directly observed. The graviton resonances can decay through different channels e.g. $G^* \rightarrow e^+e^-$. The graviton is produced from the following hard processes,

$$\begin{array}{ll} \text{quark annihilation :} & q\overline{q} \rightarrow G^* \\ \text{gluon fusion :} & gg \rightarrow G^* \end{array} \tag{3.1}$$

followed by the graviton decay into e^+e^-, $\mu^+\mu^-$, $\gamma\gamma$ or other stable or non-stable particles [5]. The $q\overline{q}$ annihilation and gg fusion are included in PYTHIA by setting the parameter ISUB= 391, 392 respectively. The branching ratios vary with graviton mass, but at large masses the ratios become constant. The graviton decay is dominated by QCD jets from $q\overline{q}$ and gg. These constitute 71% of the total decay rate. These channels have a large

Decay mode	BR(%)
$G^* \to q\overline{q}$	38
$G^* \to gg$	33
$G^* \to W^+W^-$	8.9
$G^* \to Z^0Z^0$	4.5
$G^* \to \gamma\gamma$	4.1
$G^* \to e^+e^-, \mu^+\mu^-, \tau^+\tau^-$	6
$G^* \to \nu_e\overline{\nu}_e, \nu_\mu\overline{\nu}_\mu, \nu_\tau\overline{\nu}_\tau$	6

Table 3.1: Branching ratios for graviton decay.

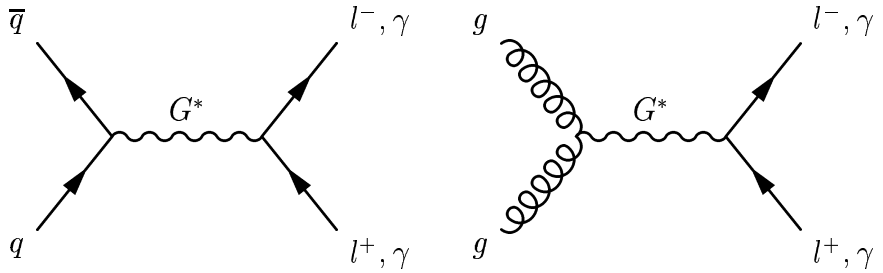

Figure 3.1: The processes for graviton resonance production used in this analysis.

background contribution from QCD multi-jet. The large background makes it very hard to make a discovery of the graviton. The W^+W^- and Z^0Z^0 decay modes, with a combined branching ratio of 13.4%, have similar problems. The W^+W^- channel has a branching ratio of 8.9%. These are best detected when one W decays leptonically into the electron or muon final states, and one hadronically [5]. This channel is contaminated by a large background from $t\bar{t}$ and W+2 jets. The Z^0Z^0 bosons are best detected in a decay mode with two leptons and two jets in the final state. This channel is dominated by a background from Z+2 jets. Consequently these channels are not useful for discovery but rather good in confirming the universality of the graviton [5] and determing its spin. Measurements of the graviton coupling in these channels were studied in reference [5]. This is beyond the scope of this study. The large standard model background from QCD jets makes it hard to observe the $\tau^+\tau^-$ decay. This leaves us with three channels where discovery is expected: $G^* \to e^+e^-, \mu^+\mu^-$ and $\gamma\gamma$. Branching ratios of the graviton are given in table 3.1.

3.2 Experimental Constraints

Constraints on the Randall-Sundrum model and its channels are set by collider experiments, like Tevatron [30]. The Tevatron is, at the moment, the world's most powerful particle accelerator, colliding protons and anti-protons. At Run II, which started in 2002

and is still going on, the center of mass energy is $\sqrt{s}$=1.96 TeV. The goal is to obtain 15 fb^{-1} of integrated luminosity by the year 2008. The Tevatron already accumulated $\sim$350 pb^{-1} of integrated luminosity in 2004 and $\sim$1 fb^{-1} in 2005.

Run II data corresponding to integrated luminosities of 345 pb^{-1} and 200 pb^{-1} were analyzed by the **C**ollider **D**etector at **F**ermilab (CDF) [31] and the DØ detector [44] in the search for resonances in the photon and lepton channels. The pairs of photons, electrons and muons were required to have E_T>15 GeV, E_T>25 GeV and E_T>20 GeV, respectively, in addition to other specified cuts, depending on the detector or the channel. See reference [32] and [45].

The lack of excesses in Drell-Yan and diphoton events confirms the SM predictions. For the CDF analysis figure 3.2 shows that the expected Drell-Yan production in the dielectron decay mode, generated by PYTHIA, is in agreement with the Tevatron data. The Drell-Yan background lies above the background originating from $t\bar{t}$ events, QCD dijet background and the background stemming from electroweak processes: $Z \rightarrow \tau\tau$, WW, WZ. Note the characteristic Z^0 peak at 91 GeV. The data were used to constrain the Randall-Sundrum model gravitons of the first excited state.

In reference [32] the 95% Condidence Level (C.L) upper limits on the graviton production cross-sections in the dilepton channel were computed by using a binned likelihood method with a likelihood function. The likelihoods were integrated to give the final limits [33]. In the diphoton channel the limits were obtained by using a Bayesian style program. The Bayesian style program utilised the observed number of events in a 3σ mass window around each hypothetical graviton mass, the backgroud prediction in this window, the efficiency and luminosity to compute the limits [45]. This is also called the mass window method. The graviton masses were generated with PYTHIA using CTEQ5L as PDF.

For the dielectron channel, the upper 95% limits on the production cross-sections are shown in figure 3.3 as a function of graviton mass. The cross-sections predicted by the Randall-Sundrum model are also shown. The limits on the Randall-Sundrum model graviton masses are given by the points where the corresponding predicted cross-sections meet the 95% C.L upper limits on the graviton production cross-section. For $\frac{k}{M_{pl}}$=0.1 the gravions are excluded up to 620, 605 and 675 GeV for the dielectron, dimuon and diphoton channels respectively [35]. The excluded region at 95% C.L. is shown in fig 3.4 as function of mass and parameter $\frac{k}{M_{pl}}$. The majority of the excluded masses, are mostly given by high values of $\frac{k}{M_{pl}}$.

Further improvement were achieved by using the mass window method for the dilepton channels, and combining the channels for the DØ analysis. Electrons and photons were not distinguished from each other. This combined the the two channels. A Bayesian limit-setting procedure were used [45]. The signals were generated with PYTHIA using CTEQ5L as PDF.

The data analysed by the DØ detector are shown in figure 3.5. The 95% C.L upper limits on the graviton production cross-section is compared to cross-sections predicted by the Randall-Sundrum model for various mass values in figure 3.6. The 95% CL excluded domain for the dielectron and diphoton decay modes are shown in figure 3.7.

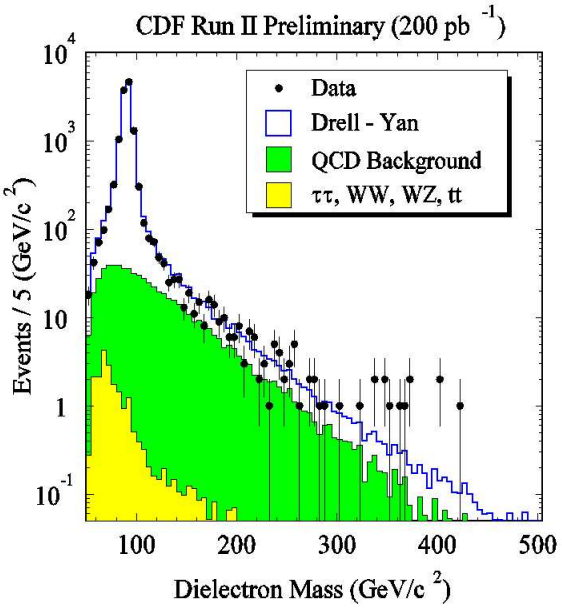

Figure 3.2: Data from Tevatron Run II at an integrated luminosity of 200 pb^{-1}. The data is in agreement with the Drell-Yan prediction from PYTHIA. Plot taken from reference [33].

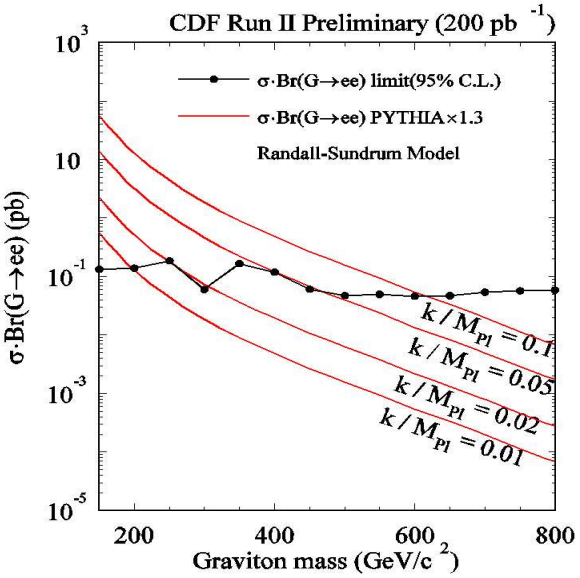

Figure 3.3: The 95% C.L. upper bounds on the graviton production cross-section compared to the cross-sections predicted by the Randall-Sundrum model for different values of $\frac{k}{M_{pl}}$. Plot taken form reference [33].

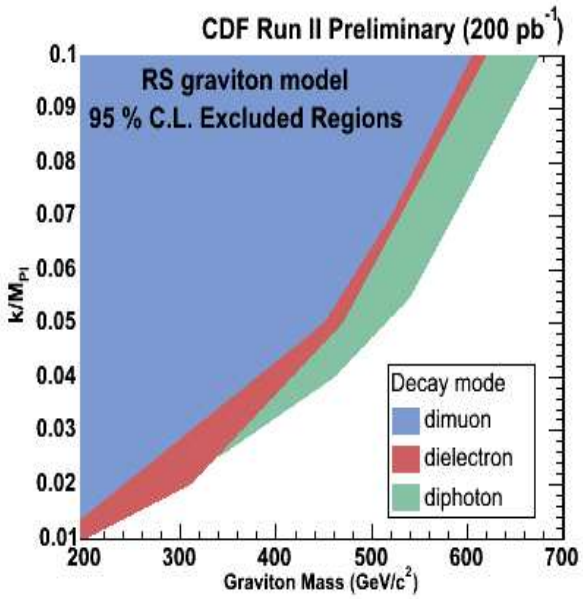

Figure 3.4: 95% C.L. excluded regions for the gravitons as a function of $\frac{k}{M_{pl}}$ for the dimuon, dielectron and diphoton decay modes. Plot taken from reference [33].

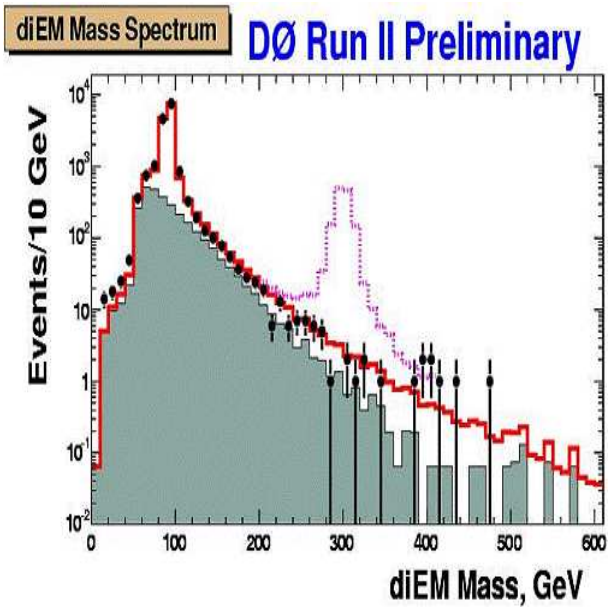

Figure 3.5: Mass distribution in the combined dielectron and diphoton channel. Data are given by the points. Shaded region is the QCD background. The open histogram is the sum of the Drell-Yan and QCD background. The peak in the middle is for a hypothetical graviton of 300 GeV. Plot taken from reference [45].

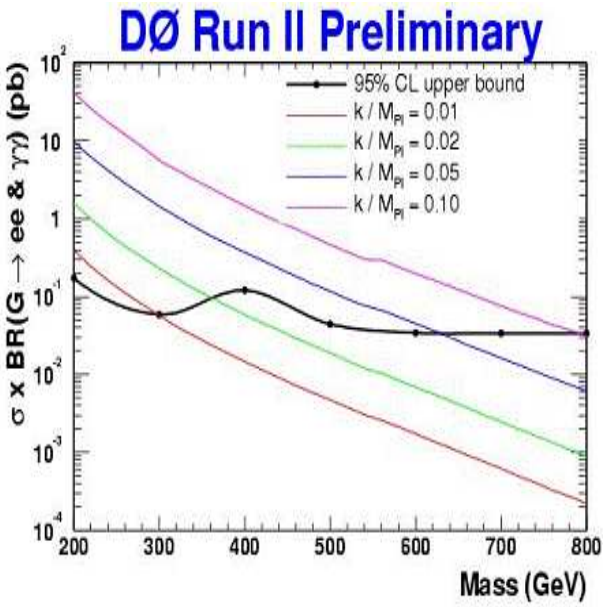

Figure 3.6: The 95% C.L upper bounds on the graviton production cross-section compared to the cross-sections predicted by the Randall-Sundrum model for $\frac{k}{M_{pl}} = 0.01$ (the lower line), 0.02, 0.05 and 0.1(the upper line). Plot taken form reference [45].

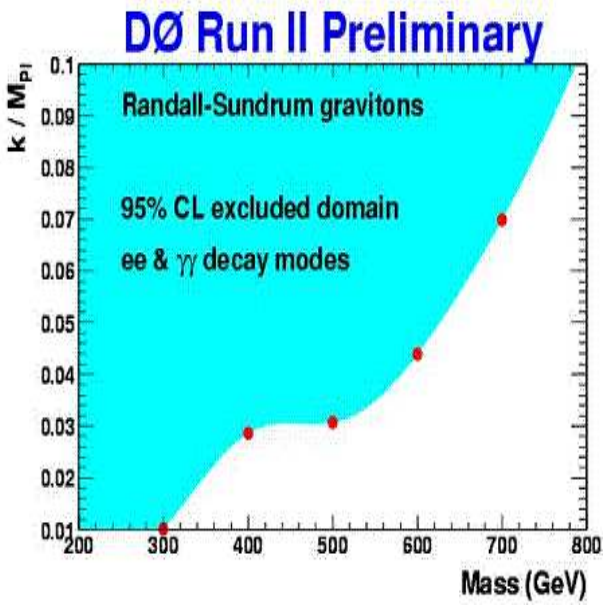

Figure 3.7: 95% C.L. excluded region for the gravitons as a function of $\frac{k}{M_{pl}}$ for the combined dielectron and diphoton decay modes. The dots show the mass points for which the cross-section limits have been obtained for. Plot taken from reference [45].

Gravitons up to 300 GeV are excluded for $\frac{k}{\bar{M}_{pl}}$=0.01, and up to 785 GeV for $\frac{k}{\bar{M}_{pl}}$=0.1.

3.3 Efficiency

Before starting the analysis the concept of efficiency has to be properly defined. Efficiency is an important property which is used throughout the analysis. It is a crucial factor in determing the experimental production cross-section. The total efficiency is calculated by dividing the number of reconstructed events by the number of generated events inside a mass window around the graviton. It tells us how well the detector measures the particles. The total efficiency is a product of (at least) four kinds of efficiencies: the geometrical acceptance of the detector, the reconstruction of the events, the identification of the particles and the trigger conditions:

• The geometrical acceptance is defined by the fraction of events where both of the decay particles are inside the detector. This efficiency is a function of the detector geometry, and is often given by the pseudorapidity, η . The cuts on the pseudorapidity given by -2.5<η<2.5 are implemented in ATLFAST, and cover the area inside the detector. The corresponding cut on the transverse momentum is $P_t > 5$ GeV for electrons and photons, and $P_t > 6$ GeV for muons. Very few events fully occur outside the detector.

• The reconstruction efficiency is the fraction of the tracks, which are correctly reconstructed. This includes, among other, losses from insufficient electron/jet or photon/jet seperation and spoiling of the calorimeter signature, particles with low P_t, those who disappear through cracks and pile up.

• The identification efficiency is a measure of how well the detector identifies the decay particles. Electron identification is done by matching hits in the EM calorimeter with tracks in the Inner Detector, as well as Transistion Radiation measurements. The muon identification is done by matching tracks in the ID with hits in the Muon Spectrometer. Photons are only identified in the EM calorimeter. The identification efficiency is set by hand in the event analysis because ATLFAST does not take this efficiency into account. A detailed study would require a full simulation of ATLAS, which is out of the scope of this study.

• The trigger cuts are made in order to reduce the background events compared to the signal. These are P_t>20 GeV for two electrons or photons, and P_t>10 GeV for two muons at high luminosity.

In ATLFAST the geometrical acceptance and reconstruction efficiency are parameterized into one efficiency. For breviety this efficiency is called the 'acceptance'. The overall efficiency is also dependent on luminosity. The LHC is expected to reach high luminosity after three years of running. High luminosity implies that more events are produced, leading to pile up. Pile up refers to a situation where the detector is affected by several

events at the same time. This causes difficulties in reconstructing the tracks, leading to a loss of efficiency. Since a lot more events are produced at high luminosity, processing interesting data requires harder trigger cuts. The trigger system essentially decides if an event is worth storing. For low luminosity the cuts are P_t>15 GeV for a pair of electrons or photons, and P_t>6 GeV for a pair of muons.

3.4 Signal Reconstruction

The invariant mass of the graviton is reconstructed with electron, muon and photon pairs with the highest transverse momuntum:

$$m_G = \sqrt{(\sum_{j=1}^{2} E_j)^2 - (\sum_{j=1}^{2} \mathbf{P_j})^2} \tag{3.2}$$

Opposite charge is also required. Both leptons have a pseudorapidity $|\eta|$<2.5 i.e. they are inside the acceptence of the ATLAS tracking detector. Monte Carlo is used to obtain the cross-section for each of the input masses, and thus the number of events corresponding to a given luminosity. A lepton and photon identification efficiency of 0.9 and 0.8 for each lepton and photon respectively is applied by hand in the event analysis, and thus the signal and the background events are reduced by 19% and 36% respectively. We only look at the first excited Kaluza Klein state of gravitons. For breviety the mass of the resonances is denoted by m and not m_1.

3.5 Earlier work and results

The study of the $G^* \rightarrow e^+e^-$ decay mode was performed in references [2], [1], and [5].

Herwig 6.3 [34] was used as an event generator and ATLFAST 2.16 was used for the detector simulation. The studies were based on a test model, the Randall-Sundrum scenario. Resonances of the first excitation in the mass range 500 GeV to 2200 GeV were produced for 100 fb^{-1} of integrated luminosity corresponding to one year of high luminosity running at LHC. The coupling $\frac{k}{\overline{M}_{pl}}$ was set to 0.01. OWEN set 1.1 [26] and newer versions of MRST [27] were used as Parton Distribution Functions (PDFs). Discovery limits of the resonances were established and the angular distribution studied. The conclusion was that the graviton resonances were detectable up to 2080 GeV. It was also demonstrated that a graviton resonance is a spin-2 particle by looking at the angular distributions of e^- in the center of mass system of the decaying graviton.

These studies, however have some weaknesses. The HERWIG event generator does not include Final-State QED Radiation (FSR). This gives too high efficiency, as this study shows. Electrons were selected inside the acceptance, and trigger conditions were not used. This corresponds to the minimum isolation of electron-momenta in ATLFAST or the level one trigger ($P_t > 5$ GeV). The discovery reach for the muon channel was given

to be $M_{G^*} < 1700$ GeV in reference [1]. No other information was given. Like in the case with the electron decay mode, HERWIG 6.3 and ATLFAST 2.16 were used. Due to the difficult background no attempt was made to get the mass limit of the graviton resonance through the $G^* \rightarrow \gamma\gamma$ decay mode.

This thesis is meant to improve these previous studies. After reproducing the previous results by starting with similar cuts and conditions, new limits are found by switching on FSR and studying ATLAS trigger conditions. This thesis also estimates the discovery mass limit of the $\gamma\gamma$ channel for the first time.

3.6 $G^* \rightarrow e^+e^-$

This channel has a good signal and a small Drell-Yan background which lies beneath it. The corresponding branching ratio is 2%.

As was mentioned in chapter 1, the Randall-Sundrum model only has two free parameters, the mass and the coupling $\frac{k}{\bar{M}_{pl}}$. In this thesis the mass is used as a free parameter while the coupling is fixed to some value. Before establishing this value, $\frac{k}{\bar{M}_{pl}}$ is studied in detail. In order to reproduce the results in [1],[2] and [5], final state QED radiation is first switched off. The same Parton Distribution Functions are used i.e. OWEN Set 1.1 [26] and newer versions of MRST [27]. This study uses MRST(h-g)(1998) although [1] and [2] used the average of the MRST(c-g) and MRST(h-g). The difference between MRST(h-g) and the latter, average of MRST(h-g) and MRST(c-g), is negligible. In addition a third more recent PDF, CTEQ5L [28], is added to the study. As in [2] the integrated luminosity is set to 100 fb^{-1} and both electrons are selected inside the acceptance, ($P_t > 5$ GeV) i.e. no trigger cuts are applied. The mass discovery limits are established for the different PDFs and compared to the limit from the earlier studies.

In the end the effects of radiation are thoroughly studied as well as their impact on the signal description and efficiency. More realistic mass discovery limits are acquired for the different PDFs by switching on Final State Radiation.

3.6.1 Signal Description

The small background and the excellent resolution makes the $G^* \rightarrow e^+e^-$ channel most promising in terms of discovery. The energy resolution of the electrons, that is the detector's ability to distinguish two closely lying clusters, is given by [1]:

$$\frac{\Delta E}{E} = \frac{12\%}{\sqrt{E}} \oplus \frac{24.5\%}{E_T} \oplus 0.7\% \tag{3.3}$$

ΔE and E are given in GeV. It is clear that the relative uncertainty gets better with increasing energy, and the electrons are easily measured. In order to calculate and study the discovery potential it is necessary to know what kind of function describes the decay products of the graviton in the best possible way. The necessary parameters needed in

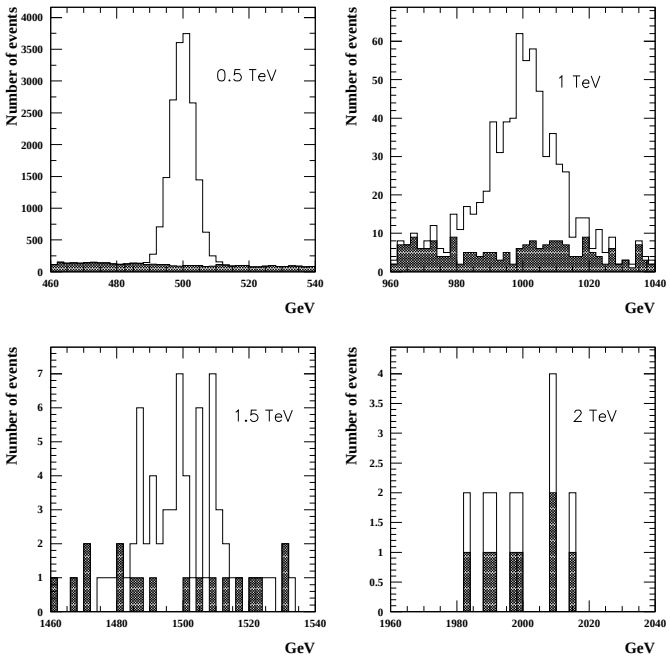

Figure 3.8: Graviton resonances at different masses in the electron decay mode. The Drell-Yan background is shown in black. No trigger cuts are applied.

the study are then extracted. These are the mass experimental resolution, σ_m, and the number of signal events, N_S. As a matter of consistency in regard to [1], [2] and [5], the resonances are described with a gaussian defined as:

$$f(x, \mu, \sigma_m^2) = \frac{1}{\sqrt{2\pi\sigma_m^2}} e^{-\frac{(x-\mu)^2}{2\sigma_m^2}} \tag{3.4}$$

where μ and σ_m are the mean value of the graviton mass and the experimental mass resolution, respectively. The number of signal events N_S, σ_m and μ are found by fitting the signal to a gaussian. At larger graviton masses the cross-section drops. In addition, only about 2% of the gravitons decay into leptons. Consequently the number of signal events drop. That becomes a problem when trying to fit the signal to a gaussian, making it impossible to find the important parameters, due to statistical fluctuations. This is clearly shown in figure 3.8, especially at 2 TeV but also at 1.5 TeV, as compared to 500 GeV and 1 TeV.

This problem is solved by generating large signal and background samples. The luminosity is artificially increased by a factor of 100 to obtain large enough statistics. This makes it possible to extract the experimental resolution, the number of signal events. Signal and background are then scaled down to the integrated luminosity of 100 fb^{-1} in order to get the correct values. These are the *expected* values without fluctuations. In real experiments the signal and background events for high masses fluctuate around these. Before generation of the masses needed the coupling $\frac{k}{\bar{M}_{pl}}$ is constrained.

3.6.2 Determination of $\frac{k}{\bar{M}_{pl}}$

The value of the important coupling $\frac{k}{\bar{M}_{pl}}$, described in chapter 1.2.2, is central to the Randall-Sundrum model. The coupling is the ratio between the five dimensional curvature parameter and the reduced four dimensional planck mass. In PYTHIA the value of $\frac{k}{\bar{M}_{pl}}$ is not set directly. However, the value of the dimensionsless coupling which enters quadratically in all partial widths of the graviton resonance is chosen. The partial width is central in describing the graviton resonance, which like all other resonances, is characterized by its short lifetime. The latter is related to the width, which can be inferred from the decay products of the resonance in some channel. The sum of all partial widths corresponding to various channels, constitutes the total width. The relation between the width, Γ, and the mean lifetime, τ, for a particle at rest is given by [6]: :

$$\Delta W \approx \Gamma \equiv \frac{1}{\tau}. \tag{3.5}$$

As $\frac{k}{\bar{M}_{pl}}$ is proportional to Γ, the resonance becomes more and more shortlived at high $\frac{k}{\bar{M}_{pl}}$.

The allowed region for the coupling is given by equation 1.10 page 6 in the theory chapter:

$$0.01 \leq \frac{k}{\bar{M}_{pl}} \leq 0.1 \tag{3.6}$$

Lower values give us a graviton with small width. This is the so-called narrow graviton resonance. There are good reasons to analyse this narrow resonance. If the real or intrinsic width of the resonance is much smaller than the mass experimental resolution given by a gaussian, the intrinsic width can be ignored. A study of graviton resonances done for the CMS detector [30] gives the observed width to be:

$$\Gamma_{obs} \approx \sqrt{\Gamma_G^2 + 2(\Delta E)^2} \tag{3.7}$$

where Γ_G is the intrinsic width of the resonance, ΔE is the energy resolution in the CMS detector given by [25]:

$$\frac{\Delta E}{E} = \frac{5\%}{\sqrt{E}} \oplus \frac{20\%}{E} \oplus 0.5\% \tag{3.8}$$

The CMS detector has better energy resolution than ATLAS due to its crystal calorimeter. The relation between the observed width, Γ_{obs}, and the experimental mass resolution, σ_m, is Γ_{obs}=$2.36\sigma_m$.

The dimensionsless coupling is set to 0.0054 which correspond to the first Kaluza-Klein excitation given by x_1=3.83 in equation 1.19 and $\frac{k}{\bar{M}_{pl}}$=0.01. Since the production cross-section is proportional to $(\frac{k}{\bar{M}_{pl}})^2$, $\frac{k}{\bar{M}_{pl}}$=0.01 yields a conservative estimation of the cross-section. The experimental mass resolution for different graviton resonance masses and their real widths are given in table 3.2 for different Parton Distribution Functions.

mG (GeV)	Γ_G (GeV)	σ_m^{owen}	$\sigma_m^{mrst(h-g)}$	σ_m^{cteg5l}
500	0.069	3.559	3.494	3.529
1000	0.142	6.060	6.084	6.083
1500	0.213	8.205	8.267	8.373
1600	0.227	8.786	8.499	8.395
1700	0.241	9.073	9.111	8.858
1800	0.256	9.164	9.228	9.298
1900	0.270	9.549	9.932	9.611
2000	0.284	10.11	9.867	9.678
2100	0.298	10.41	9.983	10.67
2200	0.312	11.48	10.82	10.72

Table 3.2: Resonance masses produced with $\frac{k}{M_{pl}}$=0.01, their real widths, Γ_G, and their experimental experimental mass resolutions, σ_m, for different Parton Distribution Functions.

The widths of the resonances are indeed very small compared to the experimental resolution and are thus ignored. At most they are 3% of the experimental resolution. Equation 3.7, taking into account the relation between Γ_G and σ_m, is reduced to:

$$\sigma_m = 0.6 \cdot \Delta E \tag{3.9}$$

When the real width, which is model dependent, is ignored the resulting experimental mass resolution of the resonance is dependent on experimental effects only. Since the graviton couplings are universal, the results of this study hold for any model which predict narrow well-resolved graviton resonances. The graviton modes couple to matter in proportionality to the energy-momentum tensor [5]. This model-independent feature provides the universality of the coupling. There are models based on RS model but with additional branes. Supersymmetric versions also exist, in which the graviton resonances are identical to the ones predicted in the original RS model. As long as the real width is negligible the discovery limit is model independent. Since the graviton is so narrow, for $\frac{k}{M_{pl}}$=0.01, the detector effects determine the observed width in all channels, and interference effects vanish in all observable distributions [5]. The coupling $\frac{k}{M_{pl}}$=0.01 is used throughout this analysis.

Larger values of $\frac{k}{M_{pl}}$ give larger graviton resonance cross-sections while the SM background remains the same. This makes it even easier to detect the resonance and correspondingly the discovery limit increases. Already at $\frac{k}{M_{pl}}$=0.1, which is the most favoured coupling in the allowed region [24], the cross-section increases by two orders of magnitude, but then the graviton resonance is no longer narrow. In the end, large values of $\frac{k}{M_{pl}}$ yield large cross-sections which overwhelm the SM background. The resonance becomes too wide to be identified as a true resonance. At $\frac{k}{M_{pl}}$ $\approx$0.07 the width of the resonance is larger than the experimental mass resolution. This makes a measurement of the width possible but then the results are no longer model independent.

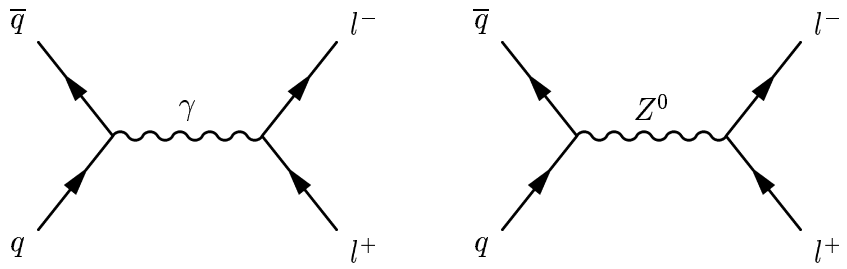

Figure 3.9: The Drell-Yan Process.

3.6.3 Background Description

The resonance signature is not unique because there are SM and non-SM processes that might lead to final states with two leptons or two photons, polluting the signal. Describing this background is important. The Drell-Yan background is given by:

$$q\overline{q} \rightarrow Z/\gamma^* \rightarrow l^+l^- \tag{3.10}$$

where Z or γ^* decay into electron-positron pairs. These processes are given by the PYTHIA parameter ISUB=1 which takes into account the full electroweak interference. The Drell-Yan process consists of a quark and a anti-quark from a pair of interacting protons which annihilate to produce a virtual photon or a Z^0 boson which subsequently converts into a lepton pair[1]. The first part is an an electromagnetic effect, while the latter is due to the weak interaction.

The electromagnetic process appears in region well below the Z^0 mass at 91 GeV, see the upper plot in figure 3.10. The low mass background is generated at an integrated luminosity of 10^{-1} fb^{-1} with the invariant mass laying between $3<M_{e^-e^+}<120$ GeV. The peak to the left of Z^0 decay is due the threshold cut on the invariant mass, $M_{e^-e^+}>3$. The branching ratio for Z^0 decaying into leptons is about 3.4%. Any graviton signal is on top of the Drell-Yan distribution. The lower plot of figure 3.10 shows gravitons with masses of 1 TeV and 1.5 TeV above the background at an integrated luminosity of 100 fb^{-1}.

The cross-section falls with increasing invariant mass, $M_{e^-e^+}$, see table 3.3. In addition this background changes with the choice of PDF.

OWEN set 1.1, an old PDF, gives lower overall cross-section compared to MRST(h-g) and CTEQ5L. At $M_{e^-e^+}>2$ the difference between OWEN set 1.1 and MRST(h-g) is of order 5! The relation between MRST(h-g) and CTEQ5L is more complicated. MRST(h-g) gives higher cross-sections for low cuts. At $M_{e^-e^+}>350$ GeV CTEQ5L gives larger cross-section than MRST(h-g). But this changes with a cut of $M_{e^-e^+}>850$ GeV. Now their cross-sections are equal. For very high invariant masses MRST(h-g) gives again

[1]Properly speaking only the process $q\overline{q} \rightarrow \gamma^* \rightarrow l^+l^-$ is called Drell-Yan. But here the term is used to denote the Z boson contribution as well

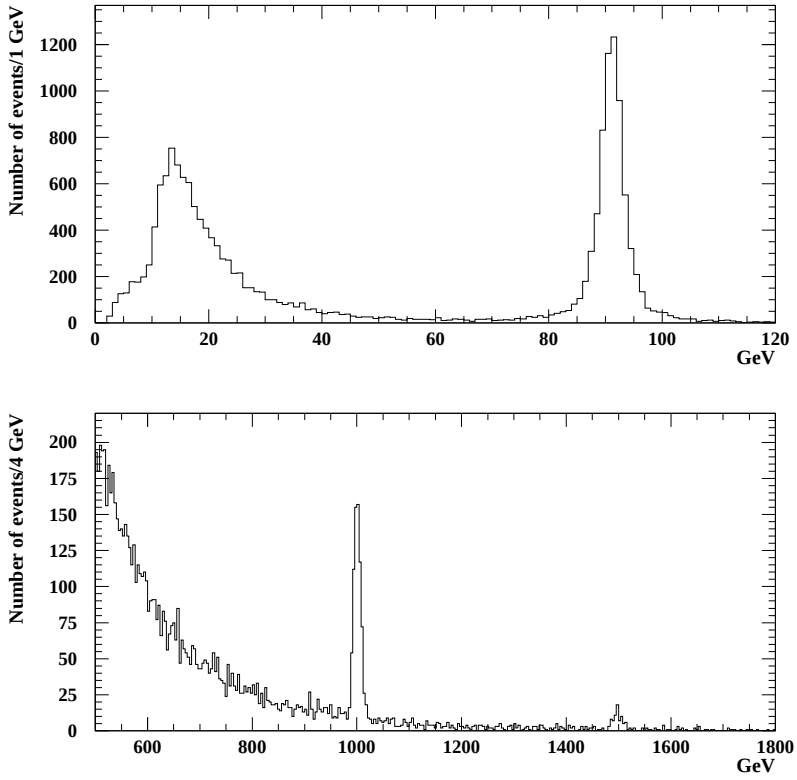

Figure 3.10: Above: Low mass Drell-Yan bacgkground. The Z^0 peak decaying into e^-e^+ to the right at 91 GeV. The peak to the left is due to cut on the invariant mass. Below: gravitons at 1 TeV and 1.5 TeV above the high mass Drell-Yan background. No trigger cuts are applied.

Cut on $M_{e^-e^+}$(GeV)	$(\sigma B)_{OWEN}(mb)$	$(\sigma B)_{MRST(h-g)}(mb)$	$(\sigma B)_{CTEQ5L}(mb)$
$M_{e^-e^+} > 2$	$1.556 \cdot 10^{-5}$	$8.127 \cdot 10^{-5}$	$5.775 \cdot 10^{-5}$
$M_{e^-e^+} > 350$	$3.132 \cdot 10^{-10}$	$3.468 \cdot 10^{-10}$	$3.617 \cdot 10^{-10}$
$M_{e^-e^+} > 850$	$1.239 \cdot 10^{-11}$	$1.310 \cdot 10^{-11}$	$1.308 \cdot 10^{-11}$
$M_{e^-e^+} > 1350$	$1.654 \cdot 10^{-12}$	$1.817 \cdot 10^{-12}$	$1.763 \cdot 10^{-12}$
$M_{e^-e^+} > 1850$	$3.366 \cdot 10^{-13}$	$3.854 \cdot 10^{-13}$	$3.686 \cdot 10^{-13}$

Table 3.3: Drell-Yan cross-sections, σB, for different choices of Parton Distribution Functions and cuts on the invariant mass $M_{e^-e^+}$

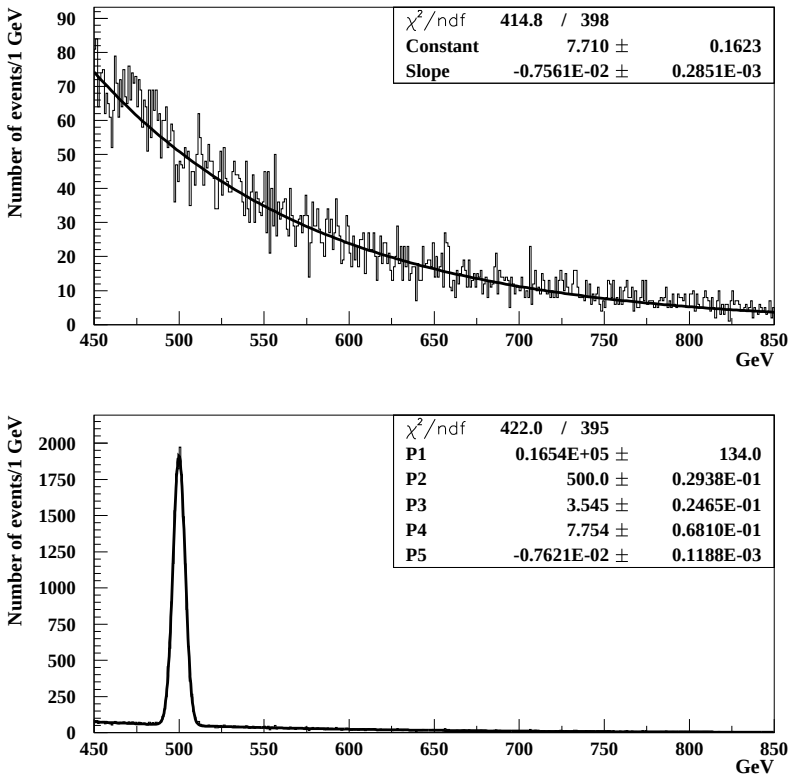

Figure 3.11: Above: Drell-Yan background fitted with an exponential. Below: A graviton resonance at 500 GeV, fitted with a gaussian. Parameter P_1 yields the number of signal events beneath the gaussian. P_2 and P_3 are the mean mass value and the experimental mass resolution, respectively.

higher cross-sections than CTEQ5L. This is not suprising at all since the PDF is a parametrization of the energy and momentum distributions of the partons in a hadron. These distributions are different because of different estimations.

Because of the falling cross-section the exponential is a suitable function to fit the background and it has only two parameters. In figure 3.11 the exponential fits the background rather well, and is used throughout this analysis. The lower plot of figure 3.11 shows the background together with a 500 GeV graviton signal simultaneously fitted with a exponential and a gaussian. The extracted parameters shown are the number of signal events, N_S(P1) , mean value of the graviton mass μ(P2) and the experimental mass resolution σ_m(P3). The Drell-Yan background estimated by PYTHIA is consistent with Tevatron data [33].

mG (GeV)	$(\sigma B)_{owen}$ (fb)	$(\sigma B)_{mrst(h-g)}$ (fb)	$(\sigma B)_{cteg5l}$ (fb)
500	279.6	211.4	185.8
1000	10.8	8.63	6.60
1500	1.20	1.07	0.76
1600	0.82	0.76	0.53
1700	0.57	0.54	0.37
1800	0.40	0.39	0.27
1900	0.29	0.29	0.19
2000	0.21	0.21	0.14
2100	0.15	0.16	0.11
2200	0.11	0.12	0.08

Table 3.4: Cross-sections times branching ratios in the R-S model for different graviton masses and Parton Distribution Functions.

3.6.4 Results

As a matter of consistency graviton masses between 500 GeV and 2200 GeV are generated and no trigger cuts are used as done by [2]. The 500 GeV graviton (with corresponding background) is produced for 100 fb^{-1} of integrated luminosity, which corresponds to one year of high luminosity running at LHC. The rest of the mass points (with corresponding backgrounds) are produced with an artificial integrated luminosity of 10000 fb^{-1}. A lepton identification efficiency of 0.9 for each lepton is added by hand.

The cut on the invariant mass of the background is set to 350 GeV in the event generator. The maximum value of this invariant mass is set to 14000 GeV, the highest value allowed due to the fact that the center of mass energy at LHC is given by E=$\sqrt{s}$=14 TeV. The cross-section for different masses and PDFs obtained by Monte Carlo, are given in table 3.4.

A striking feature in table 3.4 is that the newer PDFs lead to smaller signal cross-sections. All cross-sections from CTEQ5L are smaller than the ones derived from OWEN (1991) and MRST(h-g) (1998). The cross-sections from MRST(h-g) are smaller than the ones from OWEN except for the masses between 1900 GeV to 2200 GeV. The biggest differences are at low graviton masses. At masses of 500 GeV the difference in cross-section between OWEN set 1.1 and MRST(h-g) is 24%. The difference between OWEN set 1.1 and CTEQ5L is 34%. At high masses these differences fade out.

The mass window is an interval which lies symmetrically around the fitted signal. It is given by:

$$\mu \pm 3\sigma_m \tag{3.11}$$

where μ is the mean value of the graviton mass and σ_m is the experimental mass resolution. Inside this window the number of signal and background events are obtained by fitting and integration, respectively.

As in [1] and [2] the minimum number of signal events, N_S^{min}, needed to detect the resonance above the background is taken to be $5\sqrt{N_B}$ or 10, depending on which is greater.

This is due to the requirement:

$$S = \frac{N_S}{\sqrt{N_B}} > 5 \tag{3.12}$$

which is needed to claim discovery. Here S is the significance. The significance tells whether there is a signal present or not at some probabillity. There is a chance that what appears to be a signal is only a fluctuation in the background. With the condition 3.12 we require that the signal is five times larger than the estimated error in the background i.e. the discovery limit is set to 5σ sensitivity. At 5σ sensitivity the probability to find a fluctuation of the background instead of a signal is $\frac{1}{10^6}$. This condition is very strict indeed.

The minimum production cross-section required to produce N_S^{min}, $(\sigma B)^{min}$, is calculated by correcting N_S^{min} for the total efficiency and the luminosity since the number of reconstructed events are given by:

$$N_S^{min} = (\sigma B)^{min} L \epsilon_{tot} \tag{3.13}$$

where σ is the cross-section, L is the integrated luminosity, B is the branching ratio and ϵ_{tot} is the total efficiency without trigger cuts.

In order to get a discovery limit this minimum production cross-section for a given mass point is compared to the corresponding cross-section predicted by the Randall-Sundrum model. The minimum production cross-sections, for different PDFs, are given in the tables 3.5-3.7. Table 3.5 is comparable to table 3 in reference [2].

In tables 3.5-3.7 the total efficiency of the detector varies from 75% to 60%. Without the lepton identification efficiency, which imply a factor of 0.81, these total efficiences vary between 93 % and 74% for the different masses, which is in agreement with [2]. This is true for all the PDFs. We see that the efficiency drops at higher masses. The reason for this is discussed in section 3.7.6. The graviton mass limits for the different PDFs are extracted in the plots 3.12-3.14. The plots compare the cross-sections predicted by the Randall-Sundrum model with the calculated minimum production cross-sections. The mass discovery limit is given at the mass point where the minimum production cross-section meets the corresponding cross-section predicted by theory.

Figures 3.12 and 3.13 show that the maximum graviton mass that can be obtained at LHC is around 2.1 TeV. This is almost exactly what is obtained in references [1] and [2] where the expected discovery mass limit is found to be 2080 GeV. In other words PYTHIA and HERWIG are compatible event generators when Final State QED Radiation is turned off in PYTHIA. A small difference is shown in figure 3.14. Here CTEQ5L is used as PDF and the discovery mass limit shows a slightly lower value. The mass limit is around 2 TeV or a 100 GeV less than the limits obtained by using OWEN set 1.1 and MRST(h-g). This indicates that the PDFs have an impact on the result. Only MRST(h-g) and CTEQ5L are further used in the analysis.

μ (GeV)	$MW_{owen}(GeV)$	N_S	N_B	N_S^{min}	ϵ_{owen}	$(\sigma B)^{min}(fb)$
500	$\pm$10.68	20517.3	839.3	144.9	0.7338	1.975
1000	$\pm$18.18	802.5	65.7	40.5	0.7458	0.543
1501	$\pm$24.62	84.0	10.9	16.5	0.7006	0.236
1601	$\pm$26.36	56.7	8.0	14.1	0.6932	0.203
1701	$\pm$27.23	39.1	5.9	12.2	0.6889	0.177
1802	$\pm$27.49	26.6	4.3	10.4	0.6633	0.157
1902	$\pm$28.65	18.8	3.2	10.0	0.6564	0.152
2002	$\pm$30.33	13.3	2.4	10.0	0.6463	0.155
2102	$\pm$31.23	9.5	1.7	10.0	0.6367	0.157
2203	$\pm$34.44	6.7	1.4	10.0	0.6124	0.163

Table 3.5: The mass windows (MW) for different masses, given by $\mu \pm 3\ \sigma_m$ where the background and signal events are obtained by integration and fitting, respectively. The number of signal events beneath a gaussian, N_S. The number of background events inside the mass window, N_B. The minimal signal events needed to detect the resonance, N_S^{min}. The total efficiency inside a mass window, ϵ_{owen}, and the minimum cross-section needed to detect the graviton, $(\sigma B)^{min}$. OWEN set 1.1 PDF used.

μ (GeV)	$MW_{mrst(h-g)}(GeV)$	N_S	N_B	N_S^{min}	$\epsilon_{mrst(h-g)}$	$(\sigma B)^{min}(fb)$
500	$\pm$10.48	15057.9	867.0	147.2	0.7123	2.067
1000	$\pm$18.25	635.9	68.8	41.5	0.7365	0.564
1501	$\pm$24.80	74.7	11.5	17.0	0.6975	0.244
1601	$\pm$25.50	52.3	8.3	14.4	0.6907	0.209
1701	$\pm$27.33	37.1	6.2	12.5	0.6855	0.182
1802	$\pm$27.68	25.9	4.6	10.7	0.6656	0.161
1902	$\pm$27.80	18.8	3.6	10.0	0.6603	0.151
2002	$\pm$29.60	13.4	2.5	10.0	0.6360	0.157
2103	$\pm$29.95	9.8	1.8	10.0	0.6226	0.161
2202	$\pm$32.46	7.2	1.7	10.0	0.6076	0.165

Table 3.6: The mass windows (MW) for different masses, given by $\mu \pm 3\ \sigma_m$, where the background and signal events are obtained by integration and fitting, respectively. The number of signal events beneath a gaussian, N_S. The number of background events inside the mass window, N_B. The minimal signal events needed to detect the resonance, N_S^{min}. The total efficiency inside a mass window, $\epsilon_{mrst(h-g)}$, and the minimum cross-section needed to detect the graviton, $(\sigma B)^{min}$. MRST(h-g) PDF used.

μ **(GeV)**	$MW_{cteq5l}(GeV)$	N_S	N_B	N_S^{min}	ϵ_{cteq5l}	$(\sigma B)^{min}(fb)$
500	$\pm$10.59	13324.5	930.3	152.5	0.7171	2.127
1000	$\pm$18.25	483.2	68.9	41.5	0.7372	0.563
1501	$\pm$25.12	53.0	11.4	16.9	0.6985	0.242
1601	$\pm$25.19	35.6	8.0	14.1	0.6772	0.208
1701	$\pm$26.57	24.4	5.8	12.0	0.6573	0.183
1802	$\pm$27.89	17.5	4.3	10.4	0.6559	0.159
1902	$\pm$28.83	12.5	3.3	10.0	0.6477	0.154
2002	$\pm$29.03	8.6	2.4	10.0	0.6034	0.167
2102	$\pm$32.01	6.9	1.9	10.0	0.6571	0.152
2204	$\pm$32.16	4.7	1.4	10.0	0.5964	0.168

Table 3.7: The mass windows (MW) for different masses, given by $\mu \pm 3\ \sigma_m$, where the background and signal events are obtained by integration and fitting, respectively. The number of signal events beneath a gaussian, N_S. The number of background events inside the mass window, N_B. The minimal signal events needed to detect the resonance, N_S^{min}. The total efficiency inside a mass window, ϵ_{cteq5l}, and the minimum cross-section needed to detect the graviton, $(\sigma B)^{min}$. CTEQ5L used as PDF.

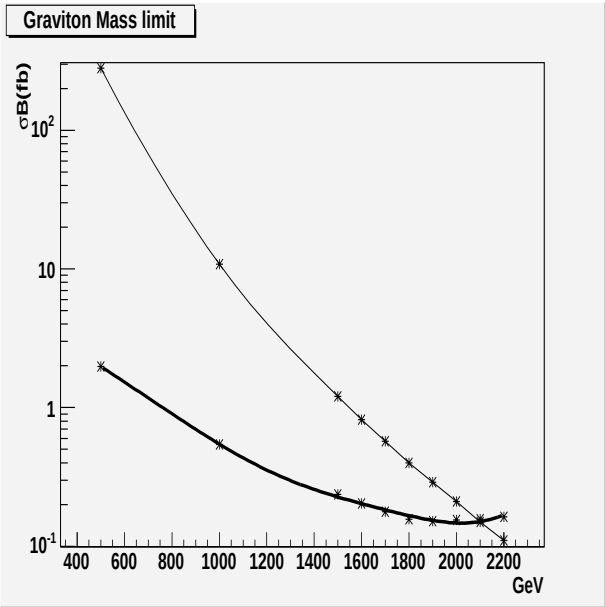

Figure 3.12: Cross-sections for $G \rightarrow e^+e^-$ in the R-S model (light curve) and the smallest detectable cross-setion (black). OWEN set 1.1 used.

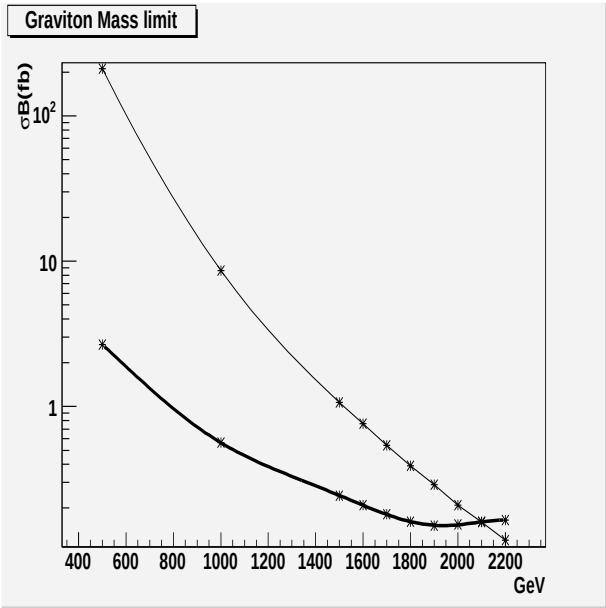

Figure 3.13: Cross-sections for $G \to e^+e^-$ in the R-S model (light curve) and the smallest detectable cross-setion (black). MRST(h-g) used.

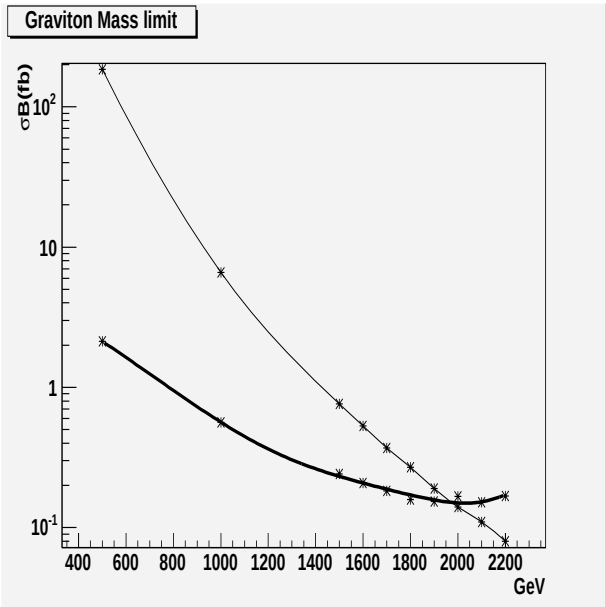

Figure 3.14: Cross-sections for $G \to e^+e^-$ in the R-S model (light curve) and the smallest detectable cross-setion (black). CTEQ5L used.

3.7 $G^* \rightarrow e^+e^-$- The effects of radiation

In this section the effects of Final State QED Radiation and Initial State Radiation are studied in detail. The source of the two types of radiations is as follows:

• Initial State Radiation (ISR) is caused by the radiation of a photon (QED) or a gluon (QCD) from one of the partons entering the hard process before the collision happens.

• Final State Radiation (FSR) is caused by the radiation of a photon (QED) or a gluon (QCD) from one of the decay products in the hard process after the collision has happened.

As this thesis only look at leptons and photons in final state there is no final state QCD radiation involved.

In section 3.7.1-3.7.4 we look at a graviton resonance of 500 GeV, produced at an integrated luminosity of 100 fb^{-1}. Two PDFs, MRST(h-g) and CTEQ5L, are used. No trigger cuts nor electron identification efficiency is applied, i.e. we are looking at the acceptance. In order to understand the effects of radiation the following scenarios are analysed:

• Initial State and Final State Radiation switched off i.e. no radiation, section 3.7.1.

• Initial State Radiation switched on, Final State Radiation switched off, section 3.7.2. This is also the case in section 3.6.

• Initial State Radiation switched off, Final State Radiation switched on, section 3.7.3.

• Initial State and Final State Radiation switched on, which is the most realistic case, section 3.7.4

FSR and ISR influence the transverse momentum distribution of the electron and positron coming from the graviton decay. The p_t distributions of figures 3.15-3.20 compare the different scenarios above. p_{t1} is the transverse momentum of the first lepton which is most energetic, and p_{t2} is transverse momentum of the second lepton. The scenarios above also influence the number of leptons and photons created in the final state as well as the distribution of the angles between the two leptons. These are given in figures 3.21-3.26. The correlations between the number of leptons and photons created in the final state are given in figures 3.27-3.34, and the correlation between p_{t1}/ p_{t2} and the angular distributions in figures 3.35-3.50. As expected MRST(h-g) yields more signal events than CTEQ5L in all the figures because of the higher signal cross-section. In each scenario 21140 and 18580 events are generated for MRST(h-g) and CTEQ5L respectively, corresponding to an integrated luminosity of 100 fb^{-1}. Mean values of transverse momenta, number of lepton and photon events in final state are given in tables 3.8-3.11. Section 3.7.5 compares the overall signal and background efficiencies. Their evolution is explained by the ratio $\frac{E}{p}$. The signal and the background are described in section 3.7.6 and 3.7.7, respectively. The signal is described with different functions in order to take into account the effects of radiation. Discovery mass limits are derived for the different scenarios in section 3.7.8.

3.7.1 No Radiation

In the case of no radiation both of the leptons have a maximum transverse momentum of around 250 GeV. The reason is that the graviton created is at rest in the laboratory system i.e. the sum of the transverse momenta of the partons is zero. When the graviton decays the outgoing leptons have equal transverse momentum spectra and are opposite directed. A large number of events are back to back, i.e. the angle between them is π, see figure 3.23. Figures 3.35-3.36 (for MRST(h-g)), and 3.43-3.44 (for CTEQ5L) show that the number of back to back events increases with increasing transverse momentum, peaking at about 250 GeV. The PDFs affect the shape of the angular distributions though. In figures 3.23-3.26 the CTEQ5L distributions flatten out with decreasing angle, while the distributions given by MRST(h-g) give a little top at the end around zero degrees. This is due to the fact that the graviton is created through different production mechanisms. Table 3.40 later in the analysis, shows that more gravitons are produced via $q\overline{q} \rightarrow \mathrm{G}^*$ when CTEQ5L is used.

The acceptance is high. 19030 and 16900 events containing 2 or more leptons are produced for MRST(h-g) and CTEQ5L, respectively, which corresponds to an acceptance of 90% and 91%. Thus the losses are of order 10% which correspond to events with only one or zero leptons in the final state. In addition 179 single and 9 double photons are created with MRST(h-g). For CTEQ5L the number is 209 and 8 respectively. Figures 3.27 and 3.31 show that the majority of the single photons are created in events containing two leptons. Since ISR and FSR are switched off neither the partons nor the leptons radiate and thus these photons come from another source, namely multiple interactions. Several parton pairs can participate in hard interactions at the same time. Thus several hard interactions in one and the same event can occur. This contributes to the overall event activity, in particular at low P_t. Removing the possibility of multiple interactions also removes the photons created in this case. This is done by setting MSTP(81)=0 in PYTHIA. Multiple interactions account for only a small part of the events produced with only a single lepton. The rest can be explained by the detector's failure to reconstruct or measure leptons. This includes leptons with large η, low P_t or electrons within jets.

3.7.2 Only ISR

When one of the incoming partons radiate a photon or a gluon, the sum of the transverse momemtum of the colliding partons does not vanish anymore. Thus the graviton created inside the ATLAS detector is not at rest, and has a momentum in the transversal direction relative to the laboratory system. This extra momentum is shared by the outgoing leptons. The first lepton gets more of this momentum than the second. The transverse momentum spectra are not equal and opposite anymore. The difference with the case of no radiation is clear. In figures 3.15 and 3.16 the maximum transverse momentum of p_{t1} is above 400 GeV. In tables 3.8 and 3.9 we see that the mean value of p_{t1} increases compared to the case with no radiation. For p_{t2} the mean value decreases compared to the case with no radiation. But the sum of these two mean values is larger than in the other cases, giving an overall increase in transverse momentum. Comparing

figure 3.23 and 3.24 we see that the number of back to back events are reduced compared to a situation without radiation because of the transversal direction of the graviton. The non back to back events increase. The correlation between p_{t1}/ p_{t2} and the angular distributions in figures 3.37-3.38 and 3.45-3.46 shows that the back to back events are more evenly distributed with regard to the transverse momentum, peaking at around 250 GeV, as compared to the case without radiation (figures 3.35-3.36 and 3.43-3.44).

The acceptance is a little lower compared to the case without radiation (table 3.8 and 3.9). 18730 and 16650 events containing two leptons are produced for MRST(h-g) and CTEQ5L respectively giving an acceptance of 89 and 90% respectively. ISR has a very small impact on the efficiency. The losses are due to an increase in number of events containing only one or zero leptons. These efficiencies are almost the same as the efficiencies given in the tables 3.6 and 3.7 in section 3.6.4 for a graviton of 500 GeV, if we, like in this section, do not take into account lepton identification efficiency. Since the partons which enter the hard process radiate the number of photons produced also increases. 887 single and 45 diphotons are created with MRST(h-g). For CTEQ5L the number is 777 and 44, respectively. But there is an additional difference compared to the case without radiation. In figure 3.28 and 3.32 the number of single photons produced in events with only one lepton has increased compared to photons produced in events with two leptons. This is due to the fact that the number of events containing one lepton has increased at the expence of events containing two or three leptons.

3.7.3 Only FSR

When switching on FSR (while ISR is off) the graviton is again produced at rest in the laboratory system. Although the transverse momentum spectra are opposite and equal they have changed. The invariant mass of the hard process is preserved but by adding FSR the leptons radiate, adding photons in the final state. FSR subdivides the invariant mass among more particles. One has to add back on $e^-e^+\gamma$ or $e^-e^+\gamma\gamma$, depending on the event, and not e^-e^+, in order to get the original graviton mass. Thus the invariant mass is lowered since we only take into account leptons. The sum of the mean values of p_{t1} and p_{t2} is reduced compared to the case with only ISR. The differences are shown in figures 3.17 and 3.18. In fact, this sum is smaller compared to the other cases. As in the other cases the loss of acceptance is due to the events containing one or zero leptons. In addition to the number of photons, the correlation between the number of photons and leptons produced, have also dramatically changed. In figures 3.29 and 3.33 the number of single photons produced in events with single lepton has increased significantly compared with the cases above. Also, a difference between the PDFs appear. For MRST(h-g) the number of double photons is less than in the case with only ISR, while for CTEQ5L the number of double photons is higher than in the case with only ISR. See figures 3.21 and 3.22.

Radiation	N	$<p_{t1}>$ (GeV)	$<p_{t2}>$ (GeV)
No Radiation	19030	220.3	217.8
Only ISR	18730	248.6	201.0
Only FSR	14610	217.9	212.7
ISR and FSR	14340	246.1	197.4

Table 3.8: The mean values of p_{t1} and p_{t2} and number of events reconstructed, N, for different scenarios described in the text. MRST(h-g) used as PDF. No trigger cuts.

Radiation	N	$<p_{t1}>$ (GeV)	$<p_{t2}>$ (GeV)
No Radiation	16900	218.9	216.3
Only ISR	16650	245.3	200.9
Only FSR	13030	217.0	211.8
ISR and FSR	12750	242.9	196.9

Table 3.9: The mean values of p_{t1} and p_{t2} and number of events reconstructed, N, for different scenarios described in the text. CTEQ5L used as PDF. No trigger cuts.

3.7.4 ISR and FSR

Switching on ISR and FSR give the most realistic situation. In this case the mean value of p_{t1} is high, while the meanvalue of p_{t2} is smaller compared with the scenarios above. The FSR reduces the momentum spectra but the ISR changes the spectra yet again, by increasing the overall transverse momentum. The differences with the case of only FSR are shown in figures 3.19 and 3.20. The number of back to back events are at the lowest, the number of photons and $e^-\gamma$ or $e^+\gamma$ events are at the highest compared with the other cases. ISR and FSR give the lowest acceptance which is 68% and 69% for MRST(h-g) and CTEQ5L respectively. Taking into account lepton identification efficiency of 0.9 for each lepton these efficiencies drop to 55% and 56%, respectively. This is a significant loss compared to the efficiencies for a graviton of 500 GeV in tables 3.6 and 3.7. This has an impact on the mass discovery limits for both MRST(h-g) and CTEQ5L. The losses increase even more because switching on FSR changes the shape of the signal, making it harder to describe with a gaussian.

3.7.5 The ration $\frac{E}{p}$ and the overall efficiency

Radiation hampers the acceptance. In a real experiment electrons and positrons are reconstructed by matching hits in the EM calorimeter with the tracks in the ID. Clusters have to pass cuts on shower shapes in the electromagnetic calorimeter and must satisfy requirements made on the ratio $\frac{E}{p}$ where E is the energy and p is the momentum measured in the EM calorimeter and ID respectively. Particles that pass these cuts are considered as electron or positron candidates. Theoretically the value of this ratio is one but FSR causes the value of $\frac{E}{p}$ to fluctuate, since some electron/positron momentum is not correctly measured. FSR is only measured by the EM calorimeter and not in the

Radiation	$N_{leptons}$=0	$N_{leptons}$=1	$N_{leptons}$=2	$N_{leptons}$=3
No Radiation	40	2074	19020	1
Only ISR	48	2364	18700	27
Only FSR	520	6006	14610	0
ISR and FSR	603	6186	14320	23

Radiation	$N_{photons}$=1	$N_{photons}$=2	$N_{photons}$=3
No Radiation	179	9	0
Only ISR	887	45	3
Only FSR	1449	40	0
ISR and FSR	2051	134	5

Table 3.10: Number of photons and leptons produced in final state for different scenarios. MRST(h-g) used as PDF. No trigger cuts.

Radiation	$N_{leptons}$=0	$N_{leptons}$=1	$N_{leptons}$=2	$N_{leptons}$=3
No Radiation	43	1640	16900	1
Only ISR	49	1879	16640	15
Only FSR	434	5115	13030	0
ISR and FSR	478	5349	12730	21

Radiation	$N_{photons}$=1	$N_{photons}$=2	$N_{photons}$=3
No Radiation	209	8	0
Only ISR	777	44	3
Only FSR	1334	51	0
ISR and FSR	1844	112	4

Table 3.11: Number of photons and leptons produced in final state for different scenarios. CTEQ5L used as PDF. No trigger cuts.

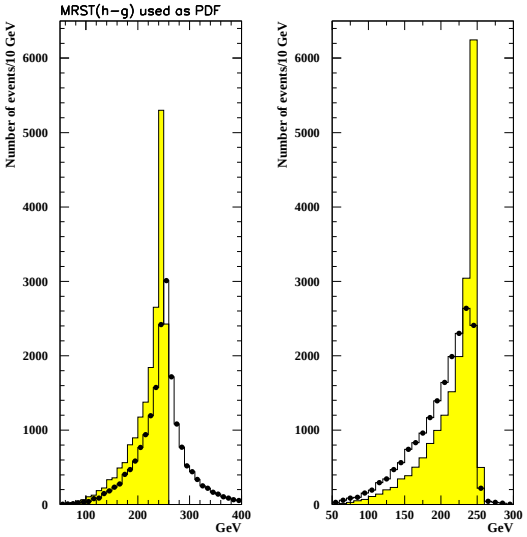

Figure 3.15: Distribution for p_{t1} (left) and p_{t2} (right) of a 500 GeV graviton resonance. ISR and FSR switched off (shaded histogram). ISR switched on, FSR switched off (open histogram with points). MRST(h-g) used as PDF. No trigger cuts.

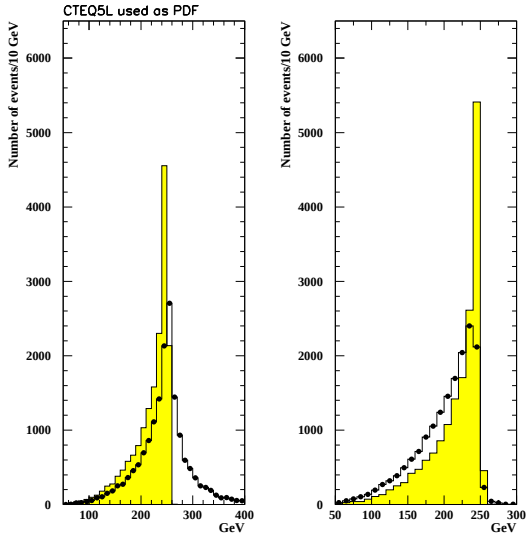

Figure 3.16: Distribution for p_{t1} (left) and p_{t2} (right) of a 500 GeV graviton resonance. ISR and FSR switched off (shaded histogram). ISR switched on, FSR switched off (open histogram with points). CTEQ5L used as PDF. No trigger cuts.

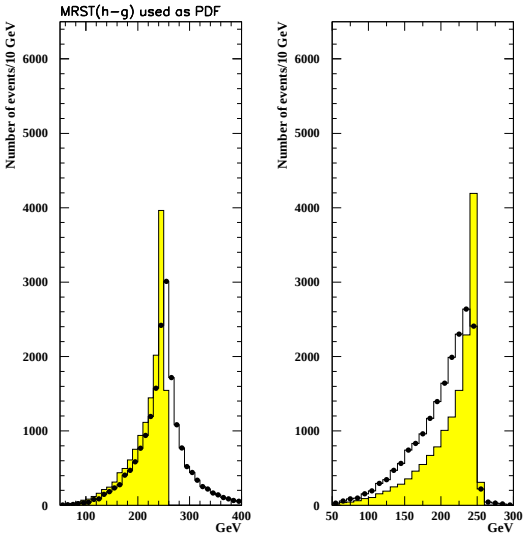

Figure 3.17: Distribution for p_{t1} (left) and p_{t2} (right) of a 500 GeV graviton resonance. ISR switched off, FSR switched on (shaded histogram). ISR switched on, FSR switched off (open histogram with points). MRST(h-g) used as PDF. No trigger cuts.

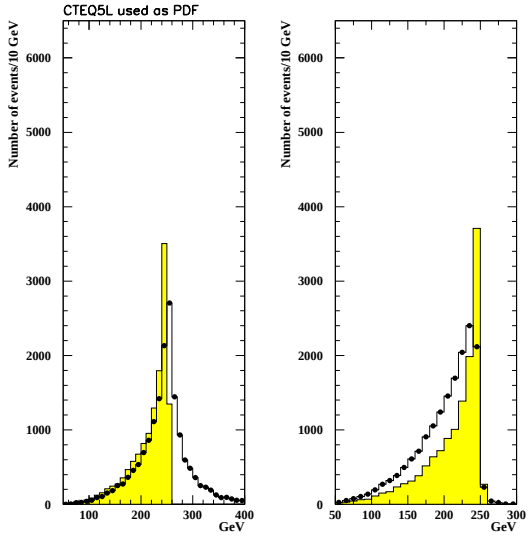

Figure 3.18: Distribution for p_{t1} (left) and p_{t2} (right) of a 500 GeV graviton resonance. ISR switched off, FSR switched on (shaded histogram). ISR switched on, FSR switched off (open histogram with points). CTEQ5L used as PDF. No trigger cuts.

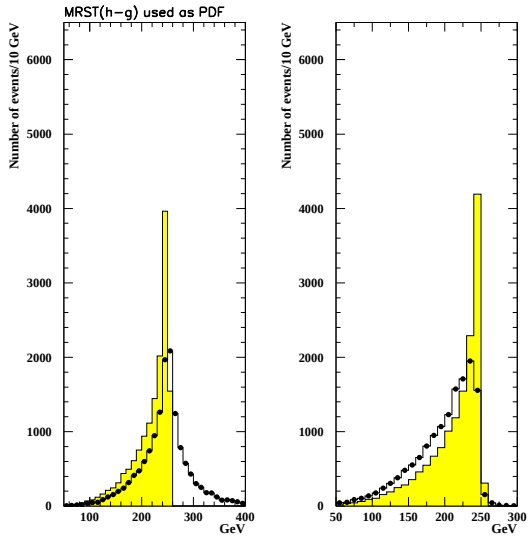

Figure 3.19: Distribution for p_{t1} (left) and p_{t2} (right) of a 500 GeV graviton resonance. ISR switced off, FSR switched on (shaded histogram). ISR and FSR switched on (open histogram with points). MRST(h-g) used as PDF. No trigger cuts.

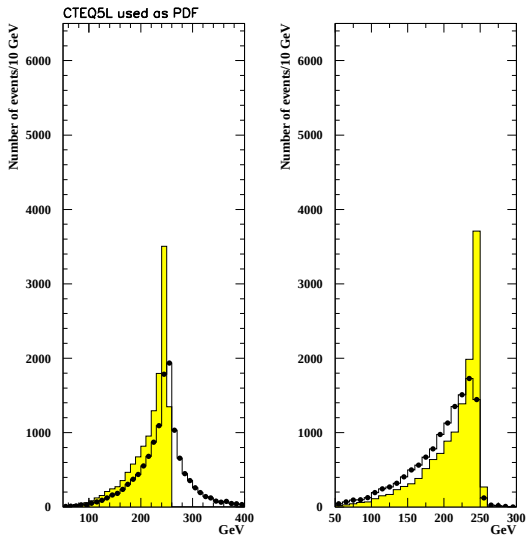

Figure 3.20: Distribution for p_{t1} (left) and p_{t2} (right) of a 500 GeV graviton resonance. ISR switced off, FSR switched on (shaded histogram). ISR and FSR switched on (open histogram with points). CTEQ5L used as PDF. No trigger cuts.

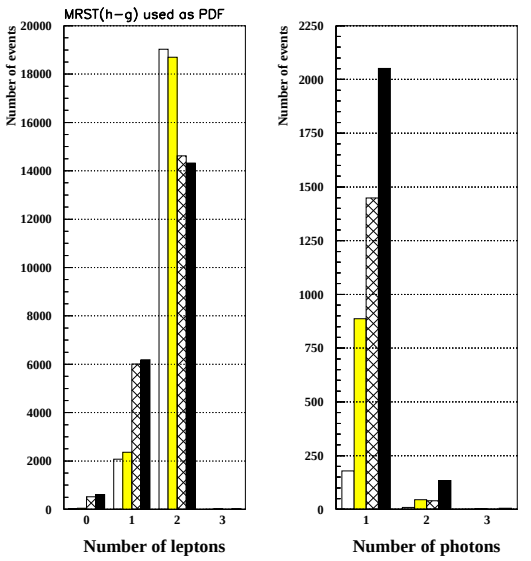

Figure 3.21: Number of leptons and photons in final state for different scenarios. No radiation (white bar), only ISR (shaded bar), only FSR (hatched bar), and ISR & FSR (black bar). MRST(h-g) used as PDF. No trigger cuts.

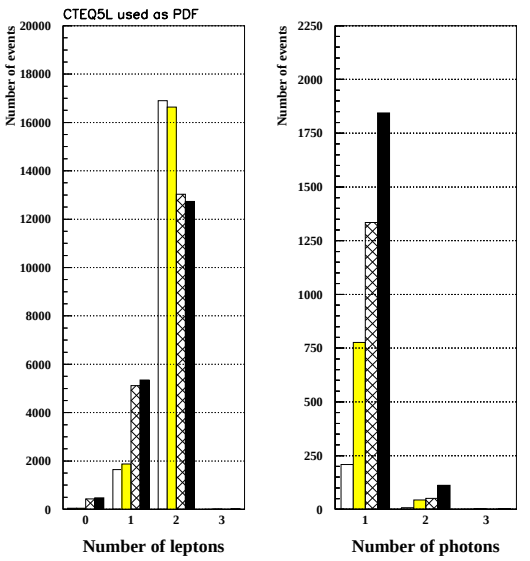

Figure 3.22: Number of leptons and photons in final state for different scenarios. No radiation (white bar), only ISR (shaded bar), only FSR (hatched bar), and ISR & FSR (black bar). CTEQ5L used as PDF. No trigger cuts.

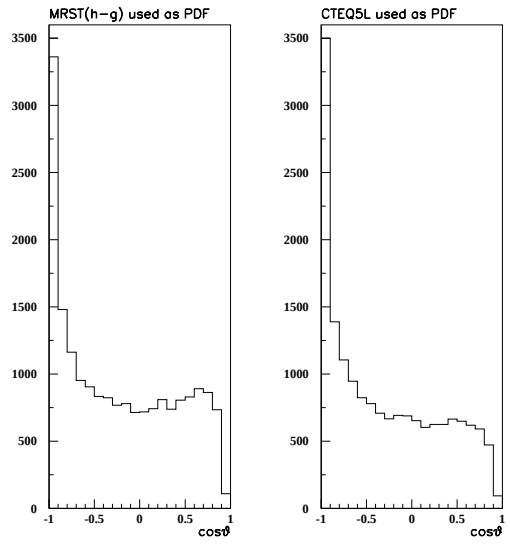

Figure 3.23: Distribution of angles between the decay products of a 500 GeV graviton in the channel $G \to e^+e^-$. ISR and FSR switched off. MRST(h-g) and CTEQ5L used as PDFs. No trigger cuts.

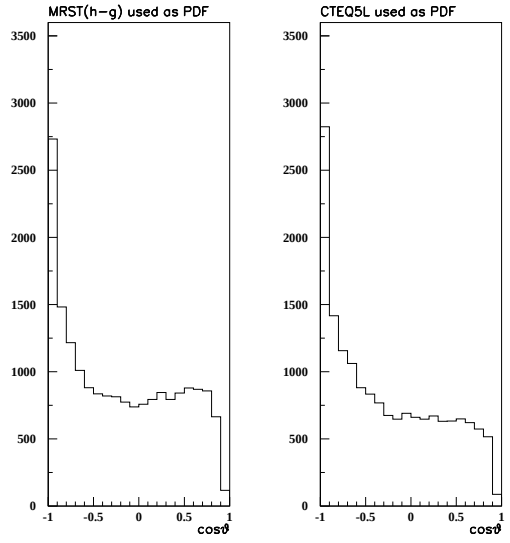

Figure 3.24: Distribution of angles between the decay products of a 500 GeV graviton in the channel $G \to e^+e^-$. ISR switced on, FSR switched off. MRST(h-g) and CTEQ5L used as PDFs. No trigger cuts.

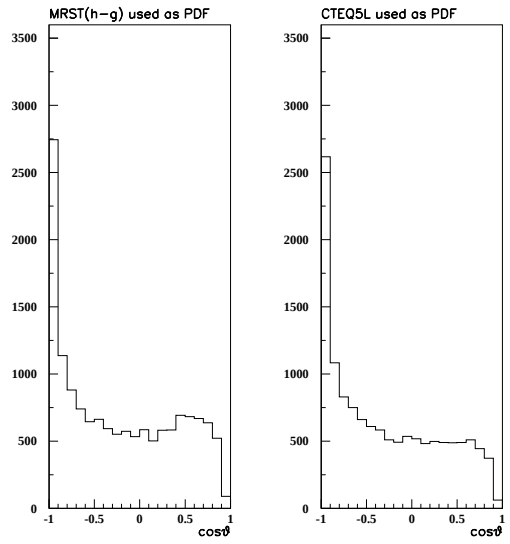

Figure 3.25: Distribution of angles between the decay products of a 500 GeV graviton in the channel $G \to e^+e^-$. ISR switched off, FSR switched on. MRST(h-g) and CTEQ5L used as PDFs. No trigger cuts.

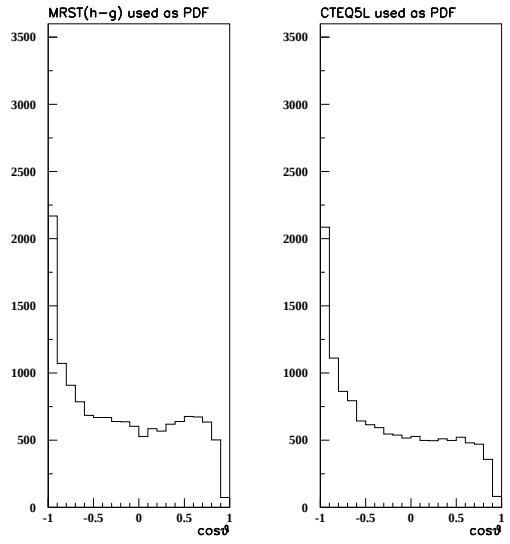

Figure 3.26: Distribution of angles between the decay products of a 500 GeV graviton in the channel $G \to e^+e^-$. ISR and FSR switched on. MRST(h-g) and CTEQ5L used as PDFs. No trigger cuts.

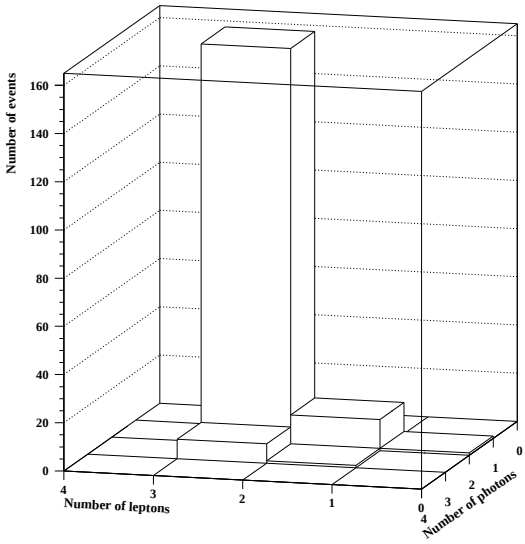

Figure 3.27: Correlation between number of photons and leptons in events produced with no radiation. MRST(h-g) used as PDF. No trigger cuts.

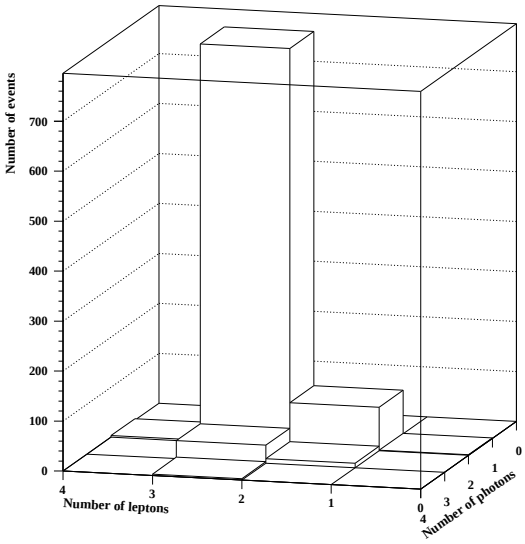

Figure 3.28: Correlation between number of photons and leptons in events produced with only ISR. MRST(h-g) used as PDF. No trigger cuts.

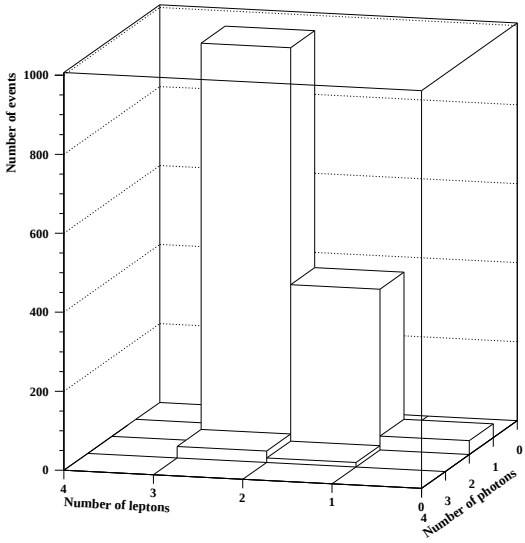

Figure 3.29: Correlation between number of photons and leptons in events produced with only FSR. MRST(h-g) used as PDF. No trigger cuts.

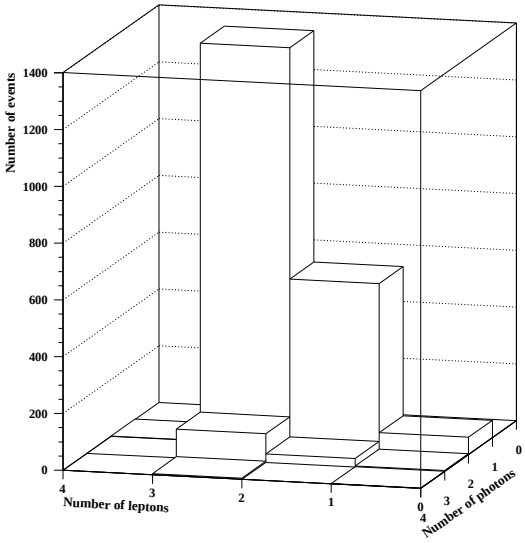

Figure 3.30: Correlation between number of photons and leptons in events produced with ISR and FSR. MRST(h-g) used as PDF. No trigger cuts.

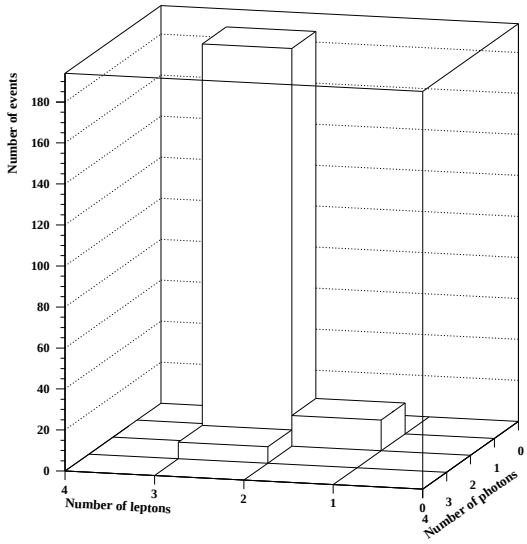

Figure 3.31: Correlation between number of photons and leptons in events produced with no radiation. CTEQ5L used as PDF. No trigger cuts.

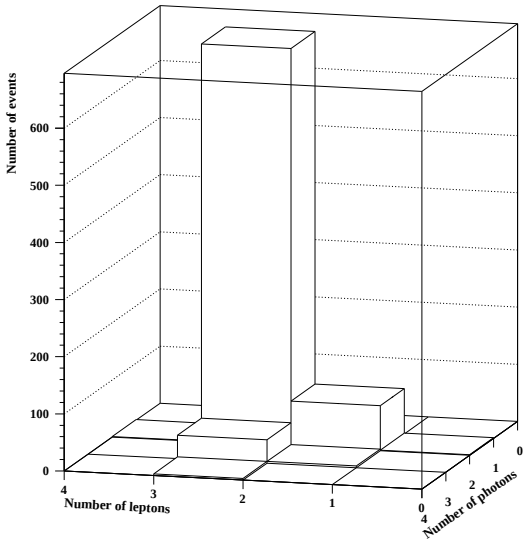

Figure 3.32: Correlation between number of photons and leptons in events produced with only ISR. CTEQ5L used as PDF. No trigger cuts.

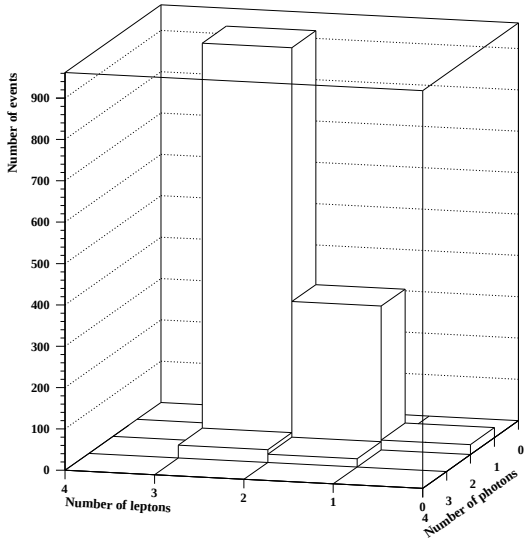

Figure 3.33: Correlation between number of photons and leptons in events produced with only FSR. CTEQ5L used as PDF. No trigger cuts.

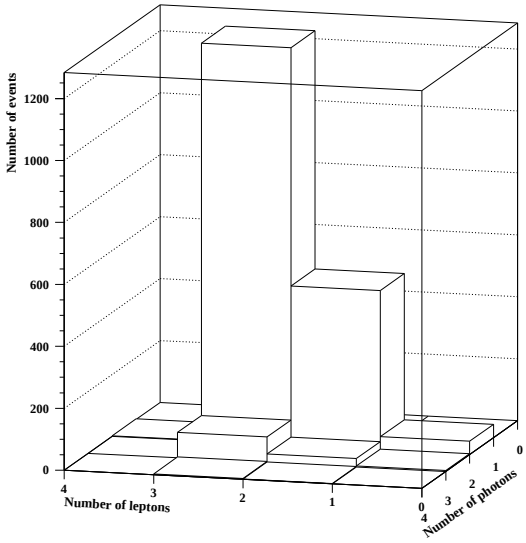

Figure 3.34: Correlation between number of photons and leptons in events produced with ISR and FSR. CTEQ5L used as PDF. No trigger cuts.

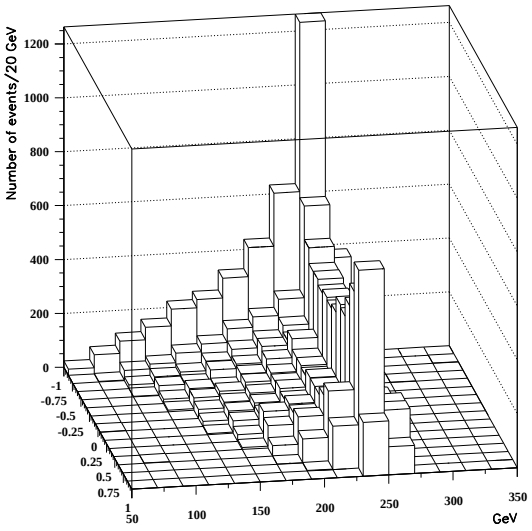

Figure 3.35: Correlation between the angular distribution and p_{t1} in events produced with no radiation. MRST(h-g) used as PDF. No trigger cuts.

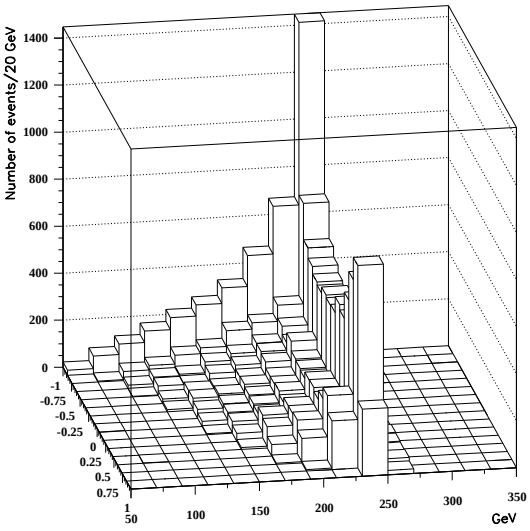

Figure 3.36: Correlation between the angular distribution and p_{t2} in events produced with no radiation. MRST(h-g) used as PDF. No trigger cuts.

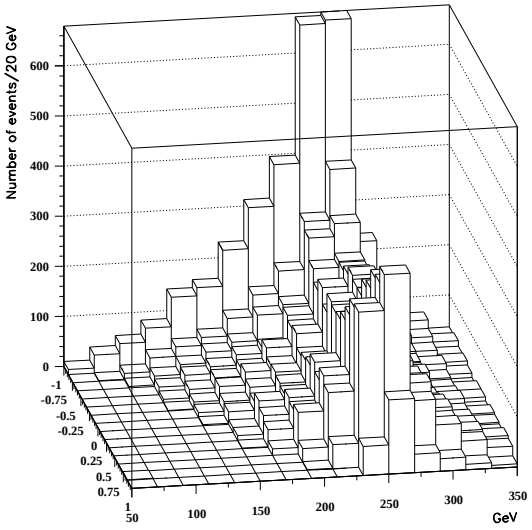

Figure 3.37: Correlation between the angular distribution and p_{t1} in events produced with only ISR. MRST(h-g) used as PDF. No trigger cuts.

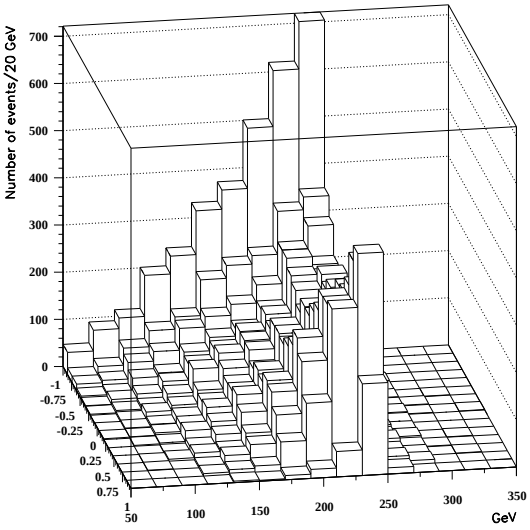

Figure 3.38: Correlation between the angular distribution and p_{t2} in events produced with only ISR. MRST(h-g) used as PDF. No trigger cuts.

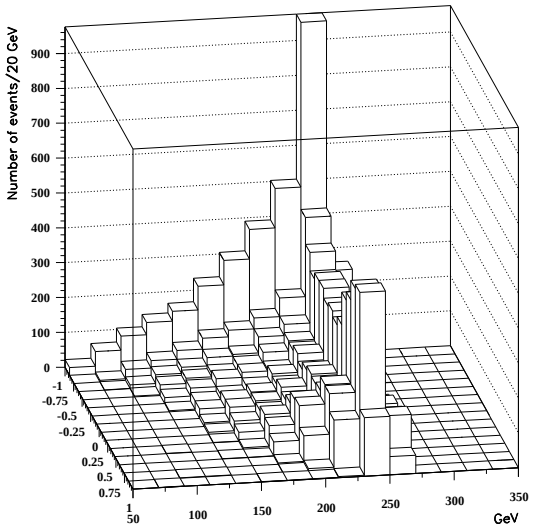

Figure 3.39: Correlation between the angular distribution and p_{t1} in events produced with only FSR. MRST(h-g) used as PDF. No trigger cuts.

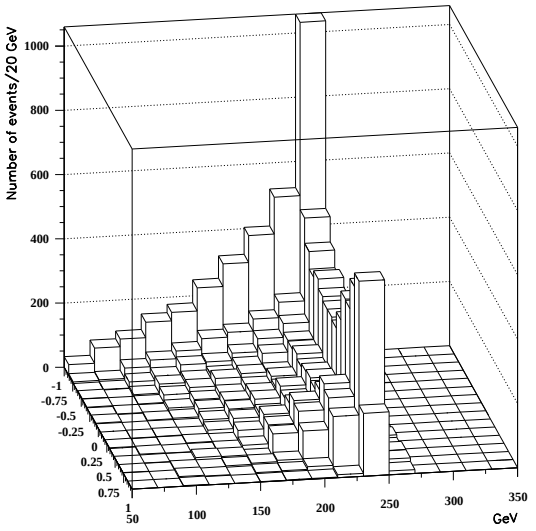

Figure 3.40: Correlation between the angular distribution and p_{t2} in events produced with only FSR. MRST(h-g) used as PDF. No trigger cuts.

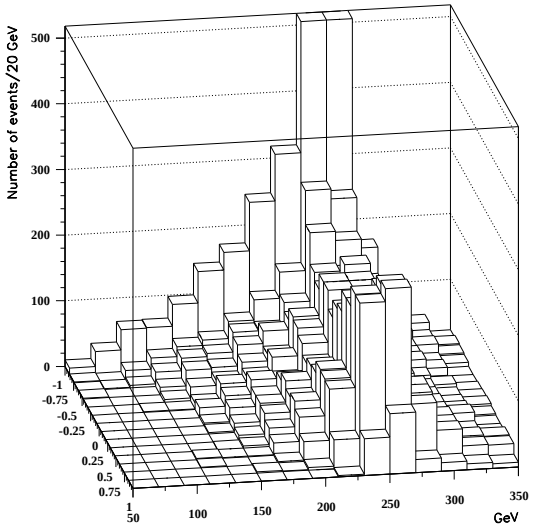

Figure 3.41: Correlation between the angular distribution and p_{t1} in events produced with ISR and FSR. MRST(h-g) used as PDF. No trigger cuts.

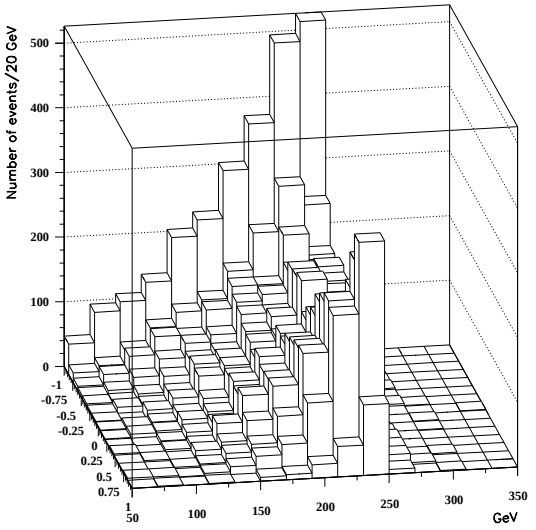

Figure 3.42: Correlation between the angular distribution and p_{t2} in events produced with ISR and FSR. MRST(h-g) used as PDF. No trigger cuts.

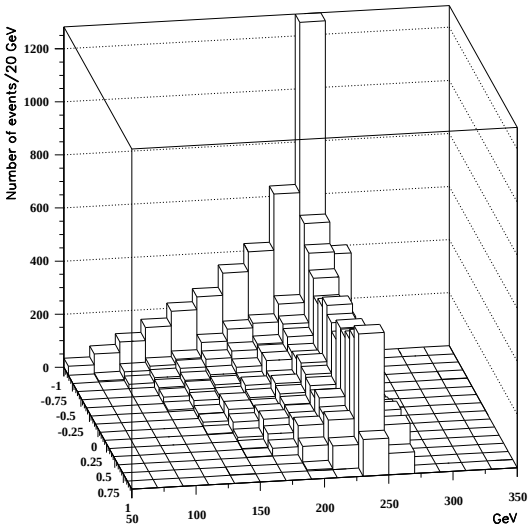

Figure 3.43: Correlation between the angular distribution and p_{t1} in events produced with no radiation. CTEQ5L used as PDF. No trigger cuts.

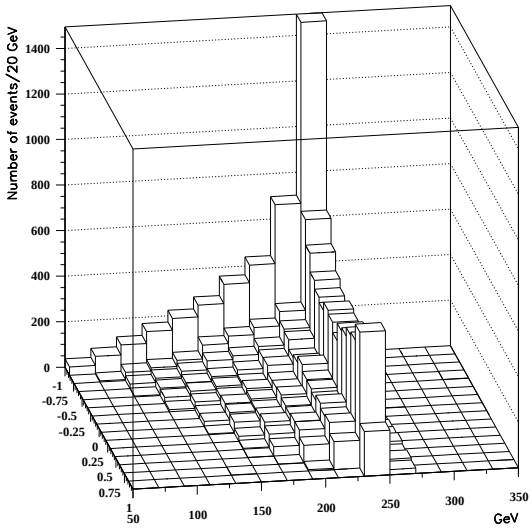

Figure 3.44: Correlation between the angular distribution and p_{t2} in events produced with no radiation. CTEQ5L used as PDF. No trigger cuts.

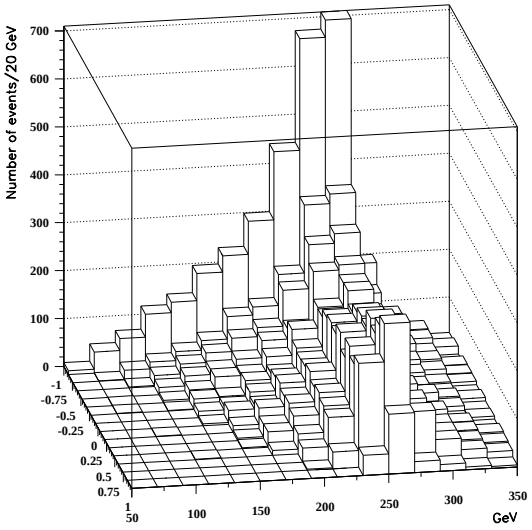

Figure 3.45: Correlation between the angular distribution and p_{t1} in events produced with only ISR. CTEQ5L used as PDF. No trigger cuts.

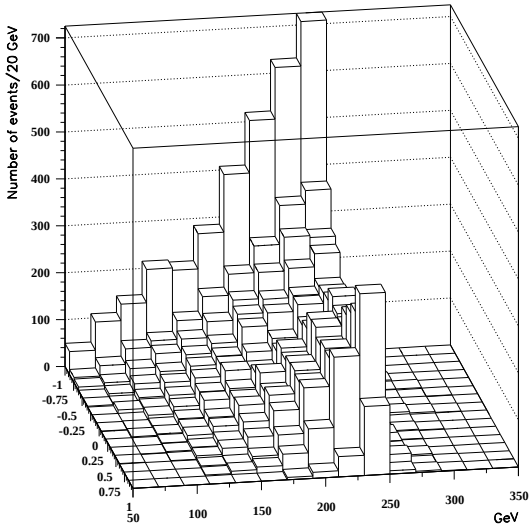

Figure 3.46: Correlation between the angular distribution and p_{t2} in events produced with only ISR. CTEQ5L used as PDF. No trigger cuts.

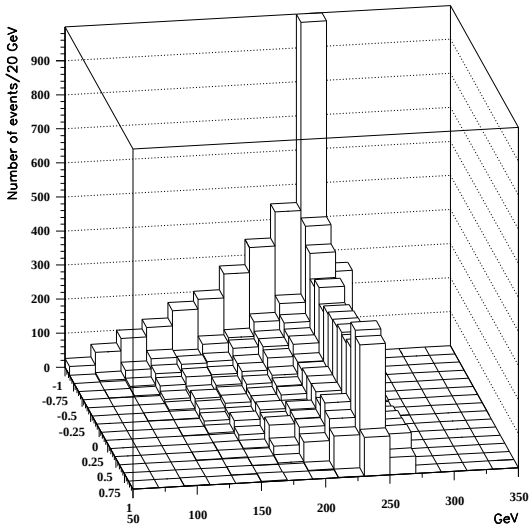

Figure 3.47: Correlation between the angular distribution and p_{t1} in events produced with only FSR. CTEQ5L used as PDF. No trigger cuts.

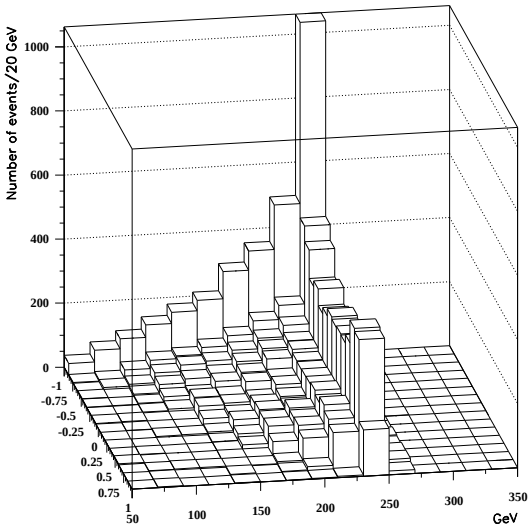

Figure 3.48: Correlation between the angular distribution and p_{t2} in events produced with only FSR. CTEQ5L used as PDF. No trigger cuts.

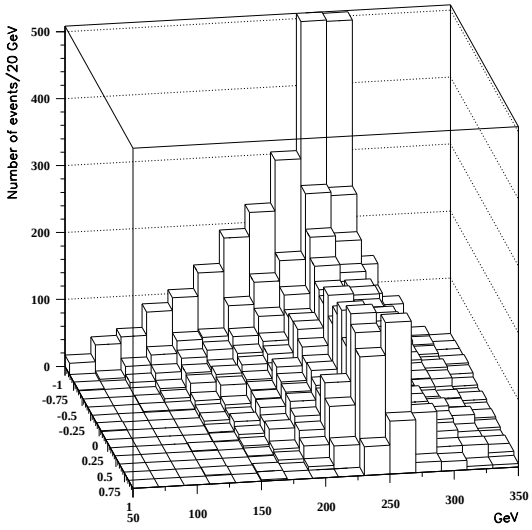

Figure 3.49: Correlation between the angular distribution and p_{t1} in events produced with ISR and FSR. CTEQ5L used as PDF. No trigger cuts.

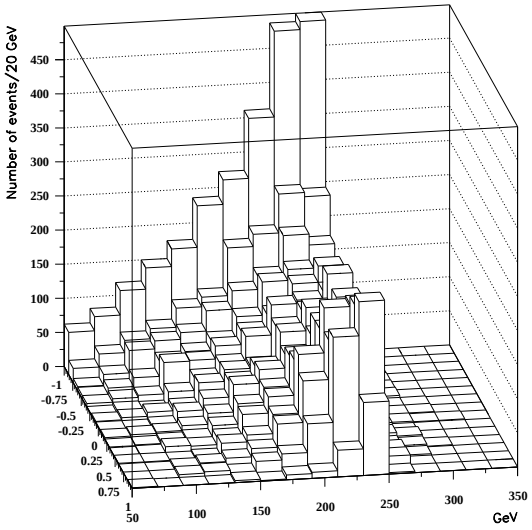

Figure 3.50: Correlation between the angular distribution and p_{t2} in events produced with ISR and FSR. CTEQ5L used as PDF. No trigger cuts.

Radiation	$\epsilon_{accetance}$	$\epsilon_{identification}$	$\epsilon_{trigger}$	$\epsilon_{overall}$
No Radiation	0.9002	0.8100	1.000	0.7292
Only ISR	0.8860	0.8100	0.9999	0.7176
Only FSR	0.6911	0.8100	0.9997	0.5596
ISR and FSR	0.6783	0.8100	0.9989	0.5488

Table 3.12: Different efficiencies for different scenarios described in the text. $\epsilon_{acceptance}$ is the acceptance, $\epsilon_{identification}$ is the lepton identification efficiency, $\epsilon_{trigger}$ is the effect of the trigger cuts on the efficiency and $\epsilon_{overall}$ is the overall efficiency. MRST(h-g) used as PDF.

Radiation	$\epsilon_{accetance}$	$\epsilon_{identification}$	$\epsilon_{trigger}$	$\epsilon_{overall}$
No Radiation	0.9096	0.8100	1.000	0.7368
Only ISR	0.8961	0.8100	0.9997	0.7256
Only FSR	0.7013	0.8100	0.9990	0.5675
ISR and FSR	0.6862	0.8100	0.9992	0.5554

Table 3.13: Different efficiencies for different scenarios described in the text. $\epsilon_{acceptance}$ is the acceptance, $\epsilon_{identification}$ is the lepton identification efficiency, $\epsilon_{trigger}$ is the effect of the trigger cuts on the efficiency and $\epsilon_{overall}$ is the overall efficiency. CTEQ5L used as PDF.

ID. If electrons/positrons are very badly measured, not meeting the requirments on $\frac{E}{p}$ i.e not matching the tracks in the ID, they are not considered as electron or positron candidates, leading to a fall in the acceptance. See tables 3.10 and 3.11, in addition to figures 3.21 and 3.22.

Tables 3.12 and 3.13 show the evolution of the overall or total efficiency for a 500 GeV graviton produced with MRST(h-g) and CTEQ5L (21140 and 18580 events generated, respectively).

The acceptance varies from 90% to 68% and 91% to 69% for MRST(h-g) and CTEQ5L, respectively. FSR causes the greatest losses of the acceptance. The reduction of the acceptance due to ISR is negligible. When a parton entering the hard process radiates a photon, less energy is available to produce a graviton. In our case this causes a loss of acceptance of order 1%.

By adding a lepton identification efficiency of 0.9 for each electron these efficiencies drop further. The overall efficiency varies from 73% to 55% and 74% to 56% for MRST(h-g) and CTEQ5L, respectively. The effect of trigger cuts on the overall efficiency is almost non-existing due to the high transverse momenta of the gravitons, which is good. The effect of the trigger cuts throws away only 0 to 24 signal events, depending on radiation scenario and PDF. But the effect on the background is not large either. The background events are not substantially reduced compared to the signal events. Nothing is gained by the trigger cuts set by the ATLAS detector. 34680 and 36170 Drell-Yan events are generated for MRST(h-g) and CTEQ5L respectively. This corresponds to a cut on the invariant mass of 350 GeV, and an integrated luminosity of 100 fb^{-1}. Tables 3.14 and

Radiation	$\epsilon_{accetance}$	$\epsilon_{identification}$	$\epsilon_{trigger}$	$\epsilon_{overall}$
No Radiation	0.6745	0.8100	1.000	0.5463
Only ISR	0.6828	0.8100	0.9994	0.5527
Only FSR	0.5297	0.8100	0.9995	0.4288
ISR and FSR	0.5340	0.8100	0.9989	0.4321

Table 3.14: Different efficiencies for different scenarios for the Drell-Yan background with a cut of 350 GeV on the invariant mass. $\epsilon_{acceptance}$ is the acceptance, $\epsilon_{identification}$ is the lepton identification efficiency, $\epsilon_{trigger}$ is the effect of the trigger cuts on the efficiency and $\epsilon_{overall}$ is the overall efficiency. MRST(h-g) used as PDF.

Radiation	$\epsilon_{accetance}$	$\epsilon_{identification}$	$\epsilon_{trigger}$	$\epsilon_{overall}$
No Radiation	0.6749	0.8100	1.000	0.5467
Only ISR	0.6857	0.8100	0.9995	0.5551
Only FSR	0.5308	0.8100	0.9992	0.4296
ISR and FSR	0.5353	0.8100	0.9990	0.4332

Table 3.15: Different efficiencies for different scenarios for the Drell-Yan background with a cut of 350 GeV on the invariant mass. $\epsilon_{acceptance}$ is the acceptance, $\epsilon_{identification}$ is the lepton identification efficiency, $\epsilon_{trigger}$ is the effect of the trigger cuts on the efficiency and $\epsilon_{overall}$ is the overall efficiency. CTEQ5L used as PDF.

3.15 show the evolution of the overall or total efficiency for the Drell-Yan background.

For CTEQ5L with ISR and FSR switched on, the total background above 350 GeV, i.e. not only inside a mass window around the graviton, is reduced with only 38 events! The number for the corresponding graviton is 15 events. This corresponds to an $\epsilon_{trigger}$ of 0.9990 and 0.9992 respectively. The transverse momentum distributions of the graviton and the background are given in figure 3.51. The trigger cuts set by ATLAS are not used in the rest of this study because we look at relatively high invariant masses.

There are striking differences between the signal and the background efficiencies when FSR is switched off. For the background, when there is no radiation or only ISR, the overall efficiency varies between 55-56% compared to the signal efficiency of 72-74%, depending on PDF. The difference between the efficiencies is smaller when FSR (alone or with ISR) is switched on. Now the corresponding efficiencies are 43% and 55-57%, respectively, depending on PDF. There are other differences as well. Unlike the graviton, the efficiency of the Drell-Yan background increases with ISR. This is due to the cut on the invariant mass set to 350 GeV. Lepton pairs with an invariant mass just below 350 GeV can pass this cut when ISR is added, because of the overall increase in transverse momentum of the lepton pairs. This is again due to the fact that the graviton is not produced at rest, as shown in section 3.7.2. More lepton pairs are reconstructed compared to cases without ISR. Thus ISR boost the rate of the low-mass state. Tables 3.16 and 3.17 show the number of reconstructed Drell-Yan events and their transverse momentum.

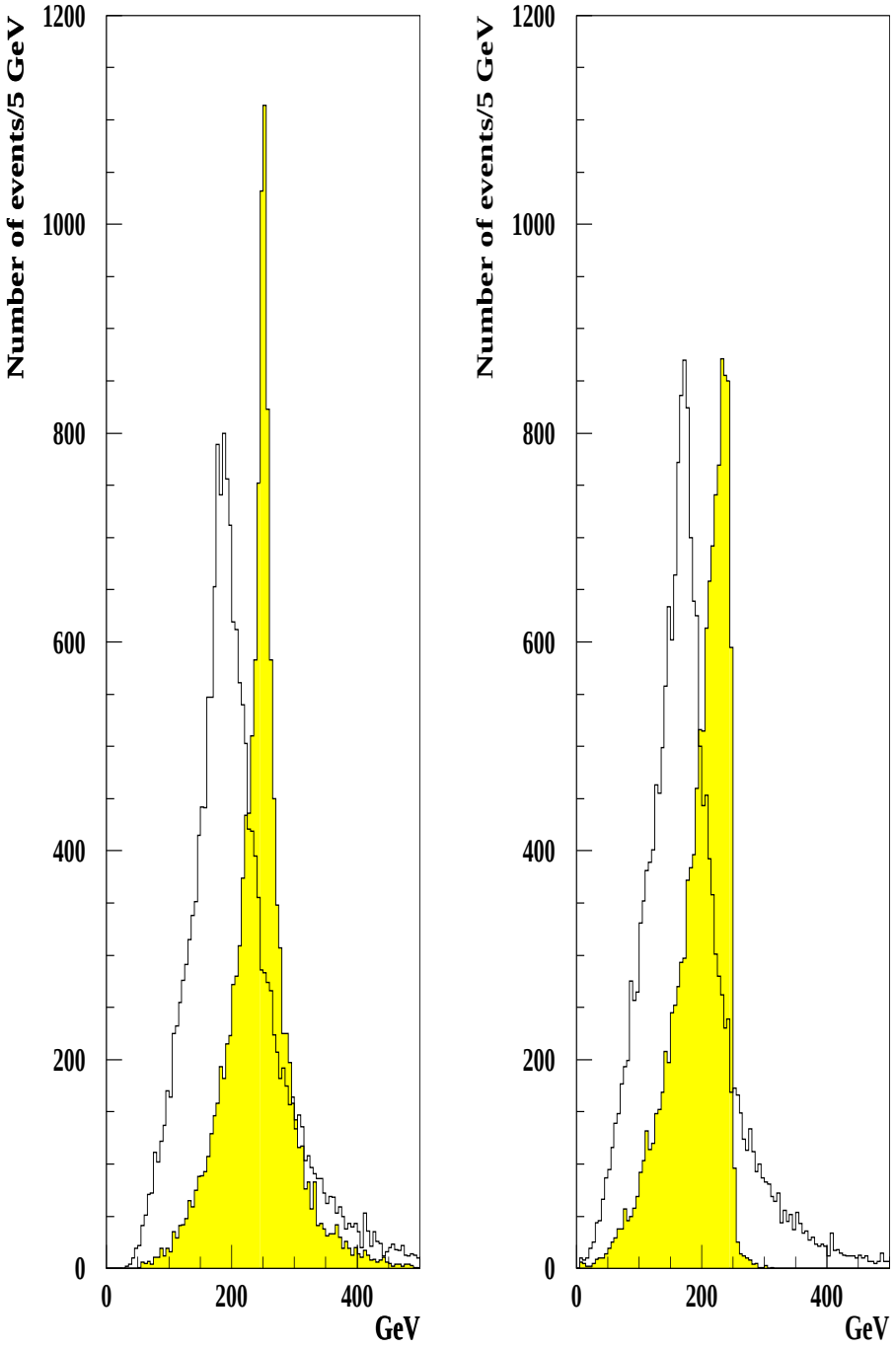

Figure 3.51: Distribution for p_{t1} (left) and p_{t2} (right) of a 500 GeV graviton (shaded histogram), and of the total Drell-Yan background with a cut on the invariant mass at 350 GeV. ISR and FSR switched on. CTEQ5L used as PDF. No trigger cuts used.

Radiation	N	$<p_{t1}>$ (GeV)	$<p_{t2}>$ (GeV)
No Radiation	23390	200.0	200.0
Only ISR	23680	220.7	188.6
Only FSR	18370	197.6	192.7
ISR and FSR	18520	214.6	181.4

Table 3.16: The mean values of p_{t1} and p_{t2} and number of events reconstructed, N, for different scenarios for the Drell-Yan background with a cut of 350 GeV on the invariant mass. MRST(h-g) used as PDF. No trigger cuts.

Radiation	N	$<p_{t1}>$ (GeV)	$<p_{t2}>$ (GeV)
No Radiation	24410	198.4	198.4
Only ISR	24800	217.5	187.1
Only FSR	19200	197.5	192.7
ISR and FSR	19360	212.2	180.5

Table 3.17: The mean values of p_{t1} and p_{t2} and number of events reconstructed, N, for different scenarios for the Drell-Yan background with a cut of 350 GeV on the invariant mass. CTEQ5L used as PDF. No trigger cuts.

A study of the effects of the $\frac{E}{p}$ requirements is done by full simulation which is beyond the scope of this study. Full simulation gives a realistic picture of how the detector responds. ATLFAST, which is a parametrization of full simulation studies, is not useful as a tool for understanding the detector. ATLFAST imposes cuts that seem too severe when FSR is switched on. The ratio $\frac{E}{p}$ lies between 0.8 and 1.2, see figures 3.52-3.53. Looser cuts yield a broader $\frac{E}{p}$ range. This could reduce the efficiency differences between the different scenarios.

3.7.6 Signal Description

The most obvious effect of radiation is a visible one. In figures 3.54-3.57 18580 events are generated with a graviton of 500 GeV at an integrated luminosity of 100fb^{-1}, and 65950, 7588 and 1424 events are generated for the masses 1000, 1500 and 2000 GeV, respectively, corresponding to an integrated luminosity of 10000 fb^{-1} for different radiation scenarios. The figures 3.58-3.60 show the masses 1000, 1500 and 2000 GeV produced at a luminosity of 100fb^{-1}. CTEQ5L is used as PDF. All the parameters are calculated inside a mass window of $\pm$60 GeV around the graviton. The acceptance for the total number of the reconstructed signal events for the corresponding masses is given in table 3.18.

The acceptance falls with higher graviton mass, see table 3.18. Explaining this fall of acceptance requires a full simulation study. However, the requirements on the ratio $\frac{E}{p}$ could explain this reduction. When there is no radiation, or only ISR the acceptance has a maximum at 1 TeV. The reason for this increase of efficiency is not clear since ATLFAST is only a parameterization of full simulation results. It might be that the

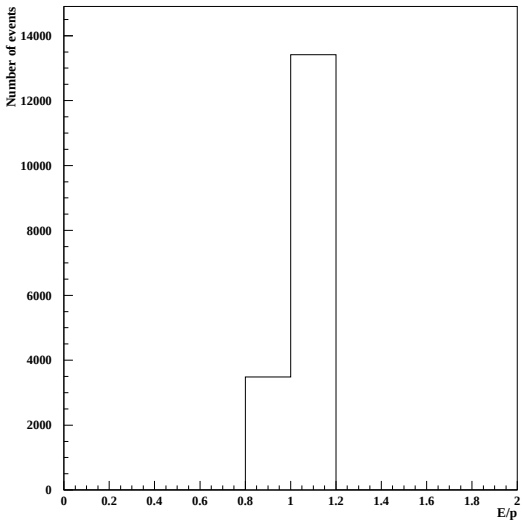

Figure 3.52: The ratio $\frac{E}{p}$ for leptons produced without radiation. CTEQ5L used as PDF. No trigger cuts.

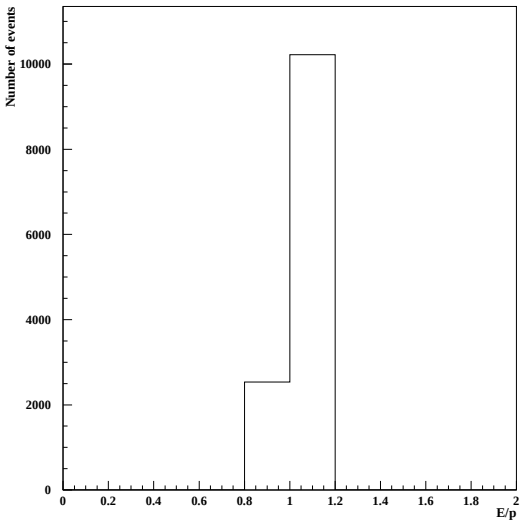

Figure 3.53: The ratio $\frac{E}{p}$ for leptons produced with ISR and FSR. CTEQ5L used as PDF. No trigger cuts.

Radiation	500 GeV	1000 GeV	1500 GeV	2000 GeV
No Radiation	0.9096	0.9337	0.8871	0.8202
Only ISR	0.8961	0.9102	0.8552	0.7887
Only FSR	0.7013	0.6552	0.5841	0.5154
ISR and FSR	0.6862	0.6370	0.5604	0.5084

Table 3.18: The acceptance for the total number of reconstructed signal events for different scenarios and invariant masses. CTEQ5L used as PDF.

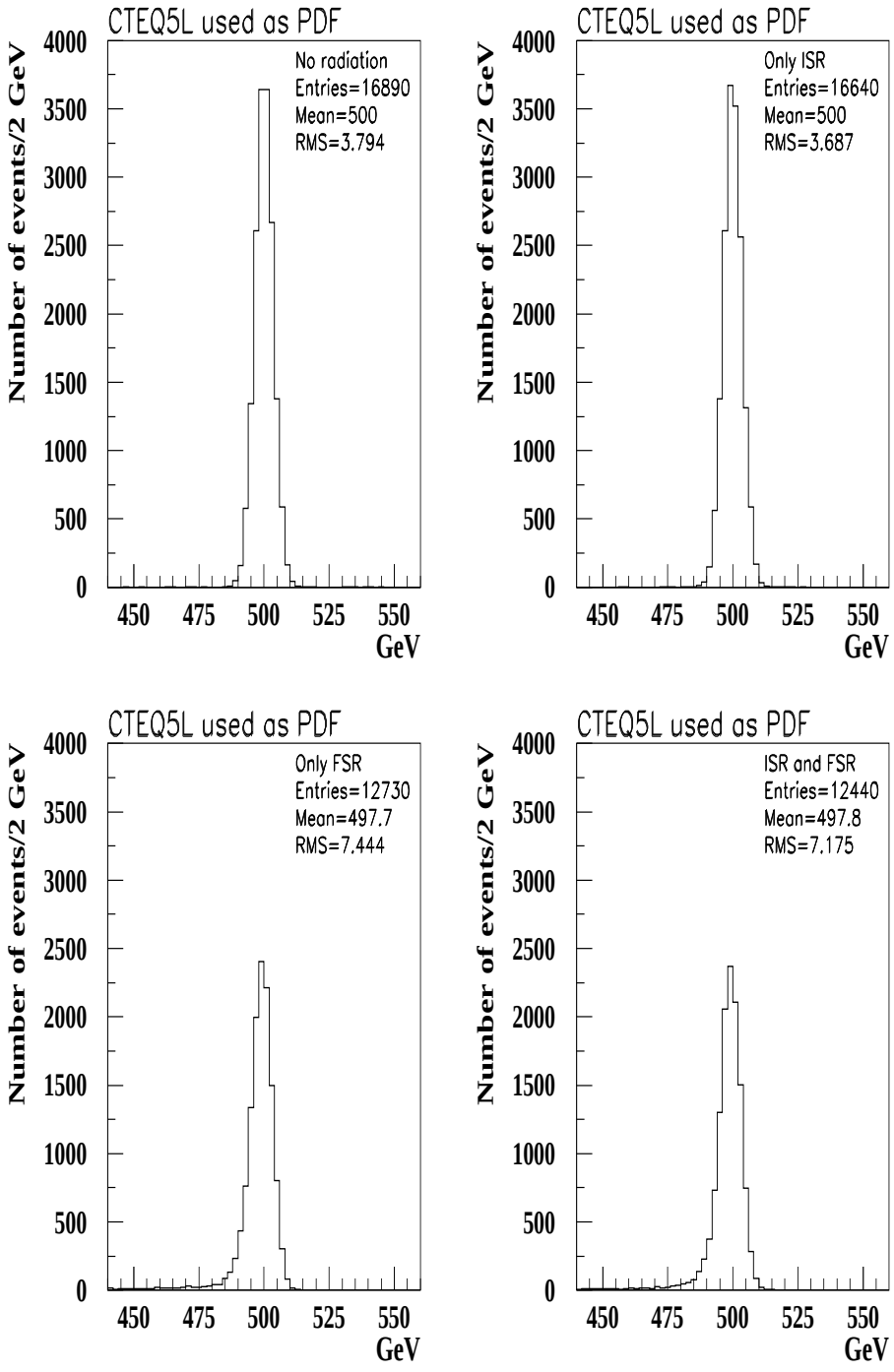

Figure 3.54: Graviton resonance of 500 GeV produced in different scenarios. Integrated luminosity set to 100 fb^{-1}. No trigger cuts applied.

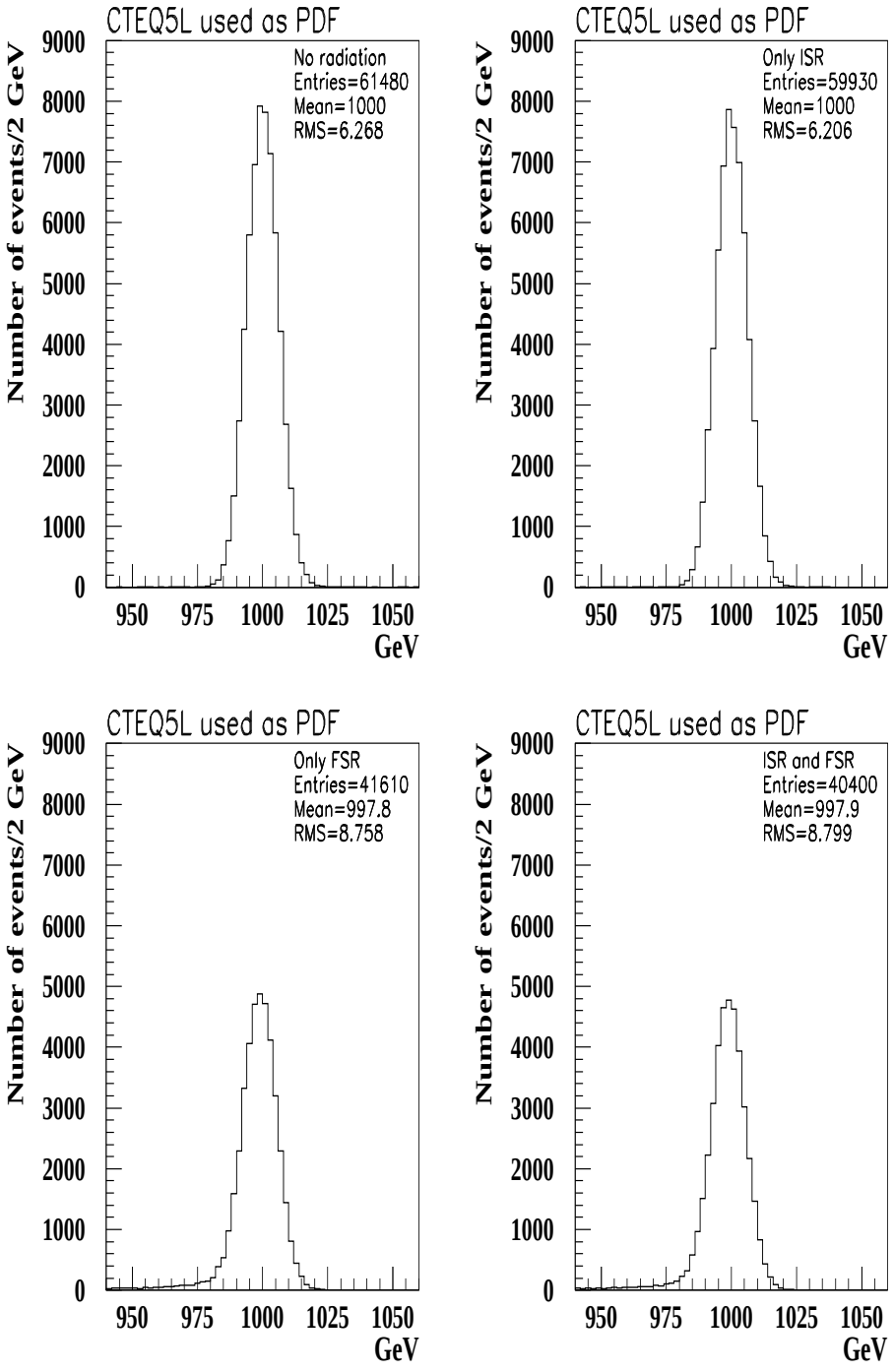

Figure 3.55: Graviton resonance of 1000 GeV produced in different scenarios. Integrated luminosity artificially set to 10000 fb^{-1}. No trigger cuts applied.

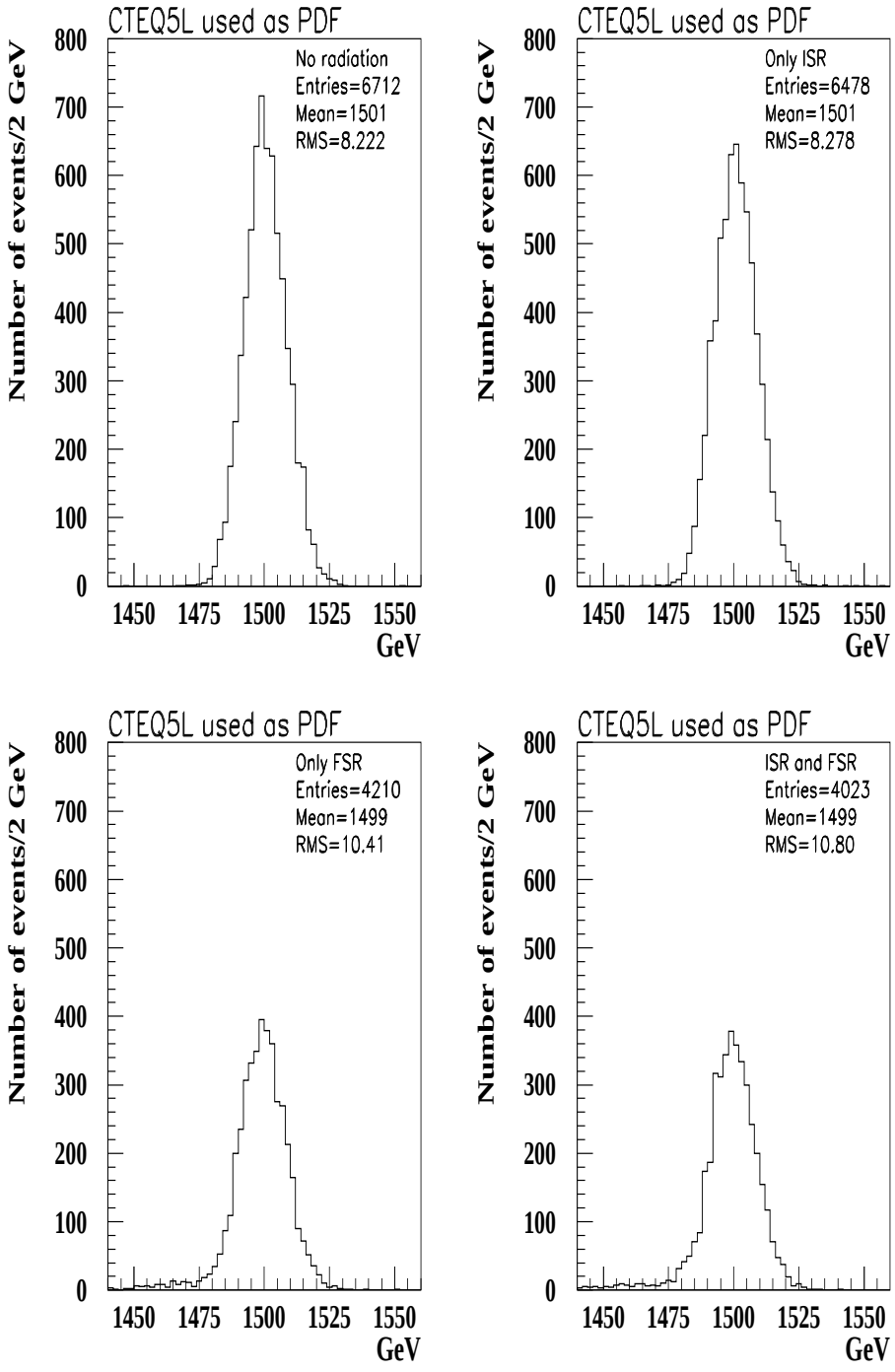

Figure 3.56: Graviton resonance of 1500 GeV produced in different scenarios. Integrated luminosity artificially set to 10000 fb^{-1}. No trigger cuts applied.

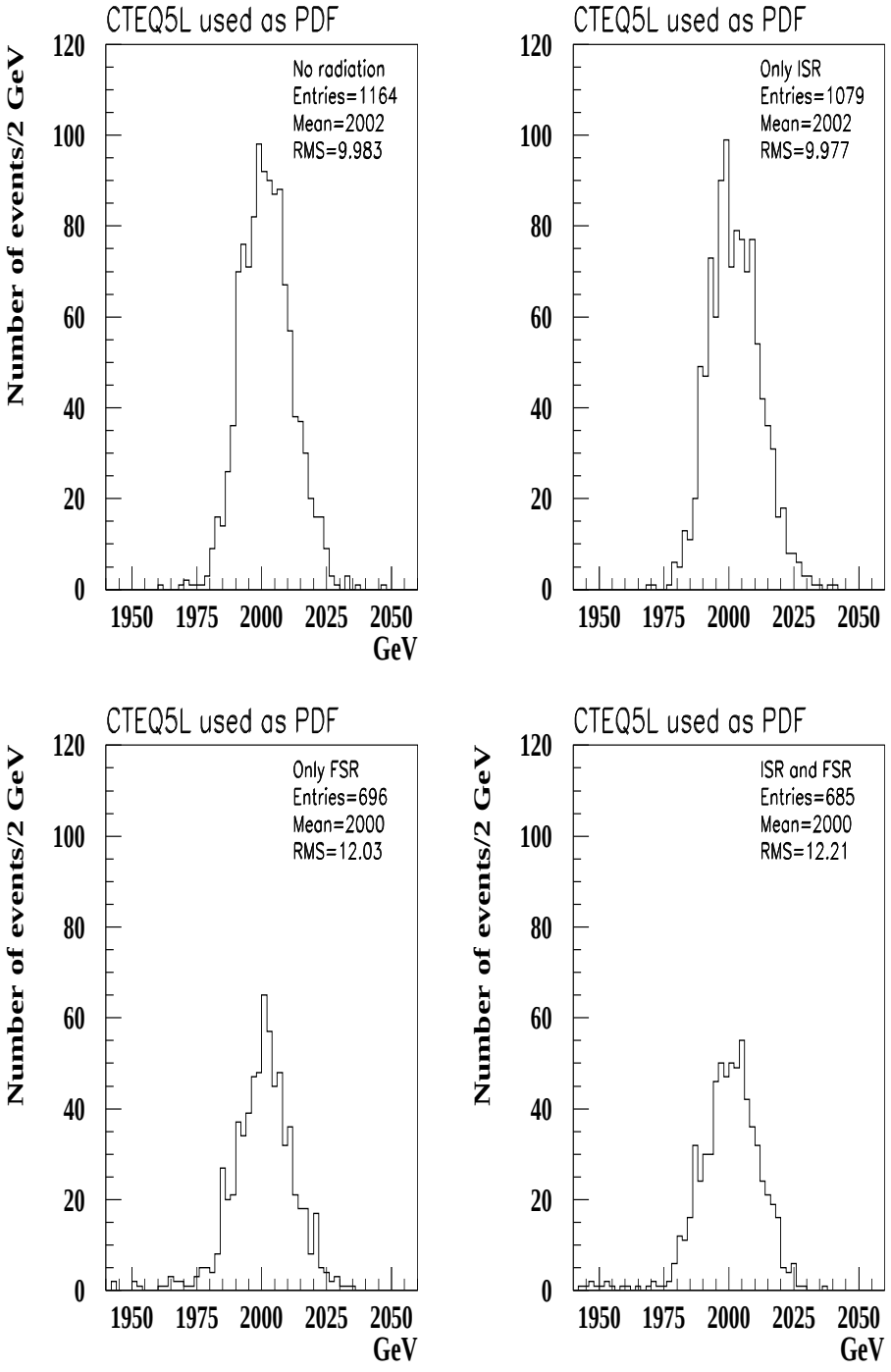

Figure 3.57: Graviton resonance of 2000 GeV produced in different scenarios. Integrated luminosity artificially set to 10000 fb^{-1}. No trigger cuts applied.

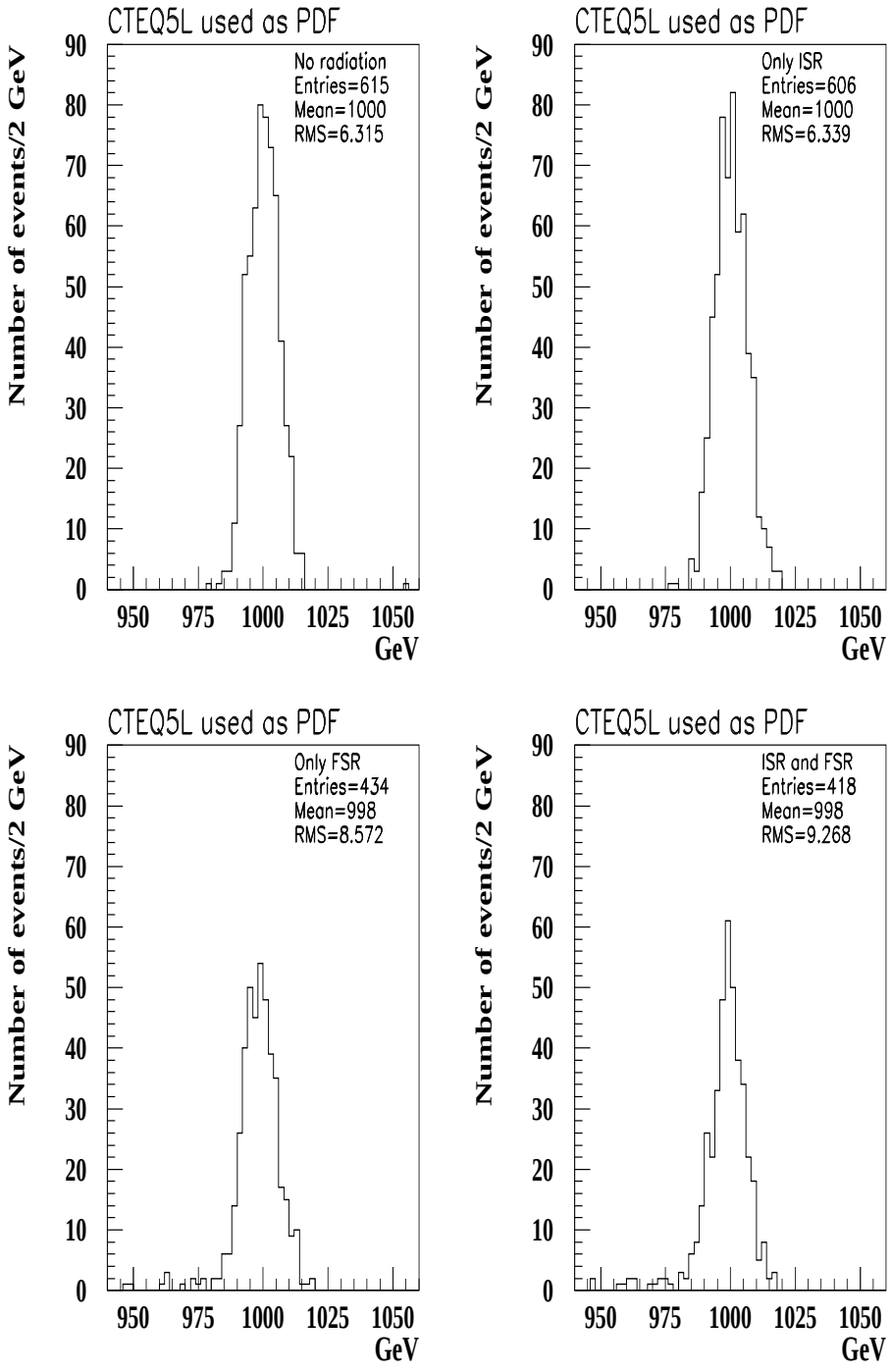

Figure 3.58: Graviton resonance of 1000 GeV produced in different scenarios. Integrated luminosity set to 100 fb^{-1}. No trigger cuts applied.

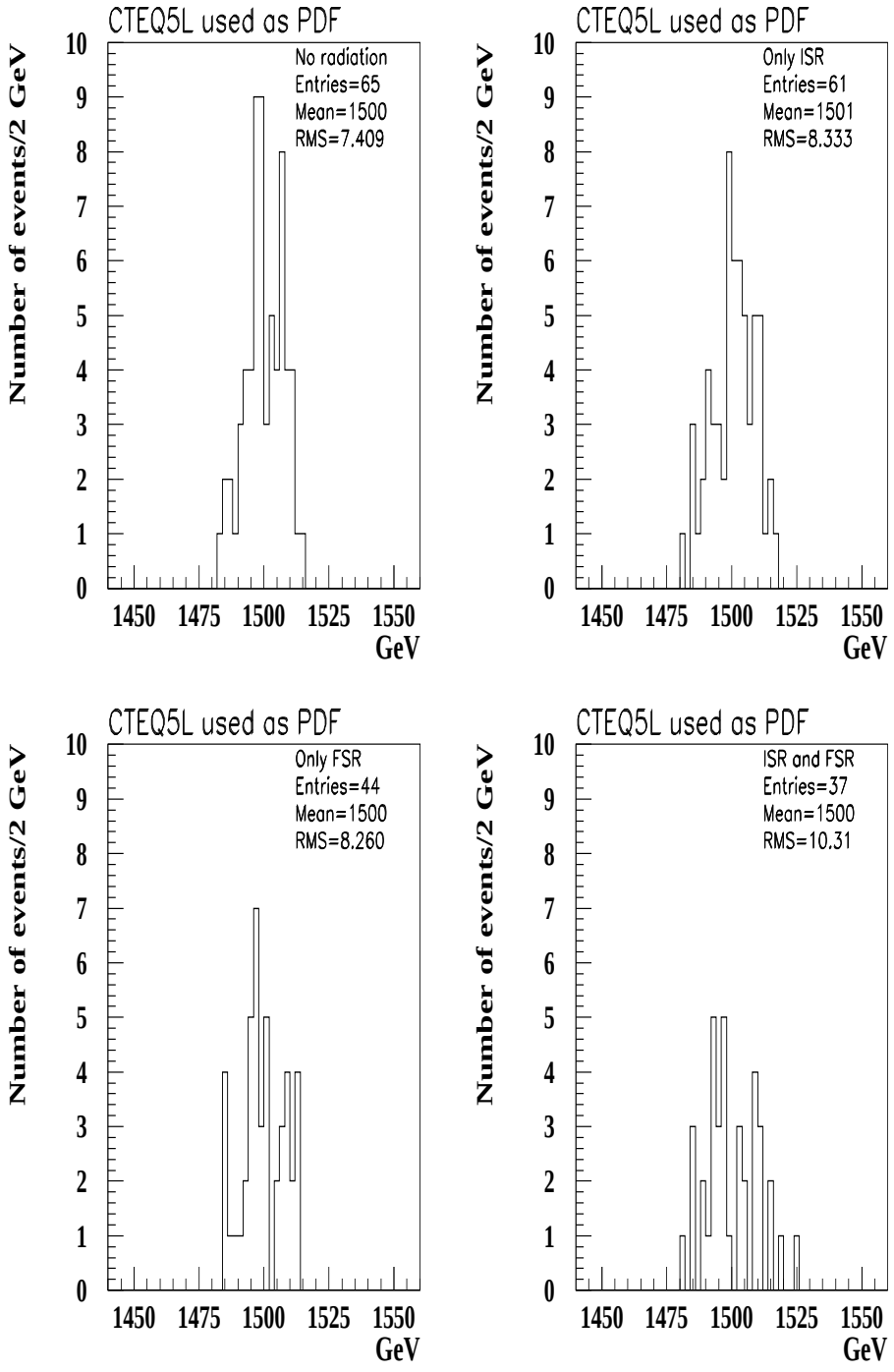

Figure 3.59: Graviton resonance of 1500 GeV produced in different scenarios. Integrated luminosity set to 100 fb^{-1}. No trigger cuts applied.

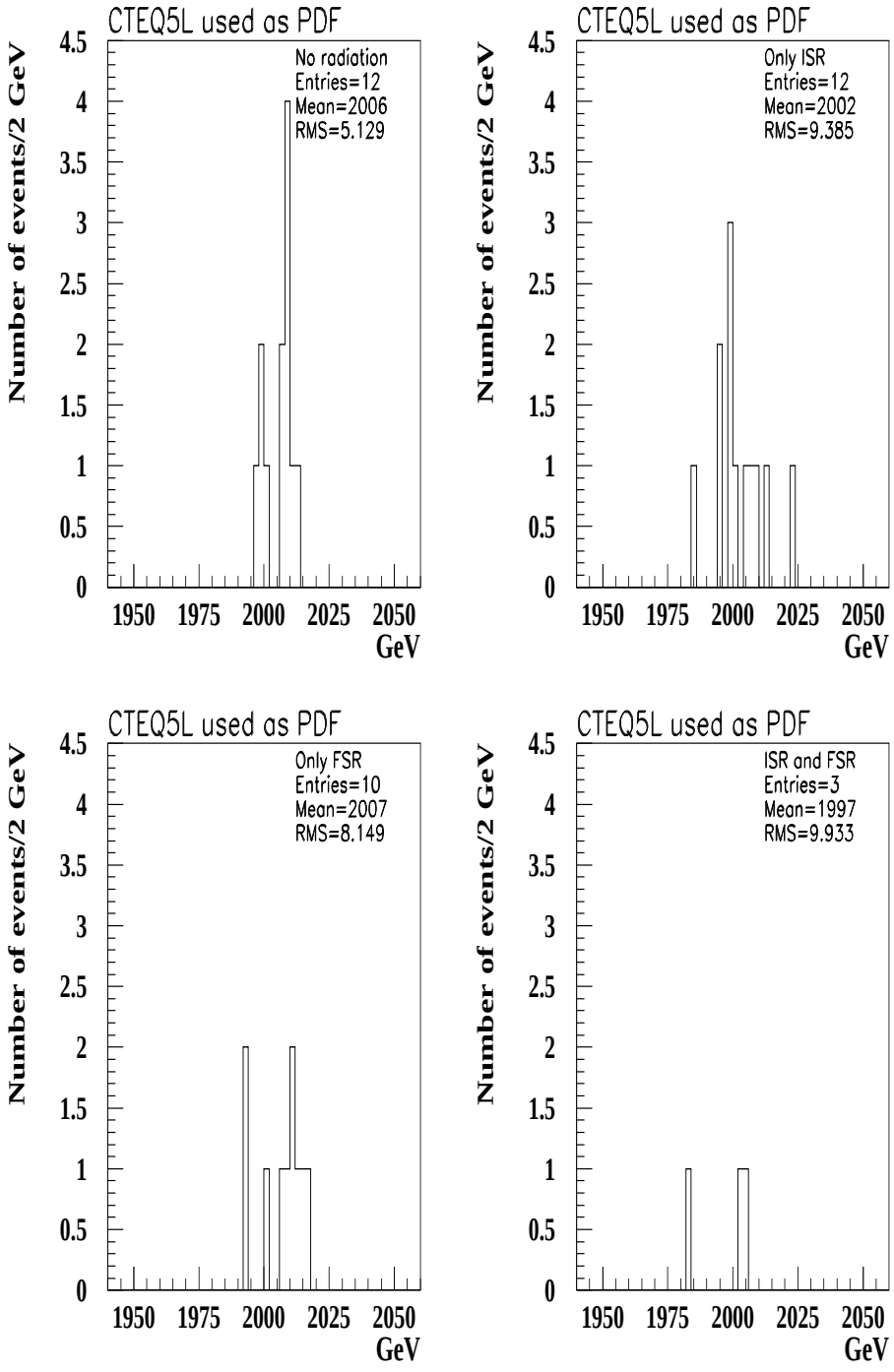

Figure 3.60: Graviton resonance of 2000 GeV produced in different scenarios. Integrated luminosity set to 100 fb^{-1}. No trigger cuts applied.

ATLAS detector is optimized in this region. After 1 TeV, momentum measurement becomes worse with higher masses while energy measurement continues to improve. Since momentum measurement becomes poorer less events pass the requirements on $\frac{E}{p}$, and the acceptance drops.

Switching on FSR alone makes the leptons radiate in their journey through the detector. Since energy loss due to FSR is not taken into account by the ID this leads to uncorrect measurement of the lepton momentum. So the momentum measurement is poor from the beginning and there is no maximum at 1 TeV. Requirements on $\frac{E}{p}$ are not met, and it get worse with higher masses since the precision of the momentum measurement decreases. The emitted photons can in turn convert into a electron and positron pair. Photon conversions are discussed in section 3.9.4.

ISR happens before the leptons are created and does not affect the momentum measurement of the leptons and the loss of acceptance is comparable, as discussed in section 3.7.5, to the case without any radiation for the 500 GeV and 1 TeV mass points. However, the losses are larger for the 1.5 TeV and 2 TeV mass points. This is again due to poorer momentum measurement and requirements on $\frac{E}{p}$ not being met. The acceptance is reduced above all by FSR, see table 3.18. FSR also changes the shape of the resonances, see figures 3.54-3.57 which show the gravitons inside a mass window of $\pm$60 GeV.

FSR reduces the transverse momentum spectra of the leptons because of the photons radiated. This lowers the mean value of the invariant mass since one has to add back on $e^-e^+\gamma$ or $e^-e^+\gamma\gamma$, and not e^-e^+ in order to get the original graviton mass. Since the invariant mass of the e^-e^+ pairs is reduced, long tails of events far below the graviton mass are produced, causing the fall in the average invariant mass. Naturally, the number of signal events inside the mass window $\pm$60 GeV is smaller than the total number of events reconstructed, since the mass window does not take into account the whole tail. In table 3.18 the acceptance of the total reconstructed events is 69% for a graviton of 500 GeV when both ISR and FSR are switched on. For 1000, 1500 and 2000 GeV the numbers are 64, 56 and 51%, respectively. In figures 3.54-3.57, i.e. inside a mass window of $\pm$60 GeV around the graviton, the acceptance is reduced to 67, 61, 53 and 48%, respectively. The tail causes changes in Root Mean Square or RMS[2]. Thus a larger σ_m is expected when we fit a resonance produced with FSR to a gaussian.

While the FSR reduces the transverse momentum, ISR increases it. Switching on the ISR together with FSR increases the mean value of the graviton masses of 500 and 1000 GeV inside the mass window, see figures 3.54-3.55. At higher masses the increase of transverse momentum is not sufficient in order to compensate for the decrease of the mean value of the invariant mass, see figures 3.56-3.57. A smaller mass window is needed to increase this value. When only ISR is switched on it does not affect the shape of the invariant mass. No tails are produced, and the mass window takes into account almost all the reconstructed events. This is also true for the case without radiation.

Since the gaussian fails to take the tail into account it is no longer convenient for fitting the resonance when FSR is switched on. As a consequence of this we get an even lower

[2]RMS is a statistical measure of the magnitude of a varying quantity.

number of signal events. Other functions are used to fit the resonance produced with FSR. In order to determine the goodness of a fit we introduce the chi-square or χ^2 defined as:

$$\chi^2 = \sum_{i=1}^{N} (\frac{x_i - \mu_i}{\sigma_i})^2 \tag{3.14}$$

where x_i are the measured variables, μ_i are the theoretical mean values and σ_i are the standard deviations. χ^2 gives the discrepancies or fluctuations between measured and expected data. A good fit is characterized by:

$$\frac{\chi^2}{NDF} \approx 1 \tag{3.15}$$

where NDF is the Number of Degrees of Freedom which is related to the number of independent variables of the measurement.

The following functions, in addition to the gaussian, are used to describe the resonance:

The Breit-Wigner [6] probability function is defined as:

$$f(x;\Gamma,M) = \frac{1}{2\pi}\frac{\Gamma}{(\Gamma^2/4)+(x-M)^2} \tag{3.16}$$

where M is the mass and Γ the observed width of the resonance. The latter is defined as $\Gamma = 2.35\sigma_m$ [7].

A function that takes into account the radiative losses due to the emission of photons is defined as [9]:

$$f(x;x_0,\sigma_x^2,\sigma_{tail}^2) = \frac{2}{\sigma_x(\sqrt{2\pi}+\pi\sigma_{tail})} \begin{cases} e^{-\frac{-(x-x_0)^2}{2\sigma_x^2}} & x > x_0 \\ \frac{1}{1+\left(\frac{x-x_0}{\sigma_x\sigma_{tail}}\right)^2} & x < x_0 \end{cases} \tag{3.17}$$

x_0 is the position of the peak maximum (equivalent to the mean value of the Gaussian). σ_x is the experimental mass resolution. σ_{tail} fits the tail of the resonance.

Graviton resonances of 500, 1000, 1500 and 2000 GeV are fitted to these functions. No trigger cuts are applied and ISR & FSR are switched on in order to obtain the most realistic situation. CTEQ5L is used as PDF. The luminosity is $100fb^{-1}$ for the 500 GeV resonance and $10000fb^{-1}$ for the rest. The results are shown in figures 3.61-3.63.

Since FSR produces tails, the peaks become asymmetric making them difficult to fit by a symmetric function like a gaussian or a Breit-Wigner. In the case of the gaussian we see that for a graviton of 500 GeV it fails to take into account the tail at around 475 GeV as well as the top of the signal in figure 3.61. It underestimates the number of signal events. But as the masses increase the tails become longer and longer, spreading out the events more evenly. Thus around 975 GeV the tail is almost invisible for a 1

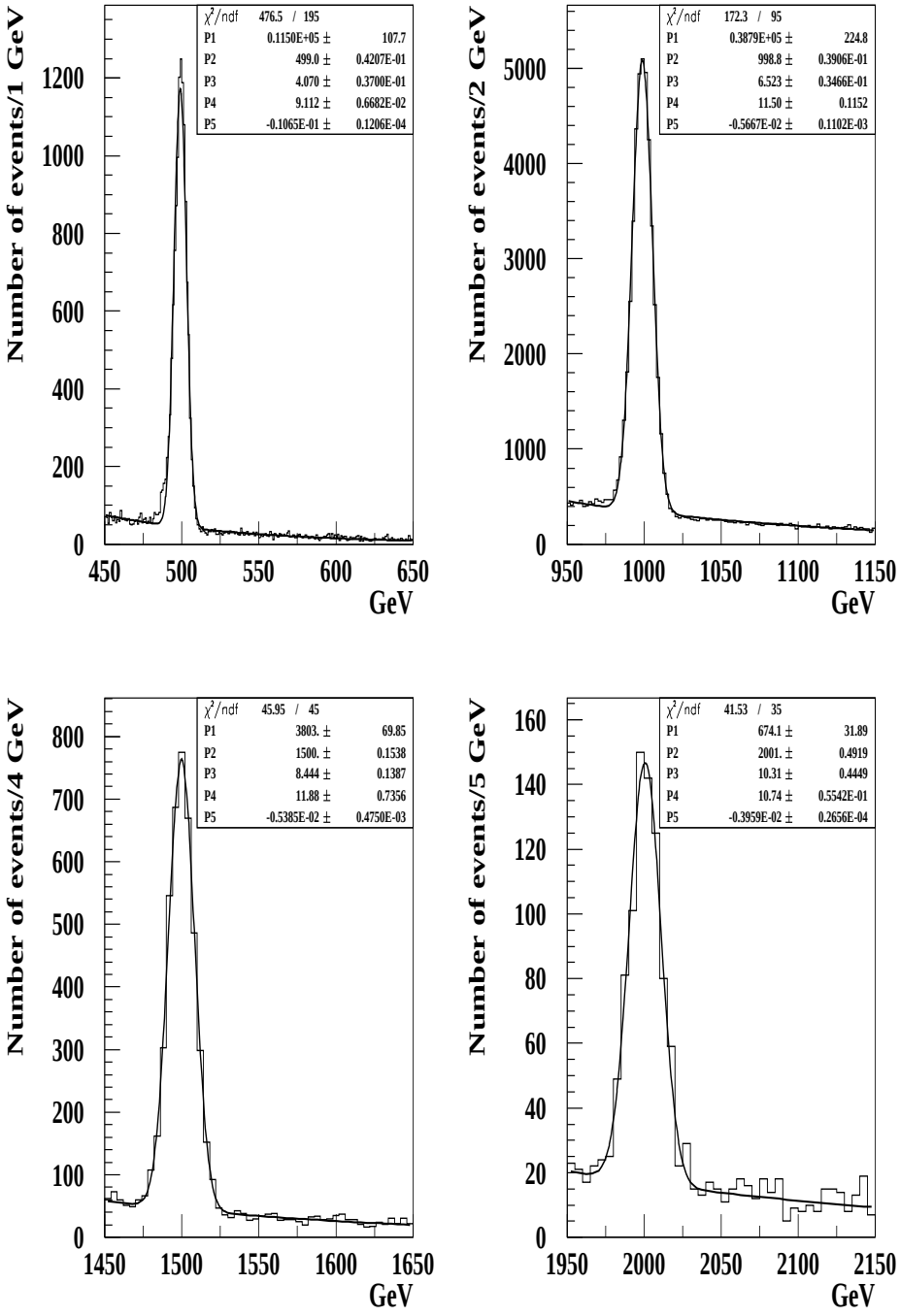

Figure 3.61: Graviton resonance invariant masses fitted with a gaussian. ISR and FSR switched on. The 500 GeV point (with background) corresponds to an integrated luminosity of 100 fb^{-1}, while the other points (with backgrounds) are artificially produced with an integrated luminosity of 10000 fb^{-1}. CTEQ5L used as PDF. No trigger cuts applied.

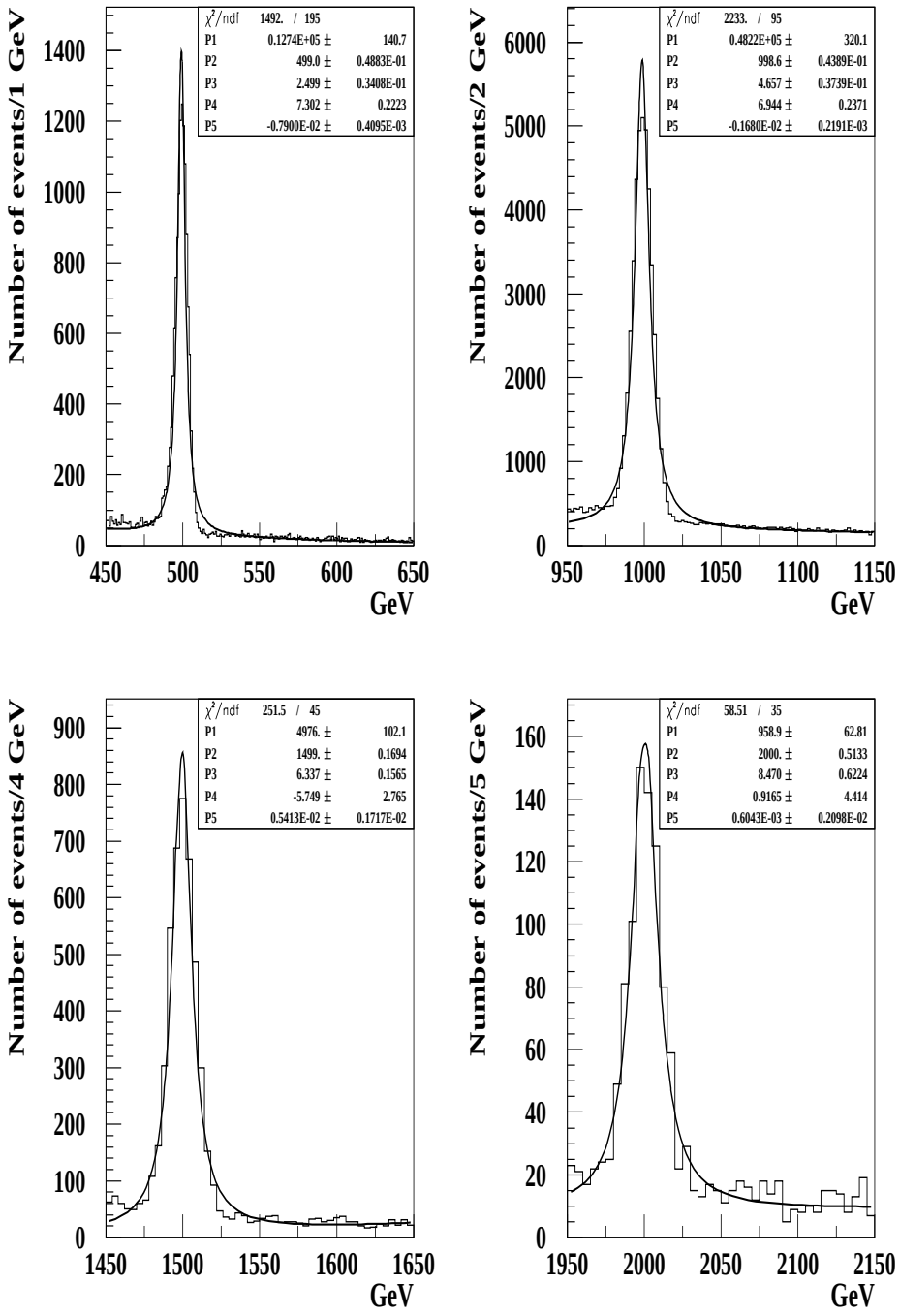

Figure 3.62: Graviton resonance invariant masses fitted with a Breit-Wigner distribution. ISR and FSR switched on. The 500 GeV point (with background) corresponds to an integrated luminosity of 100 fb^{-1}, while the other points (with backgrounds) are artificially produced with an integrated luminosity of 10000 fb^{-1}. CTEQ5L used as PDF. No trigger cuts applied.

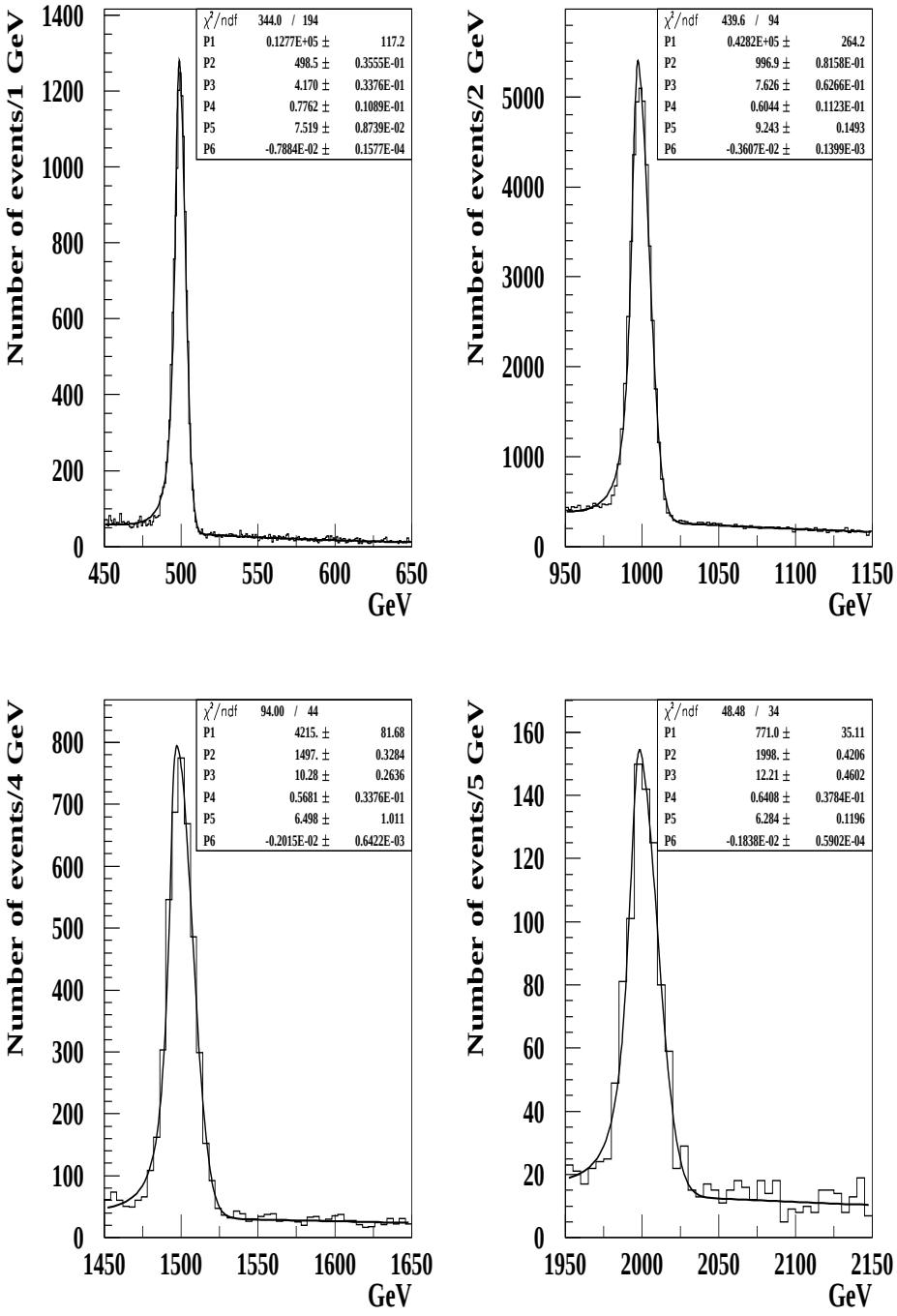

Figure 3.63: Graviton resonance invariant masses fitted with function 3.17. ISR and FSR switched on. The 500 GeV point (with background) corresponds to an integrated luminosity of 100 fb^{-1}, while the other points (with backgrounds) are artificially produced with an integrated luminosity of 10000 fb^{-1}. CTEQ5L used as PDF. No trigger cuts applied.

TeV graviton. At higher masses it is indistinguishable from the background. The χ^2 becomes almost one at the masses of 1500 and 2000 GeV. The gaussian becomes more and more accurate with increasing mass.

The Breit-Wigner distribution, in figure 3.62 fits the resonance even poorer than the gaussian. For the 500 GeV graviton it misses the mark completly at 525 GeV. This poor description of the right side of the graviton is also apparent for the other masses. It fails to describe the top of the signals and the description of the background becomes poorer as well. The χ^2 of all the fits is very poor and the parameters extracted are not reliable.

While the gaussian underestimates the signal, the asymmetric function 3.17, takes the tail into account and the number of signal events increases. However the tail is still poorly described, see the plots of figure 3.63. The function 3.17 overestimates tails since there is a gap between the fits and the tails. The poor description of the tail underestimates the mean values and overestimates the σ_m's. An overestimation of the signal also occurs. All the gravitons in figure 3.63, except for the graviton at 1500 GeV, have more events than the gravitons in figure 3.61. The fits are poorer compared with the gaussian fits except for the case of the 500 GeV graviton where the χ^2 is 1.8 compared to 2.4 for the gaussian fit. The function 3.17 is more suitable for graviton masses below 500 GeV where the tails are thicker. In addition using function 3.17 gives a much larger mass window, since the tails stretches several σ on the lefthand side of the graviton. More background than signal is gained leading to a more conservative significance.

The function that describes the resonances most correctly, when FSR is switched on, is still the gaussian. A systematic error arises because of the poor tail description as well as a poor description of the top of the signal. This systematic error can be determined by counting events inside a mass window of $\mu \pm 3\,\sigma_m$ and subtracting the events obtained by fitting. In this way the part of the events which escaped the fit at the tail and at the top of the signal can be accounted for inside a mass window of $\mu \pm 3\,\sigma_m$:

$$\Delta N = |N_{count} - N_{fit}|. \tag{3.18}$$

This also gives an error in the significance and the total efficiency given by:

$$\Delta S = \frac{\Delta N}{\sqrt{N_B}} \tag{3.19}$$

$$\Delta \epsilon = \frac{\Delta N}{N_{count}} \tag{3.20}$$

The analysis in section 3.7.8 makes use of a gaussian, in addition to taking into account the systematics errors. The whole tail can not be accounted for since it streches several σ_m outside a given mass window, leading to a fall of efficiency. Thus FSR causes a loss of efficiency in two ways: Large parts of the FSR tails are outside the given mass windows and can not be accounted for. Secondly, $\frac{E}{p}$ requirements are not met, leading to reduction of efficiency, compared to other radiation scenarios for a given mass point.

In addition, the efficiency is also reduced with higher masses in all the radiation scenarios. This might also be explained by the ratio $\frac{E}{p}$, however, a full simulation study is required in order to make a certain conclusion.

3.7.7 Background Description

The Drell-Yan background is rather well described by an exponential in all the cases discussed above. In figure 3.64 the χ^2 varies between approximately 1.0 and 1.3. The background efficiency evolves as according to table 3.14 and 3.15 in section 3.7.5. A cut of 350 GeV is made on the invariant mass, and 36170 events are generated.

3.7.8 Results

In this section discovery mass limits are reached for the graviton produced with no radiation, only FSR and with ISR & FSR. No trigger cuts are used and MRST(h-g) and CTEQ5L are used as PDFs. Graviton masses between 500 GeV and 2200 GeV are generated. The 500 GeV mass point (with corresponding background) is produced at an integrated luminosity of 100 fb^{-1}, and the rest of the mass points (with corresponding backgrounds) are produced at an integrated luminosity of 10000 fb^{-1}. The signal and the background are fitted to a gaussian and an exponential, respectively. As expected the efficiencies drop. These are given in tables 3.19 and 3.20 where ISR and FSR are switched on. Tables for the cases of no radiation and only FSR are in appendix A. MRST(h-g) yields more signal events than CTEQ5L.

In the case of no radiation the acceptance of the mass point of 500 GeV is exactly the same as was found in section 3.7.1, where the total number of reconstructed events are given, namely 90 and 91% for MRST(h-g) and CTEQ5L, respectively. This is expected since gravitons produced without radiation (or only ISR) do not have tails. This compatibility is not found when FSR is switched on. Because of the tails the fitting procedure fails to take into account all the signal and hence the acceptance of the total reconstructed events found in section 3.7.3 (only FSR) is higher than obtained by fitting the signal inside a mass window of $\pm 3\sigma_m$. When only FSR is switched on the acceptance is 69 and 70% for MRST(h-g) and CTEQ5L respectively in section 3.7.3. By fitting the acceptance is reduced by 5%. In the case of both ISR and FSR switched on, the loss by fitting is 6 and 7% repectively for MRST(h-g) and CTEQ5L compared to section 3.7.4.

The total efficiencies obtained by fitting the signal above the background are shown in the figures 3.65-3.72. Since no trigger cuts are used the acceptance is obtained by dividing the total efficiency, given in table 3.19 and 3.20 (and the tables in the appendix A), by a factor 0.81, corresponding to the identification efficiency. All the plots are fitted with a polynominal of second order. The possible reason for the loss of efficiency due to higher graviton mass is discussed in section 3.7.6.

The systematic errors, obtained using equations 3.18-3.20, are given in tables 3.21 and 3.22. The error in efficiency caused by the error in fitting is low, and varies from 0 to 4% for all masses. The tails outside the mass windows are not accounted for. Two

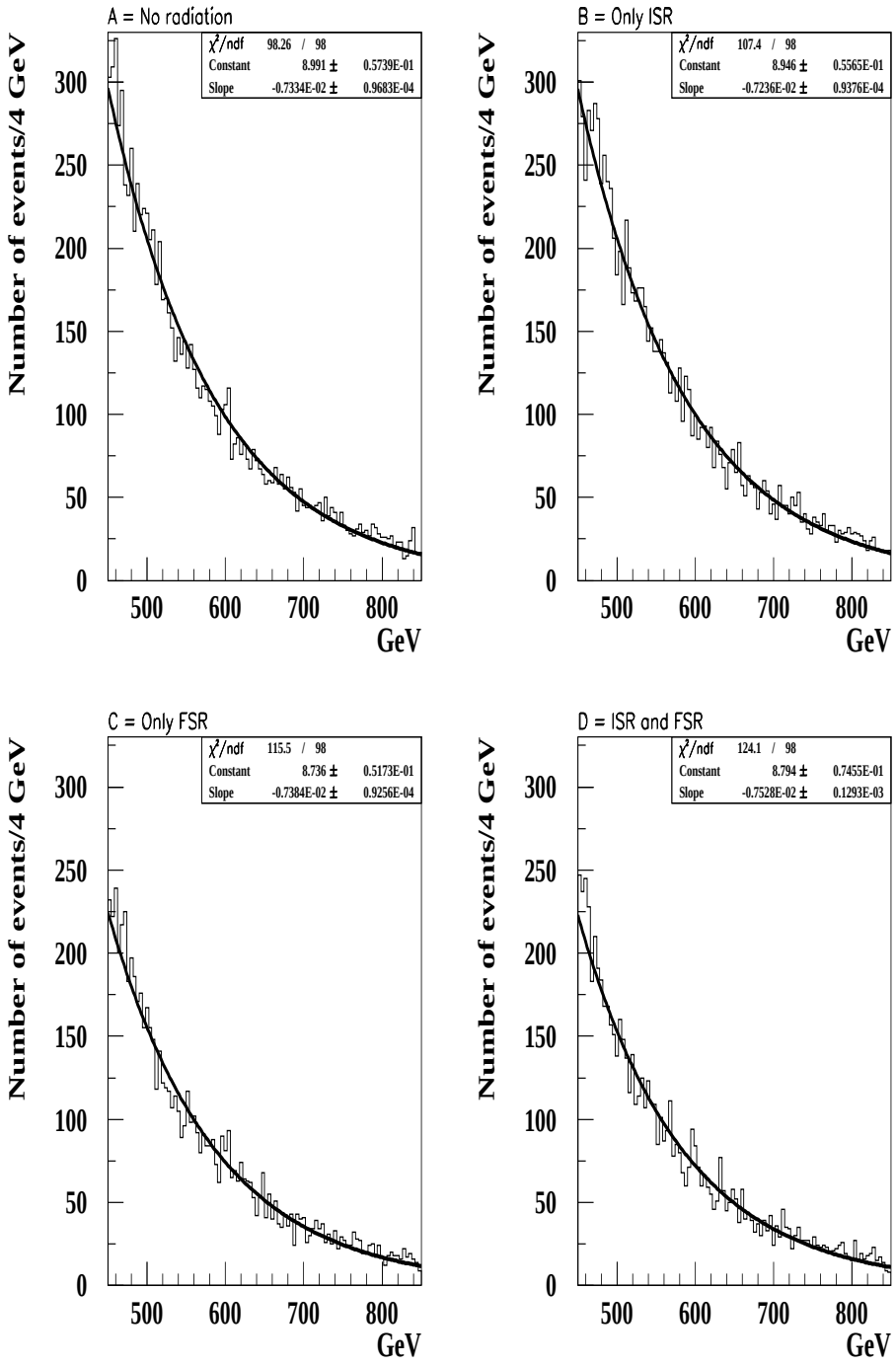

Figure 3.64: The Drell-Yan background, with a 350 GeV cut on the invariant mass, produced in different scenarios. Integrated luminosity set to 100 fb^{-1}. No trigger cuts applied.

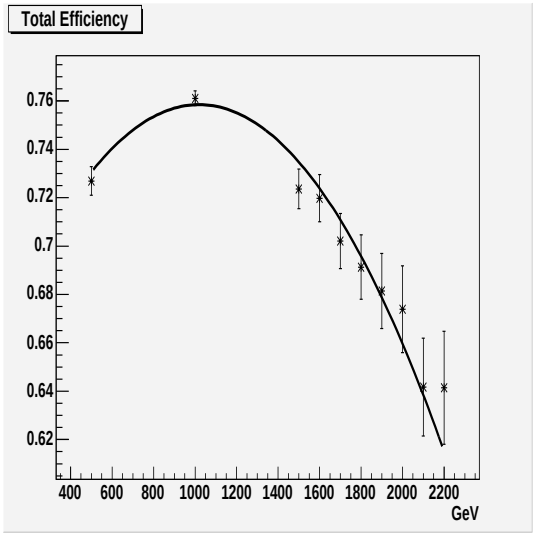

Figure 3.65: Total Efficiency obtained by fitting. No radiation. MRST(h-g) used as PDF. No trigger cuts applied.

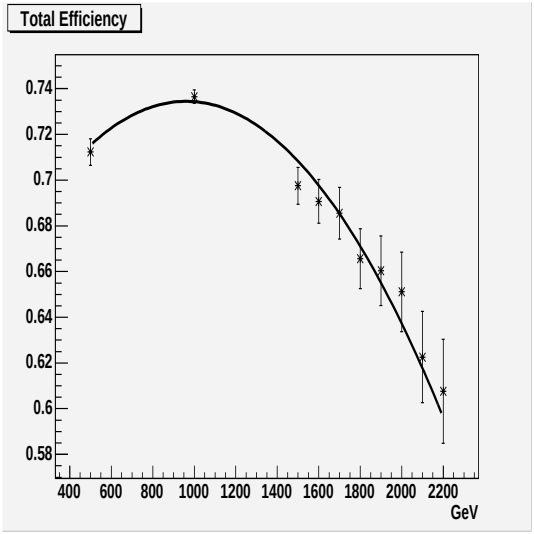

Figure 3.66: Total Efficiency obtained by fitting. Only ISR switched on. MRST(h-g) used as PDF. No trigger cuts applied.

exceptions occur at the mass points of 2200 GeV in tables 3.21 and table A.5 (only FSR) in the appendix, with an error in the efficiency of 7.3 and 8.5%, respectively. Both errors are explained by the low statistics at large invariant mass, even though the mass points are produced with 100 times more statistics! The poor description does not affect the observability of the signal, not even if we look at the changes in the significance. The poor description of the signal does not affect the discovery limit at all. The reason for this is that the FSR tails are small even if the emission probability of FSR varies as the inverse square of the particle mass i.e. the cross-section for emission is proportional to $r_e^2 = (\frac{e^2}{mc^2})^2$ [7]. The tails, outside the mass windows, caused by the FSR are solely responsible for the loss of efficiency when the resonances are fitted to gaussians. For the case of FSR only and no radiation see appendix A.

In tables 3.19 and 3.20 the efficiencies drop drastically compared to tables 3.6 and 3.7. And because of this the minimal cross-section needed to make a discovery is increasing at every mass point. This in turn affects the discovery limit. The discovery mass limits are extracted from figures 3.73-3.78.

As in section 3.6.4 the mass discovery limit is given at the point where the minimum production cross-section meets the cross-section predicted by the Randall-Sundrum model. In figures 3.77 and 3.78 the discovery mass limit is reduced compared to the limits obtained with only ISR in section 3.6.4. The limit is now about 1950 GeV for the MRST(h-g) and about 1800 GeV for CTEQ5L. Discovery mass limits obtained with no radiation are more or less the same as in the case with only ISR switched on. In other words, switching ISR on or off does not affect the discovery mass limit of the graviton. On the other hand the mass limits obtained with only FSR are identical to the ones obtained with both ISR and FSR. All the limits are given in table 3.23. The discovery mass limits for only ISR are taken from section 3.6.4.

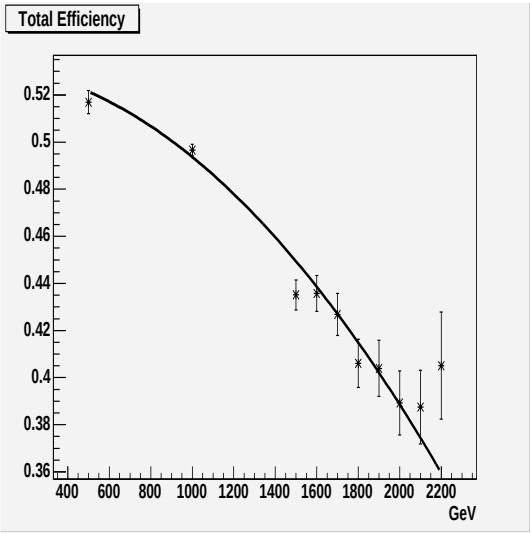

Figure 3.67: Total Efficiency obtained by fitting. Only FSR switched on. MRST(h-g) used as PDF. No trigger cuts applied.

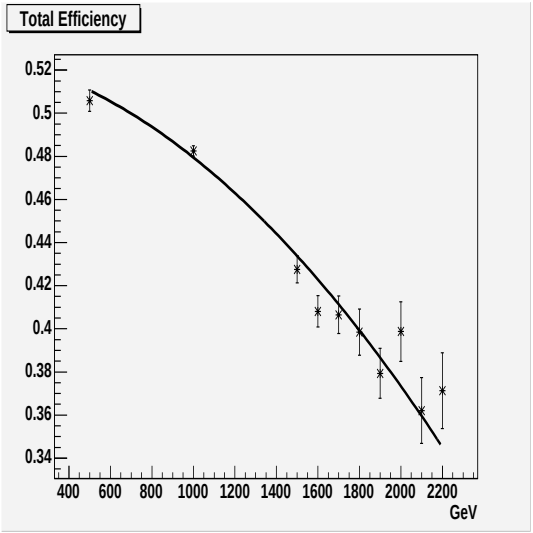

Figure 3.68: Total Efficiency obtained by fitting. Both ISR and FSR switched on. MRST(h-g) used as PDF. No trigger cuts applied.

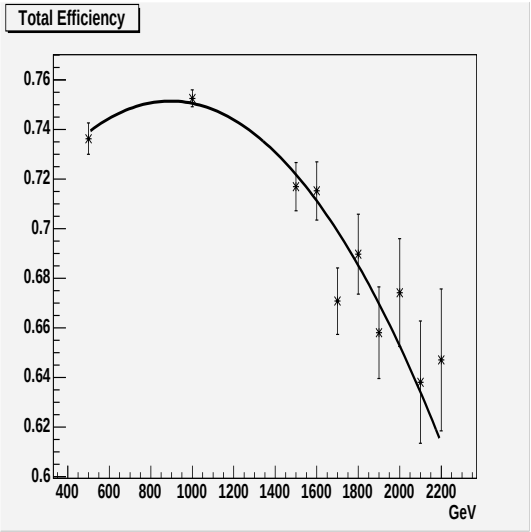

Figure 3.69: Total Efficiency obtained by fitting. No radiation. CTEQ5L used as PDF. No trigger cuts applied.

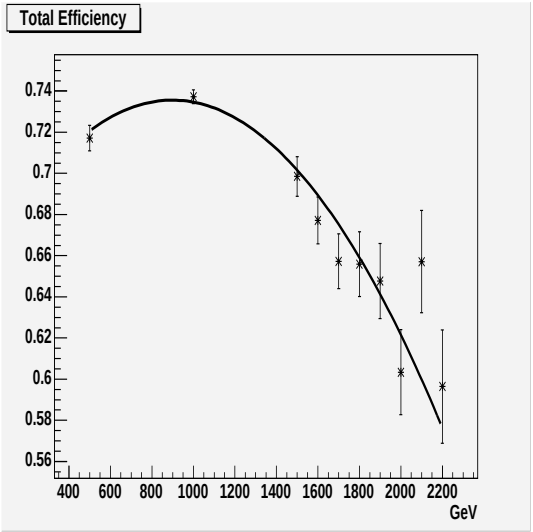

Figure 3.70: Total Efficiency obtained by fitting. Only ISR switched on. CTEQ5L used as PDF. No trigger cuts applied.

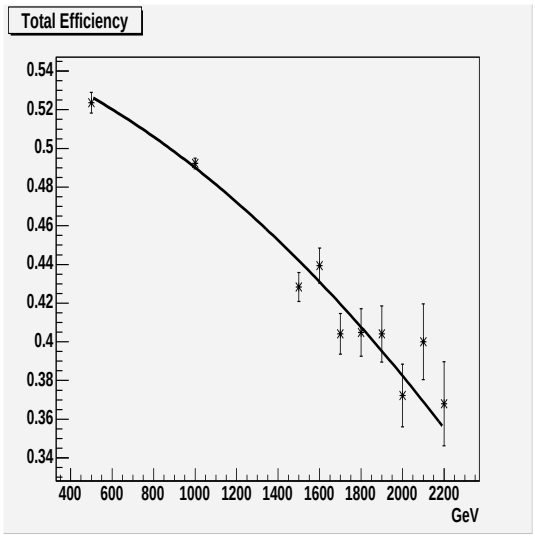

Figure 3.71: Total Efficiency obtained by fitting. Only FSR switched on. CTEQ5L used as PDF. No trigger cuts applied.

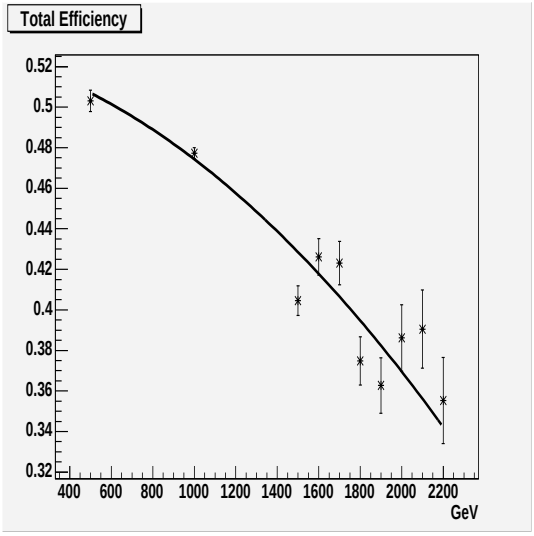

Figure 3.72: Total Efficiency obtained by fitting. Both ISR and FSR switched on. CTEQ5L used as PDF. No trigger cuts applied.

μ **(GeV)**	$MW_{mrst(h-g)}(GeV)$	N_S	N_B	N_S^{min}	$\epsilon_{mrst(h-g)}$	$(\sigma B)^{min}(fb)$
499	$\pm$12.04	10692	794.8	141.0	0.5058	2.789
998.8	$\pm$19.51	416.6	54.0	36.7	0.4825	0.761
1500	$\pm$25.49	45.8	8.4	14.5	0.4276	0.339
1599	$\pm$26.25	30.9	6.0	12.3	0.4081	0.301
1700	$\pm$27.30	22.0	4.2	10.3	0.4065	0.253
1800	$\pm$28.51	15.5	3.1	8.8	0.3984	0.251
1901	$\pm$28.84	10.8	2.2	10.0	0.3793	0.264
2000	$\pm$34.02	8.4	1.8	10.0	0.3987	0.251
2101	$\pm$29.72	5.7	1.1	10.0	0.3621	0.276
2201	$\pm$36.09	4.4	0.8	10.0	0.3713	0.269

Table 3.19: The mass windows (MW) for different masses, given by $\mu \pm 3\ \sigma_m$, where the background and signal events are obtained by integration and fitting, respectively. The number of signal events beneath a gaussian, N_S. The number of background events inside the mass window, N_B. The minimal signal events needed to detect the resonance, N_S^{min}. The total efficiency inside a mass window, $\epsilon_{mrst(h-g)}$, and the minimum cross-section needed to detect the graviton, $(\sigma B)^{min}$.

μ (GeV)	$MW_{cteq5l}(GeV)$	N_S	N_B	N_S^{min}	ϵ_{cteq5l}	$(\sigma B)^{min}(fb)$
499	$\pm$12.29	9347.4	842.9	145.2	0.5031	2.886
998.8	$\pm$19.62	314.8	53.4	36.5	0.4773	0.765
1500	$\pm$24.88	30.7	8.1	14.2	0.4046	0.351
1600	$\pm$26.90	22.4	5.9	12.2	0.4261	0.286
1700	$\pm$28.61	15.7	4.3	10.4	0.4230	0.246
1801	$\pm$28.90	10.0	3.1	8.8	0.3748	0.267
1900	$\pm$28.76	7.0	2.1	10.0	0.3627	0.276
2000	$\pm$30.36	5.5	1.8	10.0	0.3862	0.259
2101	$\pm$36.24	4.1	1.4	10.0	0.3905	0.256
2201	$\pm$35.01	2.8	0.9	10.0	0.3553	0.282

Table 3.20: The mass windows (MW) for different masses, given by $\mu \pm 3\ \sigma_m$, where the background and signal events are obtained by integration and fitting, respectively. The number of signal events beneath a gaussian, N_S. The number of background events inside the mass window, N_B. The minimal signal events needed to detect the resonance, N_S^{min}. The total efficiency inside a mass window, ϵ_{cteq5l}, and the minimum cross-section needed to detect the graviton, $(\sigma B)^{min}$.

mG (GeV)	S	ΔN	ΔS	$\Delta\epsilon$
500	379.3	$\pm$186.3	$\pm$6.61	1.7%
1000	56.7	$\pm$1.9	$\pm$0.26	0.5%
1500	15.8	$\pm$1.0	$\pm$0.35	2.1%
1600	12.6	$\pm$0.7	$\pm$0.29	2.2%
1700	10.7	$\pm$0.2	$\pm$0.10	0.9%
1800	8.8	$\pm$0.1	$\pm$0.06	0.6%
1900	7.3	$\pm$0.2	$\pm$0.14	1.8%
2000	6.3	$\pm$0.3	$\pm$0.22	3.7%
2100	5.4	$\pm$0.1	$\pm$0.10	1.7%
2200	4.4	$\pm$0.3	$\pm$0.30	7.3%

Table 3.21: The Significance, the error between the number of signal events obtained by fitting and counting, $\Delta N = |N_{count} - N_{fit}|$ and the resulting errors in significance $\Delta S = \frac{\Delta N}{\sqrt{N_B}}$ and in the total efficiency due to fitting $\Delta\epsilon = \frac{\Delta N}{N_{count}}$. MRST(h-g) used as PDF.

mG (GeV)	S	ΔN	ΔS	$\Delta\epsilon$
500	322.0	$\pm$243.0	$\pm$8.37	2.5%
1000	43.1	$\pm$2.7	$\pm$0.37	0.9%
1500	10.8	$\pm$0.8	$\pm$0.28	2.5%
1600	9.2	$\pm$0.0	$\pm$0.00	0.0%
1700	7.8	$\pm$0.0	$\pm$0.00	0.0%
1800	5.7	$\pm$0.5	$\pm$0.28	4.7%
1900	4.8	$\pm$0.1	$\pm$0.07	1.4%
2000	4.1	$\pm$0.2	$\pm$0.15	3.8%
2100	3.5	$\pm$0.1	$\pm$0.09	2.5%
2200	2.8	$\pm$0.1	$\pm$0.10	3.7%

Table 3.22: The Significance, the error between the number of signal events obtained by fitting and counting, $\Delta N = |N_{count} - N_{fit}|$ and the resulting errors in significance $\Delta S = \frac{\Delta N}{N_B}$ and in the total efficiency due to fitting $\Delta\epsilon = \frac{\Delta N}{N_{count}}$. CTEQ5L used as PDF.

Radiation	Limit$_{mrst(h-g)}$(GeV)	Limit$_{cteq5l}$(GeV)
No radiation	2125	2000
Only ISR	2100	2000
Only FSR	1950	1800
ISR and FSR	1950	1800

Table 3.23: The discovery mass limits for different radiation scenarios described in the text. MRST(h-g) and CTEQ5L used.

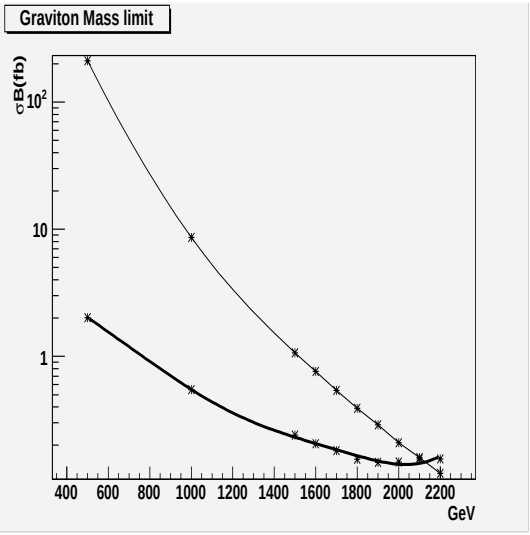

Figure 3.73: Cross-sections for $G \to e^+e^-$ in the R-S model (light curve) and the smallest detectable cross-setion (black). Both ISR and FSR switched off. MRST(h-g) used.

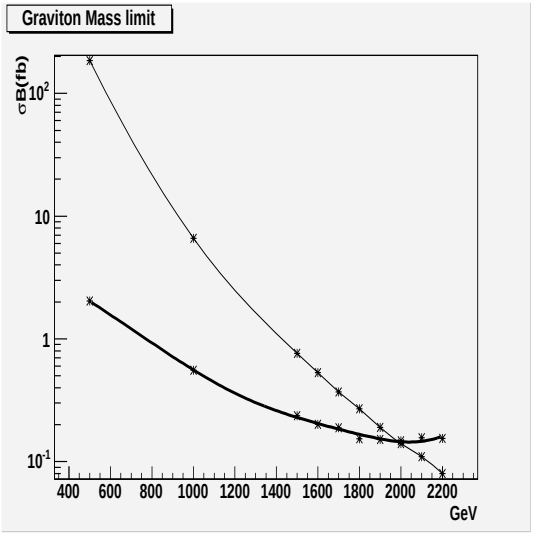

Figure 3.74: Cross-sections for $G \to e^+e^-$ in the R-S model (light curve) and the smallest detectable cross-setion (black). Both ISR and FSR switched off. CTEQ5L used.

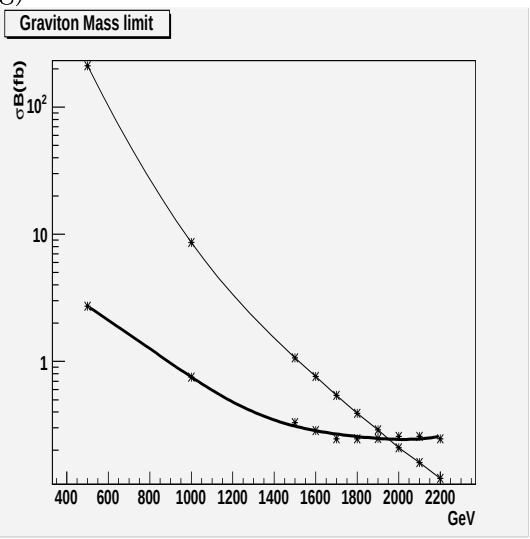

Figure 3.75: Cross-sections for $G \to e^+e^-$ in the R-S model (light curve) and the smallest detectable cross-setion (black). ISR switched off and FSR switched on. MRST(h-g) used.

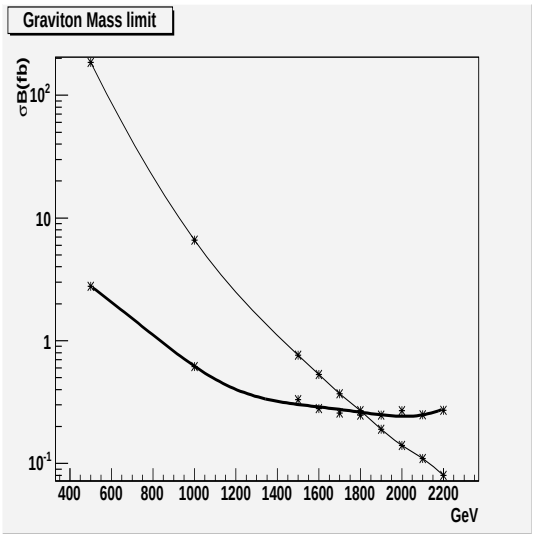

Figure 3.76: Cross-sections for $G \to e^+e^-$ in the R-S model (light curve) and the smallest detectable cross-setion (black). ISR switched off and FSR switched on. CTEQ5L used.

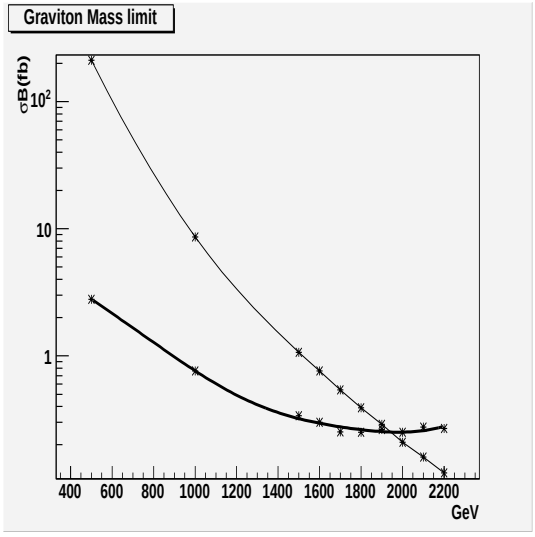

Figure 3.77: Cross-sections for $G \to e^+e^-$ in the R-S model (light curve) and the smallest detectable cross-setion (black). Both ISR and FSR switched on. MRST(h-g) used.

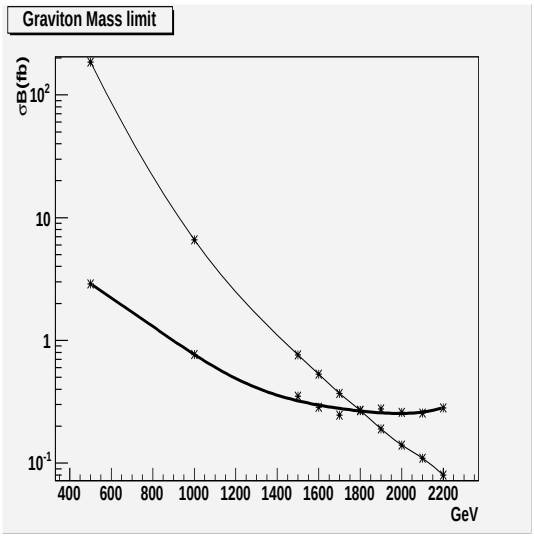

Figure 3.78: Cross-sections for $G \to e^+e^-$ in the R-S model (light curve) and the smallest detectable cross-setion (black). Both ISR and FSR switched on. CTEQ5L used.

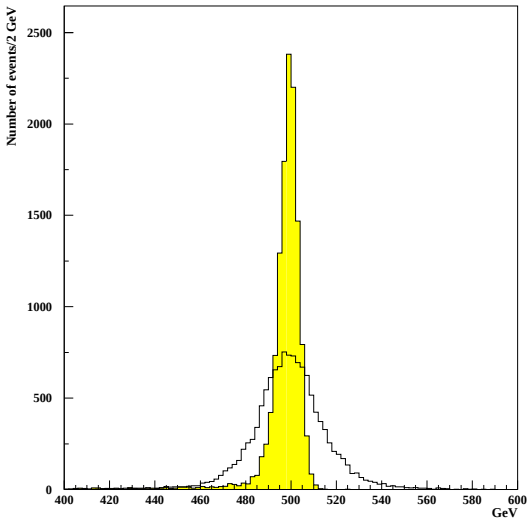

Figure 3.79: Graviton Resonances from the e^+e^- (the shaded area) and $\mu^+\mu^-$ decay modes. CTEQ5L used as PDF. No trigger cuts applied.

3.8 $G^* \rightarrow \mu^+\mu^-$

The muon decay mode of gravitons is important because it may be useful to check lepton universality, i.e. the assumption that lepton interactions are indentical once mass differences are taken into account. The branching ratios of the electron decay mode and the muon decay mode are similar. But the muon resolution is worse. In this section the signal in the muon decay mode is described and the effects of radiation discussed. Discovery mass limits are obtained using CTEQ5L which yields the most conservative signal cross-section. The limits are not as high as in the dielectron mode, because of the poor muon momentum resolution.

3.8.1 Signal Description

The muon tracks are measured in a different way than the electrons. While ATLAS measures the energy of electrons in the electromagnetic calorimeter it uses momentum measurement in the Muon Spectrometer. This implies a very different experimental resolution. Energy measurement gives relative better resolution with increasing energy. This is not the case for momentum measurement where the relative uncertainty increases with higher energies. The experimental resolution when measuring momentum is given by:

$$\frac{\Delta p}{p} \sim p \tag{3.21}$$

At high muon momentum the momentum resolution of the Muon Spectrometer decreases. Low momentum tracks have greater curvature making the momentum mea-

Radiation	500 GeV	1000 GeV	1500 GeV	2000 GeV
No Radiation	0.9020	0.9289	0.9350	0.9410
Only ISR	0.8267	0.8499	0.8454	0.8427
Only FSR	0.7347	0.7124	0.6852	0.6868
ISR and FSR	0.6803	0.6495	0.6245	0.6243

Table 3.24: The acceptance for the total number of reconstructed signal events for different scenarios and invariant masses. CTEQ5L used as PDF.

surement more accurate. The opposite is true for high momentum tracks. This gives a much worse experimental resolution for muons than electrons at high invariant masses. This is already apparent with graviton resonances at 500 GeV, see figure 3.79, where the e^+e^- and $\mu^+\mu^-$ invariant masses are compared. The experimental mass resolutions are found to be about 4.1 and 14.8 GeV for the e^+e^- and $\mu^+\mu^-$ invariant masses, respectively. Another important aspect of muons is that they are 200 times heavier than the electrons. This ensures that the losses due to Final State Radiation are smaller than in the case of the electrons, see tables 3.18 and 3.24. The total efficiency is obtained by multiplying the acceptance with a factor of 0.81, which corresponds to the lepton identification efficiency. 18580 events are generated with a graviton of 500 GeV at a luminosity of 100 fb^{-1}, and 65950, 7588 and 1424 events are generated for the masses 1000, 1500 and 2000 GeV, respectively, corresponding to an integrated luminosity of 10000 fb^{-1}. In combination with the worse resolution the low energy tail is almost invisible. For this reason we obtain a symmetric signal rather than an asymmetric like in the case of the electrons. In figure 3.80 a 500 GeV graviton is produced in different radiation scenarios. All the gravitons have a symmetric shape.

Even though the signal is symmetric the bad resolution makes it difficult to fit it well with a gaussian. Figure 3.82 shows graviton resonances of 500, 1000, 1400 (11100 events generated for an integrated luminosity of 10000 fb^{-1}) and 1500 GeV fitted to a gaussian. ISR and FSR are switched on. The single gaussian fails to take into account the top of the signal, as well as the sides at the bottom of the signal. The χ^2 is poor and varies between 2.1 and 7.0. The bad resolution causes a broadening in the signal which is difficult to take into account by one gaussian. A second gaussian is therefore added to give a better fit, see figure 3.83. The two gaussians fit the signals much better, and this is reflected in the χ^2 which now varies between 1.1 and 1.7. Almost all of the events[3] are taken into account by the two gaussians. For 500 GeV and 1500 the acceptance obtained by the fits is 66 and 60%, respectively. The corresponding acceptance for the total number of events reconstructed is 68 and 63 %, respectively. With a single gaussian fit the same acceptances are 64 and 57 %, respectively.

[3]These are given by the sum of the parameters P1 and P4 in the figure 3.83

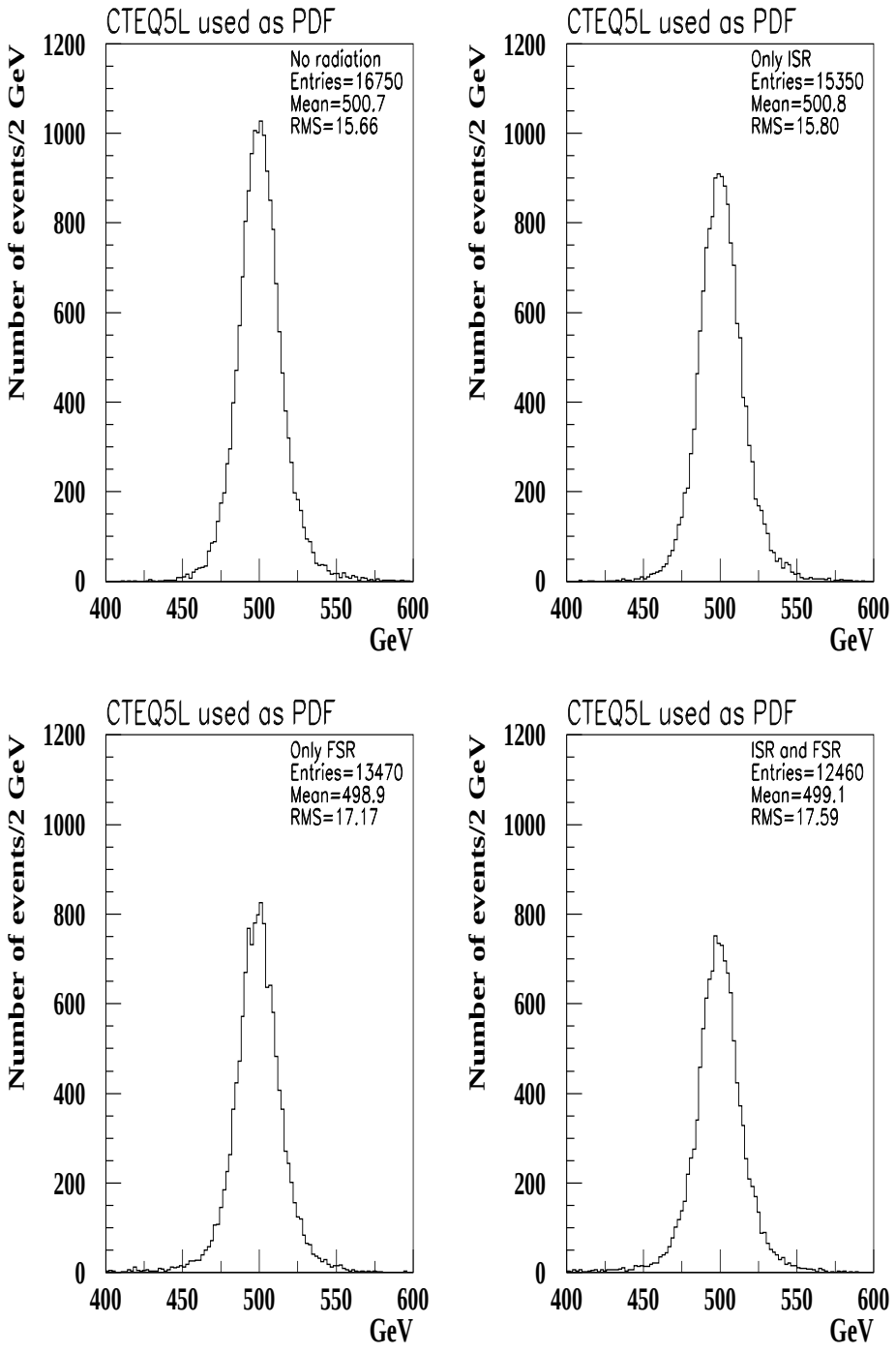

Figure 3.80: Invariant mass of a 500 GeV graviton resonance produced in different radiation scenarios. Integrated luminosity set to 100 fb^{-1}. No trigger cuts applied.

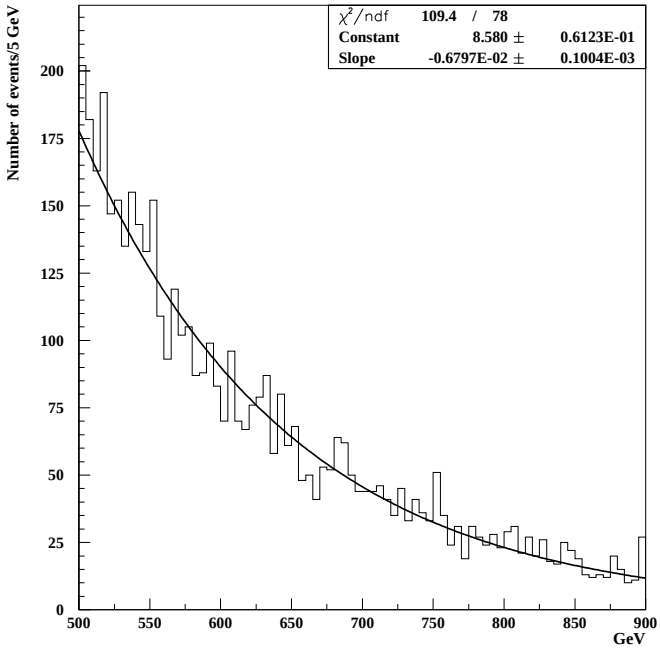

Figure 3.81: The Drell-Yan background, with a 350 GeV cut on the invariant mass, produced with ISR and FSR. Integrated luminosity set to 100 fb^{-1}. No trigger cuts applied.

3.8.2 Background Description

This channel, like in the case with the electrons, has Drell-Yan background which is well described by an exponential function. This is illustrated in figure 3.81. 36170 Drell-Yan events are generated for CTEQ5L. This corresponds to a cut on the invariant mass of 350 GeV, and an integrated luminosity of 100 fb^{-1}.

Table 3.25 shows the overall efficiency for the Drell-Yan background. The efficiencies are similar to the efficiencies for the electron decay mode in the tables 3.14 and 3.15.

3.8.3 Results

The analysis of the muon channel is similar to the electrons channel but has some important differences. Although trigger cuts are not used in this study ATLAS requires the muons to have $P_t > 10$ GeV [10] which is half of what is required for electrons. The interaction probabillity is proportional to $\frac{1}{M^2}$. Since the muon mass is 200 times bigger than the electron mass, this allows the muons to escape the EM calorimeter. Muons are minimum ionising particles or MIPs. The muons also pass through the Hadronic calorimeter because leptons do not interact strongly. This makes the muons easy to tag and makes it possible to use lower P_t cuts. Both muons must pass a pseudorapidity, $|\eta|<2.4$ cut to be detectable. Graviton masses between 500 and 1500 GeV are generated

Radiation	$\epsilon_{accetance}$	$\epsilon_{identification}$	$\epsilon_{overall}$
No Radiation	0.6613	0.81	0.5357
Only ISR	0.6558	0.81	0.5312
Only FSR	0.5518	0.81	0.4470
ISR and FSR	0.5419	0.81	0.4389

Table 3.25: Different efficiencies for different scenarios for the Drell-Yan background with a cut of 350 GeV on the invariant mass. $\epsilon_{acceptance}$ is the acceptance, $\epsilon_{identification}$ is the lepton identification efficiency and $\epsilon_{overall}$ is the overall efficiency. CTEQ5L used as PDF.

and no trigger cuts are applied. Both ISR and FSR are switched on. The 500 GeV mass point (with corresponding background) is produced at an integrated luminosity of 100 fb^{-1}, and the rest of the mass points (with corresponding backgrounds) are produced at an integrated luminosity of 10000 fb^{-1}.

The signal alone is poorly described by one gaussian, as shown in figure 3.82. By including the background, the signal 'becomes' narrower. The broadening disappears into the background and only a little bump is left. The signal is now well described with a single gaussian, see figure 3.84. The χ^2 varies between 1.1 and 1.7. But the signal is more and more lost in the background with larger mass. At 500 GeV the acceptance is 62% which is 6% less than the acceptance for the total number of reconstructed signal events. The corresponding numbers for 1500 GeV is 42 and 21%, respectively.

In order to make comparisons mass discovery limits are derived for both single and double gaussians. The resoltution of the two combined gaussians is given by [37]:

$$\sigma_{com} = \sqrt{\frac{N_1}{N_1+N_2}\sigma_1^2 + \frac{N_2}{N_1+N_2}\sigma_2^2} \tag{3.22}$$

where N_1, N_2, σ_1 and σ_2 are the number of events and the mass resolution, of the first and second gaussian, respectively. $\frac{N_1}{N_1+N_2}$ and $\frac{N_2}{N_1+N_2}$ are the weights and are from now on denoted as w_1 and w_2. Equation 3.22 yields a larger experimental mass resolution, so the mass window becomes larger than in the case with a single gaussian. Thus more signal events and better signal efficiency is expected. But the total efficiencies obtained by single and double gaussians are more or less the same except in the points 1200 and 1500 GeV, see tables 3.27 and 3.29. This is also true for the minimum production cross sections, $(\sigma B)^{min}$. The χ^2 or the godness of the fit is, not suprisingly, comparable, see table 3.26 and figures 3.84 and 3.85. The mass discovery limit obtained in both these cases are about 1325 GeV, see figure 3.86. The difference with the limit in reference [1] is thus 375 GeV. For the future: It is sufficient to use a single gaussian in this analysis, which makes life a little bit easier.

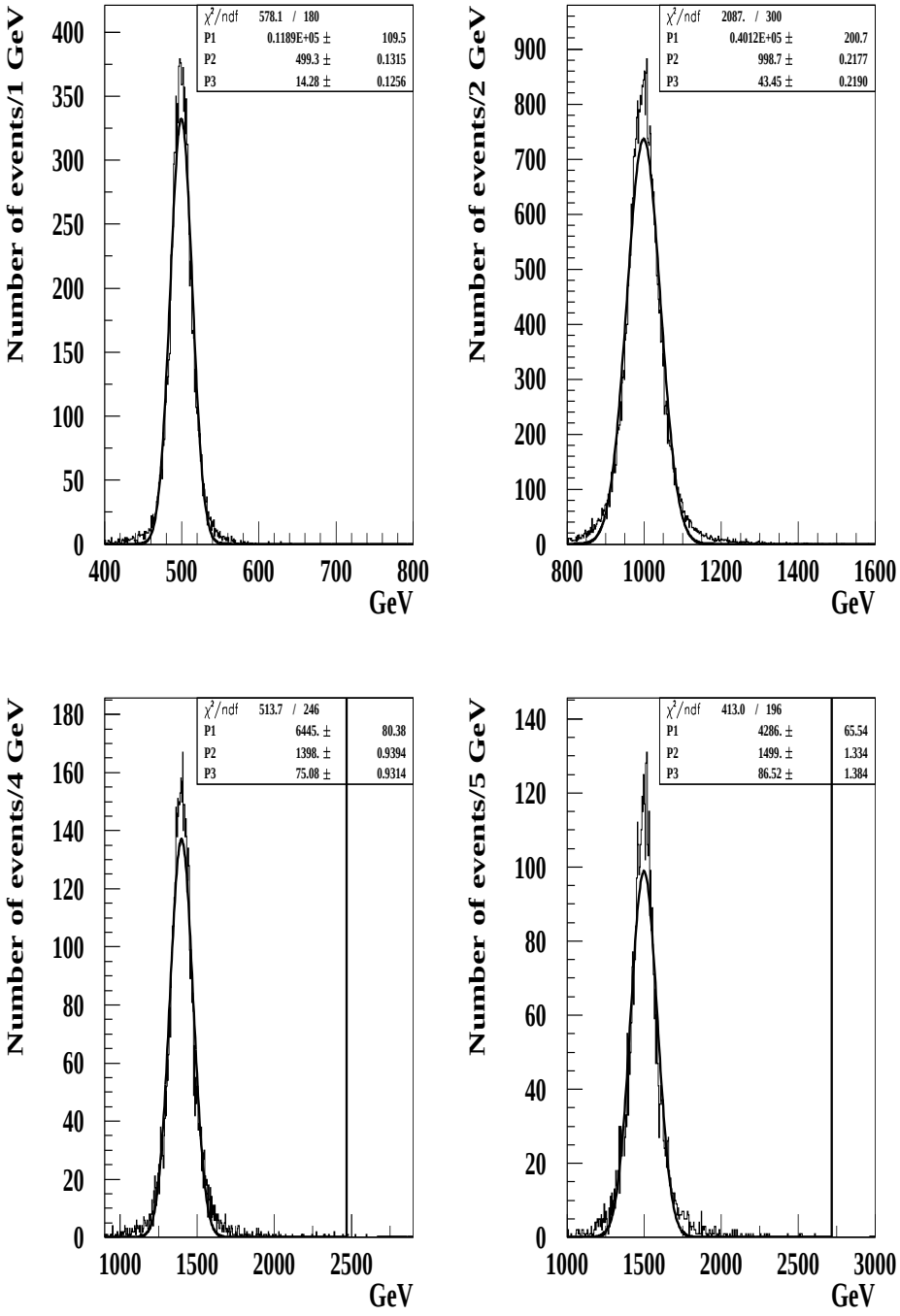

Figure 3.82: Graviton resonances with different mass fitted with a gaussian. ISR and FSR switched on. The 500 GeV point (with background) corresponds to an integrated luminosity of 100 fb^{-1}, while the other points (with backgrounds) are artificially produced with an integrated luminosity of 10000 fb^{-1}. CTEQ5L used as PDF. No trigger cuts applied.

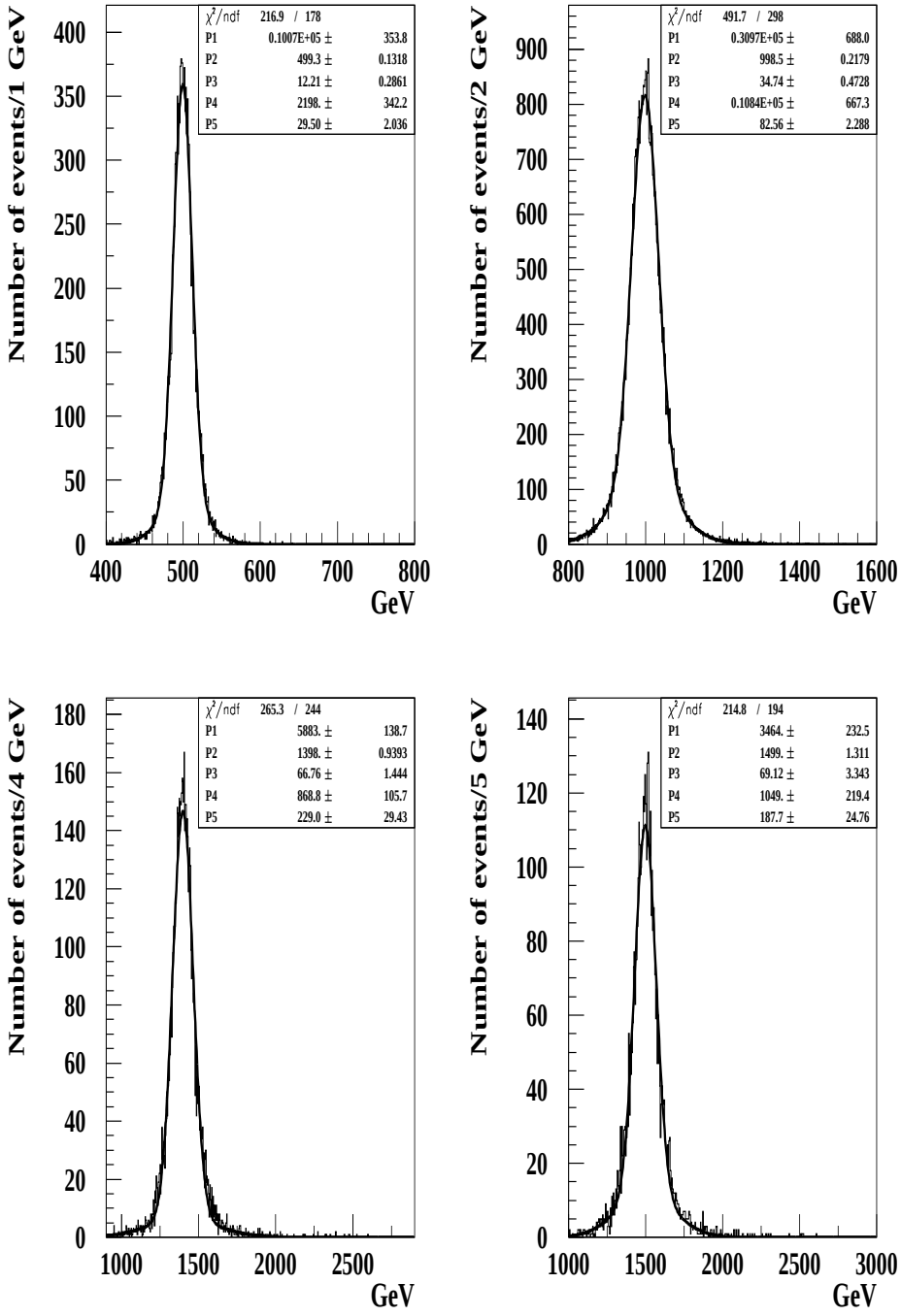

Figure 3.83: Graviton resonances with different mass fitted with two gaussians. ISR and FSR switched on. The 500 GeV point (with background) corresponds to an integrated luminosity of 100 fb^{-1}, while the other points (with backgrounds) are artificially produced with an integrated luminosity of 10000 fb^{-1}. CTEQ5L used as PDF. No trigger cuts applied.

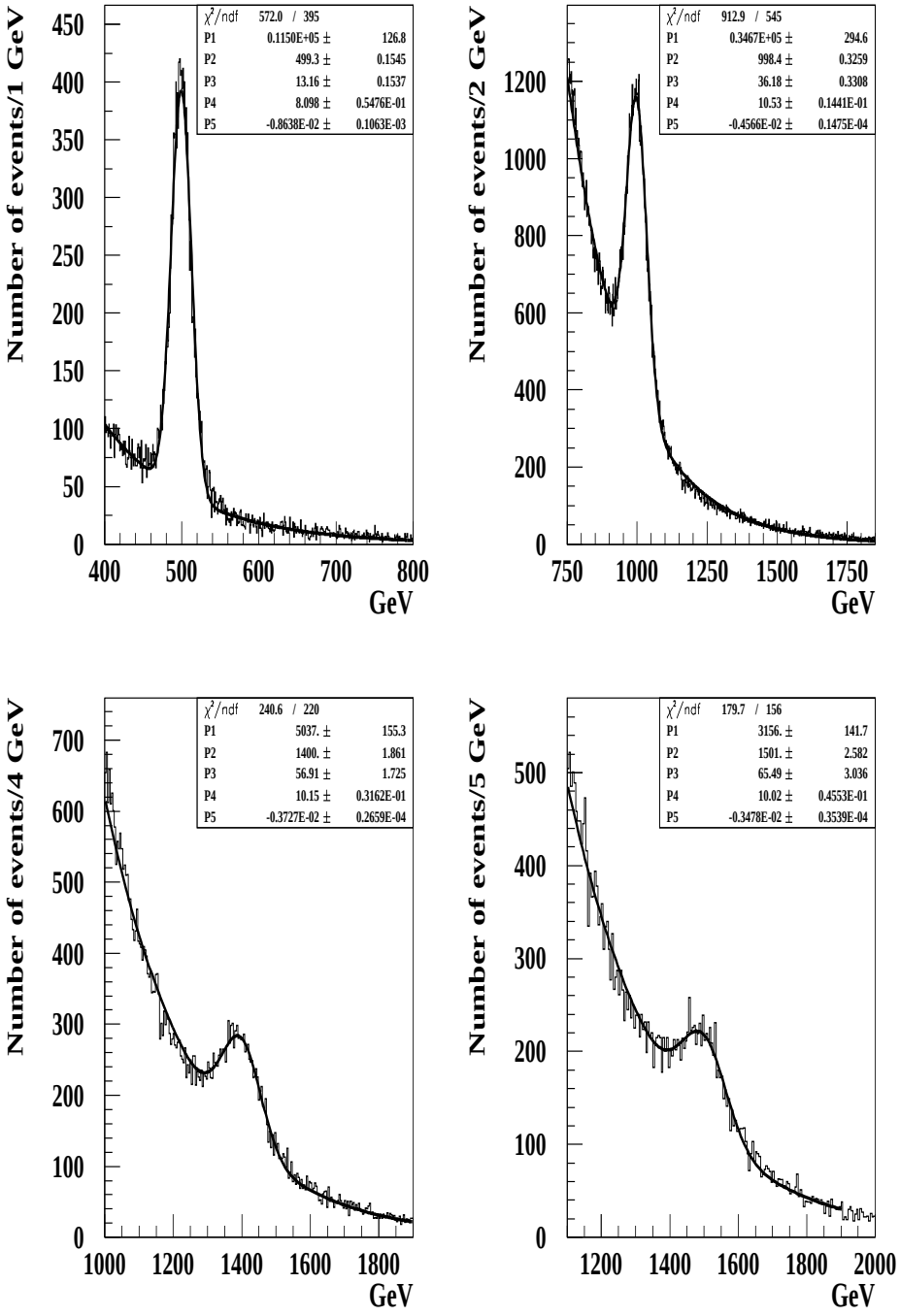

Figure 3.84: Graviton resonances with different mass fitted with a gaussian above the Drell-Yan background. ISR and FSR switched on. The 500 GeV point (with background) corresponds to an integrated luminosity of 100 fb^{-1}, while the other points (with backgrounds) are artificially produced with an integrated luminosity of 10000 fb^{-1}. CTEQ5L used as PDF. No trigger cuts applied.

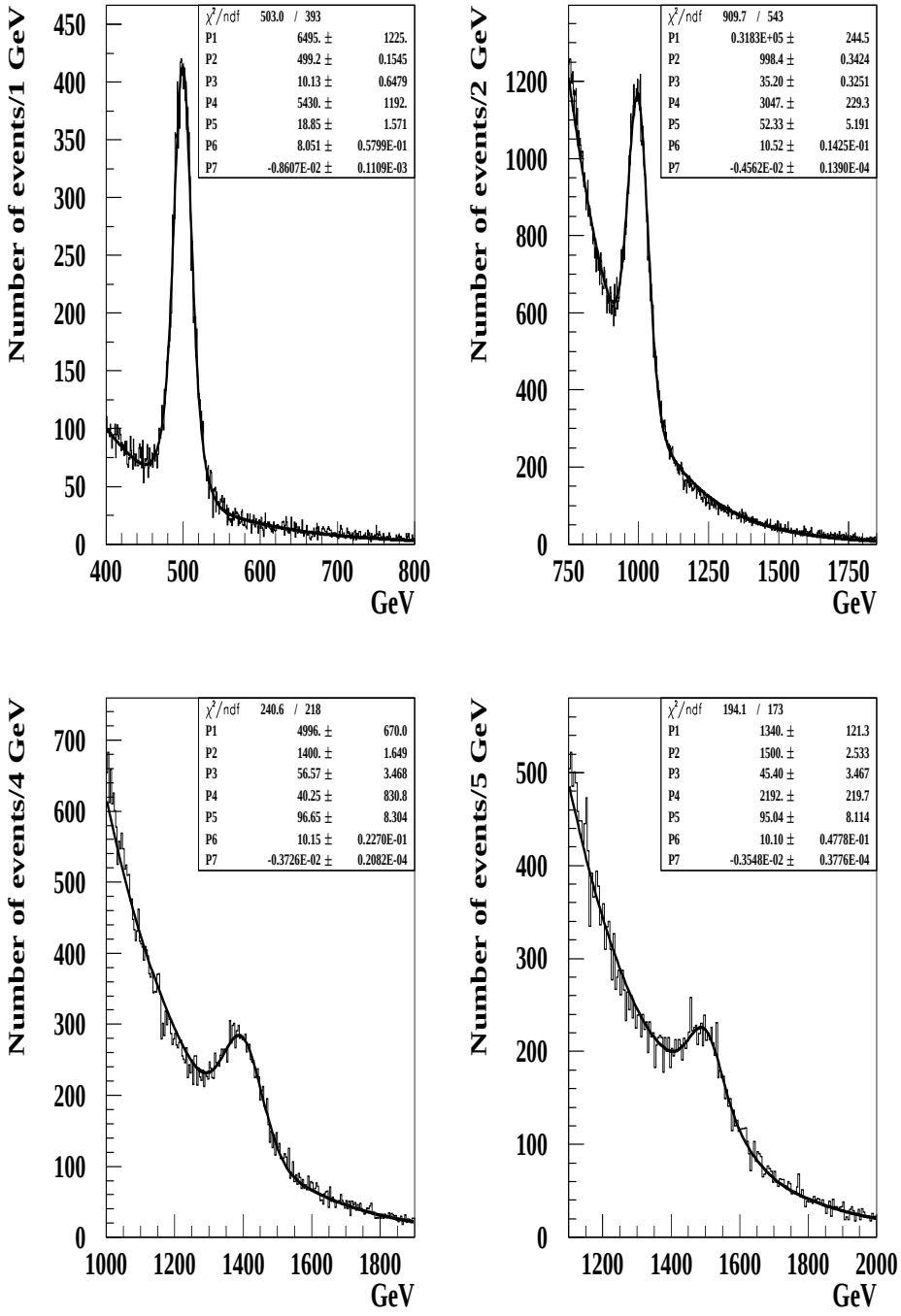

Figure 3.85: Graviton resonances with different mass fitted with two gaussians above the Drell-Yan background. ISR and FSR switched on. The 500 GeV point (with background) corresponds to an integrated luminosity of 100 fb^{-1}, while the other points (with backgrounds) are artificially produced with an integrated luminosity of 10000 fb^{-1}. CTEQ5L used as PDF. No trigger cuts applied.

mG (GeV)	χ^2_g	χ^2_{2g}
500	1.45	1.28
1000	1.68	1.68
1100	1.66	1.65
1200	1.12	1.08
1300	1.07	1.07
1400	1.09	1.10
1500	1.15	1.12

Table 3.26: The goodness of the fits with one gaussian, χ^2_g and the goodness of the fits with two gaussians χ^2_{2g}

μ **(GeV)**	$MW_{cteq5l}(GeV)$	N_S	N_B	N_S^{min}	ϵ_{cteq5l}	$(\sigma B)^{min}(fb)$
499.3	$\pm$39.48	9315	2869.6	267.8	0.5013	5.342
998.4	$\pm$108.5	280.8	358.4	94.7	0.4258	2.224
1099	$\pm$121.4	156.9	255.1	79.9	0.3900	2.049
1197	$\pm$144.2	102.2	190.4	69.0	0.4014	1.719
1301	$\pm$162.4	63.4	143.2	59.8	0.3801	1.573
1400	$\pm$170.7	40.8	103.1	50.8	0.3676	1.382
1501	$\pm$196.5	25.7	83.5	45.7	0.3387	1.349

Table 3.27: The mass windows (MW) for different masses in the muon decay mode, given by $\mu \pm 3\,\sigma_m$, where the background and signal events are obtained by integration and fitting, respectively. The number of signal events beneath the gaussian, N_S. The number of background events inside the masswindow, N_B. The minimal signal events needed to detect the resonance, N_S^{min}. The total efficiency inside a mass window, ϵ_{cteq5l}, and the minimum cross-section needed to detect the graviton, $(\sigma B)^{min}$.

m (GeV)	N_1	N_2	σ_1	σ_2	w_1	w_2	σ_{com}
500	5261	4398.3	10.13	18.85	0.5447	0.4553	14.75
1000	257.8	24.7	35.20	52.33	0.9126	0.0874	37.02
1100	70.9	88.5	33.09	48.59	0.4448	0.5552	42.40
1200	58.7	52.7	37.90	74.27	0.5269	0.4731	58.02
1300	56.8	6.6	53.84	57.15	0.8959	0.1041	54.19
1400	40.5	0.3	56.57	96.65	0.9926	0.0074	56.97
1500	10.9	17.8	45.40	95.04	0.3798	0.6202	79.91

Table 3.28: The number of events under the first and second gaussian respectively, N_1 and N_2. The resolution of the first and secound gaussian respectively, σ_1 and σ_2. The weights w_1 and w_2 and the resoltion of the combined gaussian σ_{com}.

μ (GeV)	$MW_{cteq5l}(GeV)$	N_S	N_B	N_S^{min}	ϵ_{cteq5l}	$(\sigma B)^{min}(fb)$
499	$\pm$44.25	9659.3	3135.9	280.0	0.5199	5.386
998.4	$\pm$111.1	282.5	367.0	95.8	0.4284	2.236
1099	$\pm$127.2	159.4	267.7	81.8	0.3962	2.065
1196	$\pm$142.4	111.4	229.8	75.8	0.4375	1.733
1301	$\pm$174.1	63.4	143.4	59.9	0.3801	1.576
1400	$\pm$162.6	40.8	103.3	50.8	0.3676	1.382
1500	$\pm$239.7	10.9	103.4	50.8	0.3782	1.343

Table 3.29: The background and signal events are obtained by integration and fitting with two gaussians, respectively. The mass windows (MW) for different masses in the muon decay mode, given by $\mu \pm 3\ \sigma_{com}$ where σ_{com} is the combined resolution of the first and second gaussian. The number of signal events beneath the two gaussians, N_S. The number of background events inside the mass window, N_B. The minimal signal events needed to detect the resonance, N_S^{min}. The acceptance inside a mass window, ϵ_{cteq5l}, and the minimum cross-section needed to detect the graviton, $(\sigma B)^{min}$.

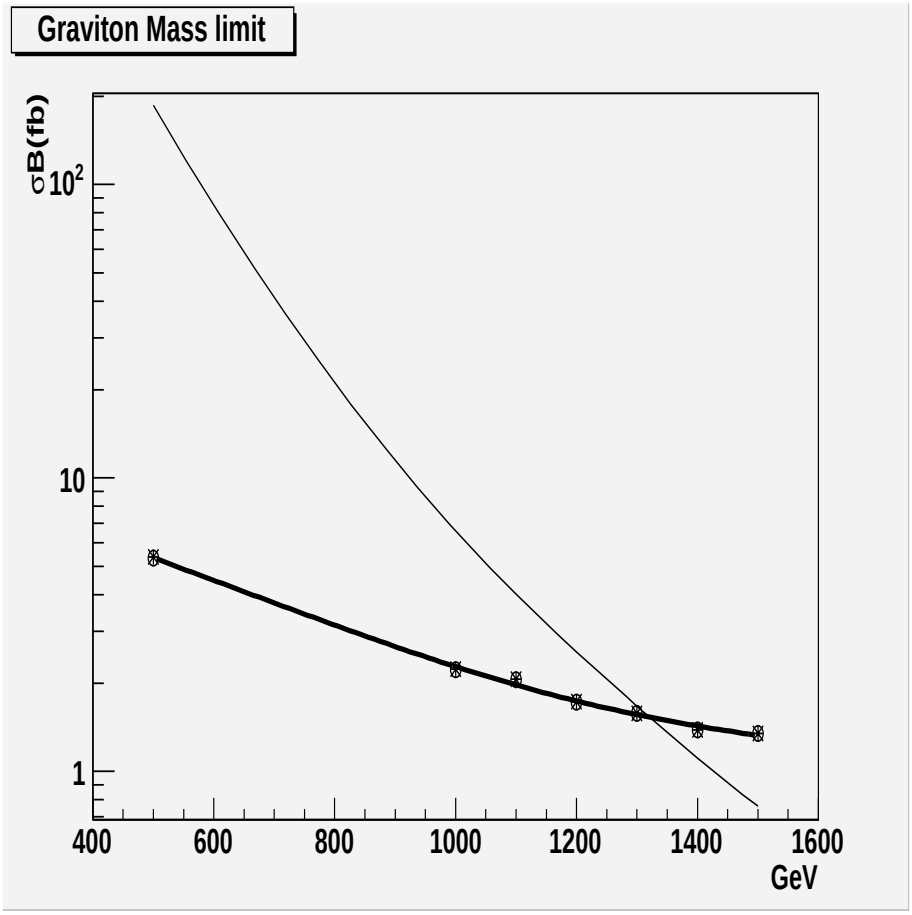

Figure 3.86: Cross-sections for $G \rightarrow \mu^+ + \mu^-$ in the R-S model (light line) and the smallest detectable cross-section. The results obtained with one gaussian (stars) and two gaussians (circles) are used.

Radiation	500 GeV	1000 GeV	1500 GeV	2000 GeV
No Radiation	0.8609	0.9127	0.8927	0.8367
Only ISR	0.8545	0.8946	0.8691	0.8280
Only FSR	0.8646	0.9119	0.8979	0.8270
ISR and FSR	0.8604	0.8961	0.8711	0.8280

Table 3.30: The acceptance for the total number of reconstructed signal events for different scenarios and invariant masses. CTEQ5L used as PDF.

3.9 $G^* \to \gamma\gamma$

The branching ratio of the photon decay mode is about 4.1 %, see table 3.1. It is twice that of the lepton pair branching ratio. The energy resolution is as good as for electrons and this makes the photon decay mode a good channel for discovery. The background, which consists of two photons in the final state, is more difficult to 'understand', however. It consists of Born and box processes, and backgrounds coming from QCD jets. A partonic event generator, DIPHOX [13], is used to determine the size of this difficult background. The discovery mass limit is subsequently achieved using PYTHIA and ALTFAST. Only CTEQ5L is used as a Parton Distribution Function for simplicity.

3.9.1 Signal Description

The photons, which are massless, do not emit FSR, which makes it possible to fit the signal peaks with single gaussians. 37310 events are generated with a graviton of 500 GeV at a luminosity of 100 fb^{-1}, and 132800, 15280 and 2878 events are generated for the masses 1000, 1500 and 2000 GeV, respectively, corresponding to an integrated luminosity of 10000 fb^{-1}. Figure 3.87 shows the $\gamma\gamma$ invariant mass for 500 GeV gravitons produced in different radiation scenarios. All the signals are symmetric. Table 3.30 shows that the acceptance in the photon decay mode is not affected by FSR. The acceptance for each mass in different scenarios is more or less constant since the photons do not radiate in the detector, and ISR, which occurs before the partons collide, has only a minor impact on the acceptance. The radiating partons do not reduce their energies sufficiently in order to affect the acceptance. The losses are of order 1-2%. The difference in acceptance between the 1 TeV and 2 TeV gravitons, when ISR and FSR is switched on, is only 7%.

3.9.2 Background Description

In Born and Box processes, see figures 3.88 and 3.89 respectively, the two photons are produced as follows:

$$\text{Born} : \text{f}\bar{\text{f}} \to \gamma\gamma \tag{3.23}$$

$$\text{Box} : \text{gg} \to \gamma\gamma \tag{3.24}$$

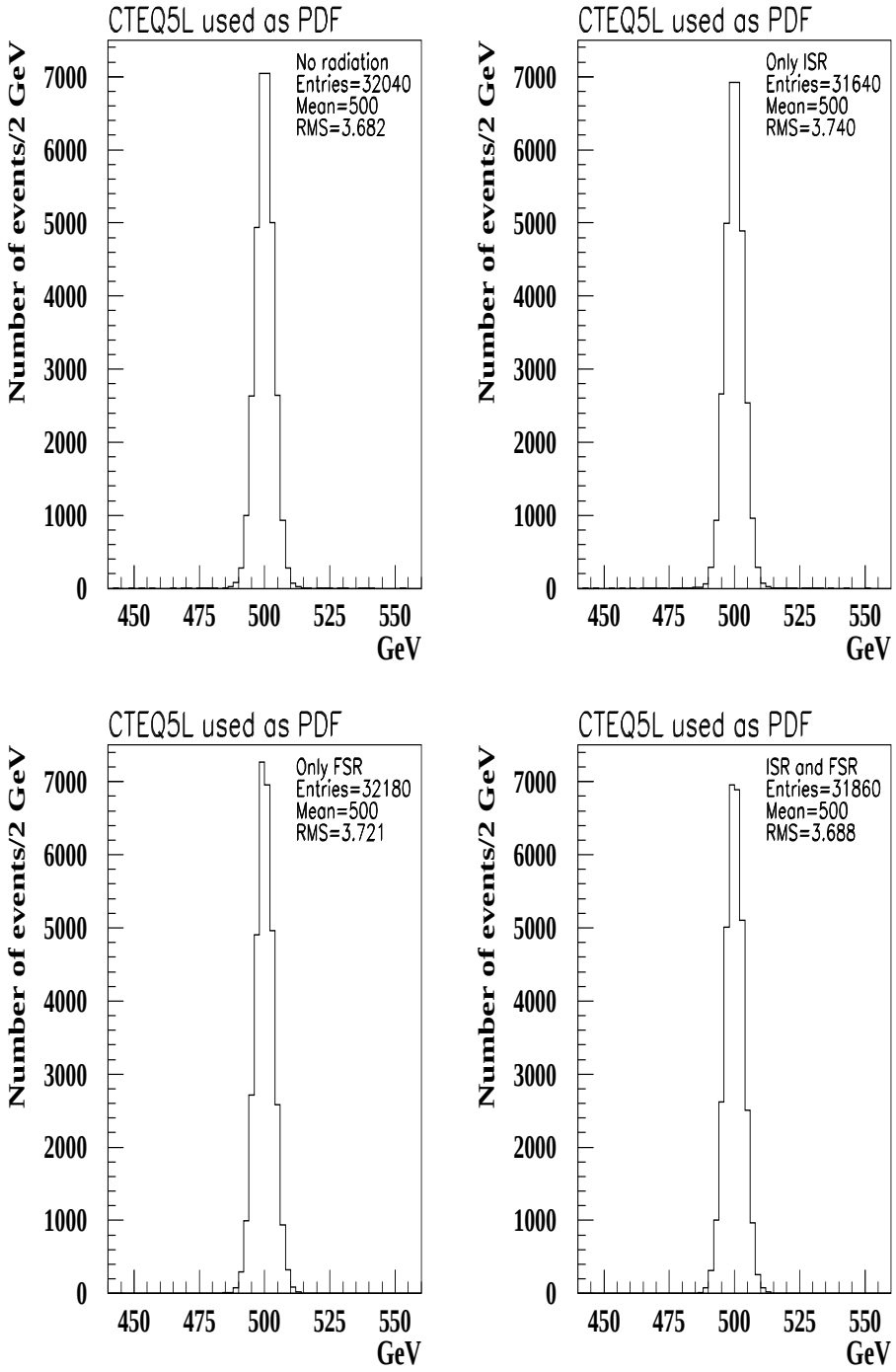

Figure 3.87: Invariant mass of a 500 GeV graviton resonance decaying into $\gamma\gamma$ and produced in different radiation scenarios. Integrated luminosity set to 100 fb^{-1}. No trigger cuts applied.

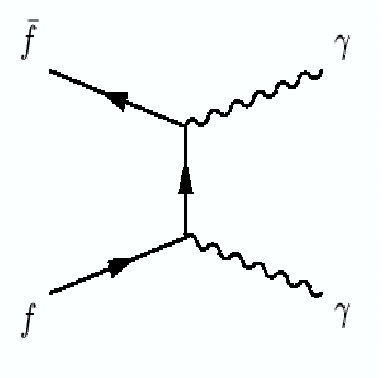

Figure 3.88: The born process. Plot taken from [12].

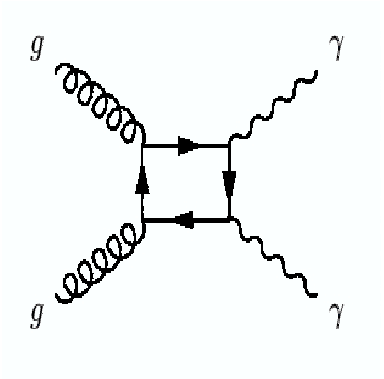

Figure 3.89: The box process. Plot taken from [12].

This background is called irreducible because the photons do not result from decay of hadrons like π^0, η or ω. The irreducible background also includes what is called 'bremsstrahlung' [11] (which is an ambiguous term) or fragmentation (which is a more appropriate term). The 'bremsstrahlung' processes consists of a photon and a fermion/gluon in the final state. But the fermion/gluon fragments giving an addional softer photon in the final state:

$$f\overline{f} \to g\gamma \rightsquigarrow g\gamma\gamma \tag{3.25}$$

$$fg \to f\gamma \rightsquigarrow f\gamma\gamma \tag{3.26}$$

$$gg \to g\gamma \rightsquigarrow g\gamma\gamma \tag{3.27}$$

These processes are not implemented in PYTHIA, which only includes processes with one photon in the final state i.e. processes without fragmentation. In order to get the second photon in the final state, Final State QED Radiation must be switched on. But PYTHIA calculates the cross-section on the hard process level only. So when the Final State QED Radiation is added the final state topology (or the Feynman diagram) is

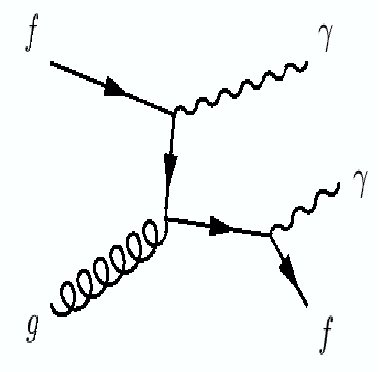

Figure 3.90: A 'bremsstrahlung' process (process 3.26) were f fragments and emits a photon in final state. Plot taken from [12].

changed but the cross-section is not. The cross-section is still that of processes with one photon in the final state only. It is still possible to obtain the cross-sections of bremsstrahlung with two photons in the final state, but this is time consuming and not very reliable Monte Carlo generation is needed.

A program called DIPHOX designed to calculate the hadro-production of two photons (or one hadron plus one photon, or two hadrons) [13] is used to calculate the cross-section of the bremsstrahlung contribution. DIPHOX is compared to PYTHIA in [14] at Next to Leading Order (NLO).

In DIPHOX, which is a 'partonic event generator', the 'bremsstrahlung' contributions contain the following partonic sub-processes:

$$qg \rightarrow \gamma\gamma q \tag{3.28}$$

$$qg \rightarrow q\gamma \tag{3.29}$$

$$q\overline{q} \rightarrow \gamma g \tag{3.30}$$

where the parton/gluon fragments and give an additional photon in the final state in the last two processes. The g g $\rightarrow$ g γ process is not implemented in DIPHOX. A fragmentation function must be chosen in order to compute the above cross-sections.

In addition to the irreducible background an important background in the photon decay mode stems from QCD Jet-γ and Jet-Jet. Jets contain many high energetic mesons, the neutral pions π^0, which lead to 'photon-like' events in the EM calorimeter. This background is thus called reducible. A π^0 decays into two photons, and if the pion have a high transverse momentum compared to the pion mass, the two photons are collimated, appearing as single (fake) photon because the detector is unable to properly resolve them. Thus $\pi^0\pi^0$ coming from two jets appear as two single photons when mesonic decays occur. In addition during hadronization many pions are produced together with photons, i.e. π^0 γ. Again the π^0 decays into photons which are not properly resolved

by the detector. π^0 γ appears as two single photons and contribute to the reducible background. These misidentified photons are worrisome since enormous amount of pions are produced inside a jet.

Photons not produced by mesonic decays are contaminated by $\pi^0\pi^0$ and $\pi^0\gamma$ events. In addition there are more reducible backgrounds; electrons misidentified as photons due to $\gamma \to e^+e^-$ or tracking inefficiency, and there are more complicated processes which require full simulation. DIPHOX however, predicts the pion rate inside a jet via fragmentation of partonic subprocesses. The background from π^0 γ consists of two contributions in DIPHOX:

• The π^0 is emitted collinearly by a parton and the photons come directly in the partonic subprocess. This contribution has one fragmentation function[4].
• The π^0 and the photon are emitted collinearly by a parton. This contribution has two fragmentation functions.

The $\pi^0\pi^0$ contribution requires a fragmentation function for each of the partons emitting pions. The pions constitute the bulk of the misidentified photons. The background in the diphoton mode is fitted by using an exponential function.

3.9.3 Isolation Cut

As an enormous amount of high energetic pions are produced in a jet one needs a huge supression factor to get rid of the reducible background. This is done by isolation. In DIPHOX a photon is said to be isolated if, in a cone of rapidity and azimuthal angle about the photon direction, the amount of hadronic transverse energy E_T^{had} is smaller than some value E_T^{max} fixed by the experiment[18]:

$E_T^{had} \leq E_T^{max}$ inside $(Y - Y_\gamma)^2 + (\Phi - \Phi_\gamma)^2 \leq R^2$

where R is set to 0.4. For the ATLAS experiment the maximal transverse energy allowed inside a cone lies between 5 and 15 GeV [14]. At too low values, less than 5 GeV, transverse energy is saturated by hadrons coming from multiple interactions and pile up. So at 5 to 15 GeV the transverse energy stems from hard partonic interactions only. But these values are for the partonic level. In a experimental realistic situation these values are different. Experimentally, isolations cuts mean that we check if there is a large energy deposit around the photon candidate.

3.9.4 Photon Conversions

The photons have to traverse significant amounts of material of the ID cavity before reaching the EM calorimeter where they are finally detected. They interact with this material and some 30% of them are converted into e^+e^- pairs before reaching the calorimeter. 75% of these conversions happen inside a volume (R$<$ 80 cm, |z|$<$280

[4] A fragmentation function is a probability density function describing the hadronization of jets. They parameterize the mechanism how partons (quarks or gluons) turn into hadrons in the final state.

Cuts	DIPHOX(mb)	PYTHIA(mb)
P_t>20 GeV	$1.665 \cdot 10^{-7}$	$1.653 \cdot 10^{-7}$
+ |y|<2.5	$8.867 \cdot 10^{-8}$	$8.855 \cdot 10^{-8}$
+ $M_{\gamma\gamma}$>900 GeV	$1.025 \cdot 10^{-11}$	$1.026 \cdot 10^{-11}$

Table 3.31: Comparison of Born and Box contributions from DIPHOX and PYTHIA with cuts.

cm) in which they are efficiently identified. Conversions ocurring outside this region are less harmful because the electrons do not bend much in the azimuthal direction before entering the EM calorimeter, and hence look more like unconverted photons [10]. The conversions can be recovered with an overall efficiency of 60%.

ATLFAST does not take this effect into account. What is required is full simultions which is beyond the scope of this study.

3.9.5 Results

This study compares the Born and Box contributions with different cuts at Leading Order (LO) in DIPHOX and PYTHIA. Cuts on the transverse momentum, P_t, are added subsequently together with cuts on the rapidity, Y, and the invariant mass of the final state photons, $M_{\gamma\gamma}$.

DIPHOX is, see table 3.31, compatible with PYTHIA at LO. DIPHOX is perfectly in agreement with TEVATRON data [19]. Herwig 6.3 on the other hand, predict a cross-section which is a factor of 5 too small [5].

For the cross-section calculation of the reducible background cuts are imposed at the generator level in DIPHOX and all calculations are at LO only. The minimum transverse momentum of the photons is set to 20 GeV. The rapidity is set to |Y|<2.5 and the minimum invariant mass of the two photons is set to 900 GeV. The photon identification efficiency is set to 0.8 for each of the photons [11]. CTEQ5L is used as a Parton Distribution Function. In addition, fragmentation functions are chosen for partons fragmenting into a photon or a pion. In case of the photons there are no LO fragmentation functions in DIPHOX. BFG [40], which is at NLO only, is used as a fragmentation function for photons. In order to be consistent, KKP [41] at NLO is used as a fragmentation function for the pions. In principle, one should use a LO Fragmentation Function when LO calculations are made. But since the theoretical errors are large at LO (due to the scale dependence), the errors coming from this are negligible. In order to be consistent with PYTHIA the scale chosen for the calculations is $P_{T\gamma 1}+ P_{T\gamma 2}$ for the photons in the final state, unlike in [14] where the scale was (incorrectly) given to be $\sqrt{P_{T\gamma 1} + P_{T\gamma 2}}$.

The cross-section of the born and box contribution is, see table 3.31, $1.026 \cdot 10^{-2}$ pb. The contribution from the bremsstrahlung processes, estimated by DIPHOX, are of order $3.1 \cdot 10^{-3}$pb. The contribution from $q\overline{q} \rightarrow$ g $\gamma \rightsquigarrow$ g γ γ is negligable, see table 3.32. The cross-section ratio between the bremsstrahlung, and the born and box contributions, is given by:

Process	$\sigma(pb)$
q g $\to \gamma\ \gamma$ q	$2.880{\cdot}10^{-3}$
q g $\to$ q $\gamma \rightsquigarrow$ q $\gamma\ \gamma$	$2.515{\cdot}10^{-4}$
$q\overline{q} \to$ g $\gamma \rightsquigarrow$ g $\gamma\ \gamma$	$3.839{\cdot}10^{-7}$

Table 3.32: The cross-section contributions from different bremstrahlung processes from DIPHOX.

Process	$\sigma(pb)$
f g $\to \gamma\ \gamma$ f	3.219
$f\overline{f} \to$ g γ	$9.098{\cdot}10^{-1}$
g g $\to$ g γ	$2.391{\cdot}10^{-4}$

Table 3.33: The cross-section contributions from different bremstrahlung processes from PYTHIA.

$$\frac{\sigma_{bremsstrahlung}}{\sigma_{born+box}} = \frac{3.1 \cdot 10^{-3}}{1 \cdot 10^{-2}} \approx 0.31 \tag{3.31}$$

or 31% of the born and box contribution. Since DIPHOX is not a genuine event generator, i.e. there is no hadronization, PYTHIA is used to generate the required events. The bremsstrahlung background is included in the generation by correspondingly scaling up the born and box cross-section by 31% for a given luminosity. In reality there is a possibillity that the different shapes of the two contributions makes this approach simplistic. This approach of scaling up the born and box cross-section is used in e.g [11].

As mentioned earlier, DIPHOX does not take into account the g g $\to$ g γ contribution. In order to evalute this background it is compared to the other bremstrahlung processes in PYTHIA where there is no fragmentation or isolation cut, see table 3.33. It turns out that g g $\to$ g γ has the lowest contribution to the overall bremstrahlung cross-section. It amounts, already before fragmentation, to only about 2.4 % of the born and box background. After fragmentation this cross-section is reduced further. This is easily seen by comparing the other two processes with their fragmented counterparts in table 3.32. Thus g g $\to$ g γ (from table 3.33) as q $\overline{q} \to$ g $\gamma \rightsquigarrow$ g $\gamma\ \gamma$ (from table 3.32) are neglected.

Calculating the contributions from jet-jet and jet-γ is more difficult. DIPHOX breaks down when calculating the contribution coming from the two fragmentation parts of the $\pi^0\gamma$ and $\pi^0\pi^0$ background, see tables 3.34 and 3.35.

DIPHOX just reproduces the same cross-section in the region P_t<52 GeV, which is difficult to understand. Do the cross-sections in the region P_t<52 increase or not? We are interested in the cross-sections given by the cut P_t>20 GeV. Fortunately there exists

P_t Cuts	$\sigma(pb)$
P_t>100	$5.899 \cdot 10^{-5}$
P_t> 70	$8.925 \cdot 10^{-5}$
P_t> 60	$8.872 \cdot 10^{-5}$
P_t> 58	$8.878 \cdot 10^{-5}$
P_t> 56	$8.870 \cdot 10^{-5}$
P_t> 54	$8.856 \cdot 10^{-5}$
P_t> 52	$8.888 \cdot 10^{-5}$
P_t> 50	$8.888 \cdot 10^{-5}$
P_t> 40	$8.888 \cdot 10^{-5}$
P_t> 20	$8.888 \cdot 10^{-5}$

Table 3.34: The cross-section contributions from the two fragmentation part of $\pi^0\gamma$

P_t Cuts	$\sigma(pb)$
P_t>100	$2.441 \cdot 10^{-5}$
P_t> 70	$4.574 \cdot 10^{-5}$
P_t> 60	$4.566 \cdot 10^{-5}$
P_t> 58	$4.543 \cdot 10^{-5}$
P_t> 56	$4.566 \cdot 10^{-5}$
P_t> 54	$4.560 \cdot 10^{-5}$
P_t> 52	$4.554 \cdot 10^{-5}$
P_t> 50	$4.554 \cdot 10^{-5}$
P_t> 40	$4.554 \cdot 10^{-5}$
P_t> 20	$4.554 \cdot 10^{-5}$

Table 3.35: The cross-section contributions from $\pi^0\pi^0$

Process	$\sigma(pb)$
PP $\rightarrow \pi^0\ \gamma$, one fragmentation	$7.582 \cdot 10^{-5}$
PP $\rightarrow \pi^0\ \gamma$, two fragmentations	$8.888 \cdot 10^{-5}$
PP $\rightarrow \pi^0\ \pi^0$, two fragmentations	$4.554 \cdot 10^{-5}$

Table 3.36: Cross-sections for the reducible background.

a constraint on P_t from the particles coming from fragmentation. They have a lower limit on the P_t, which is below the limit on the particles not coming from fragmentation, given by the following equation[5]:

$$P_{h_3} \geq \frac{1}{2}\sqrt{\frac{(E_T^{max})^2 + (M_{min})^2}{cosh(\frac{Y_{h_3} - Y_{h_4}}{2})}} - \frac{1}{2}E_T^{max} \tag{3.32}$$

where M_{min} is the lowest invariant mass of two particles. Y_{h_3} and Y_{h_4} is the rapidity of the pion/photon, and P_{h_3} is the transverse momentum of the pion/photon coming from fragmentation. Using the cuts mentioned above, the lowest P_t of the fragmented particles is 65.9 GeV. This means that the cross-section is constant up to this point. This is also visible in the tables 3.34 and 3.35. The cross-section clearly fluctuates in the region P_t<60 GeV, e.g the cross-section in table 3.34 given by the cut P_t> 56 GeV and P_t> 54 GeV are smaller than the cross-section given by P_t> 60 GeV. The cross-section of the total reducible background is given by table 3.36.

Rejection factors of 2 to 3 per pion is possible [18] thus making this background even smaller. With a rejection factor of 2 per pion this background amounts to 0.94% of the born and box background. Increasing the rejection factor to three yields a background which is only 0.58% of the born and box background. Given the fact that the pions constitute the main source of the fake background, the other kinds of reducible background, like electrons appearing as photons, are smaller, and thus reducible background is not a problem in the search for the gravitons at ATLAS. They are therefore neglected in this study.

This study looks at a background consisting of born and box processes, and 'bremsstrahlung processes' which are included by scaling up the born and box cross-section by 31%. The efficiency evolution of the background is given table 3.37. Cuts on the generator level, as specified above in this section, are applied. 133380 events are generated which corresponds to an integrated luminosity of 10000 fb^{-1}. Graviton masses between 1000 GeV and 2200 GeV are generated. The same cuts as for the background are applied on the generator level, except for, naturally, the 900 GeV cut on the invariant mass. All the mass points are artificially produced with an integrated luminosity of 10000 fb^{-1}. The background is very well described by an exponential and the signal with a gaussian, see figure 3.91. The χ^2 varies between 1.0 and 1.3.

[5]Thanks to Jean Philippe Guillet

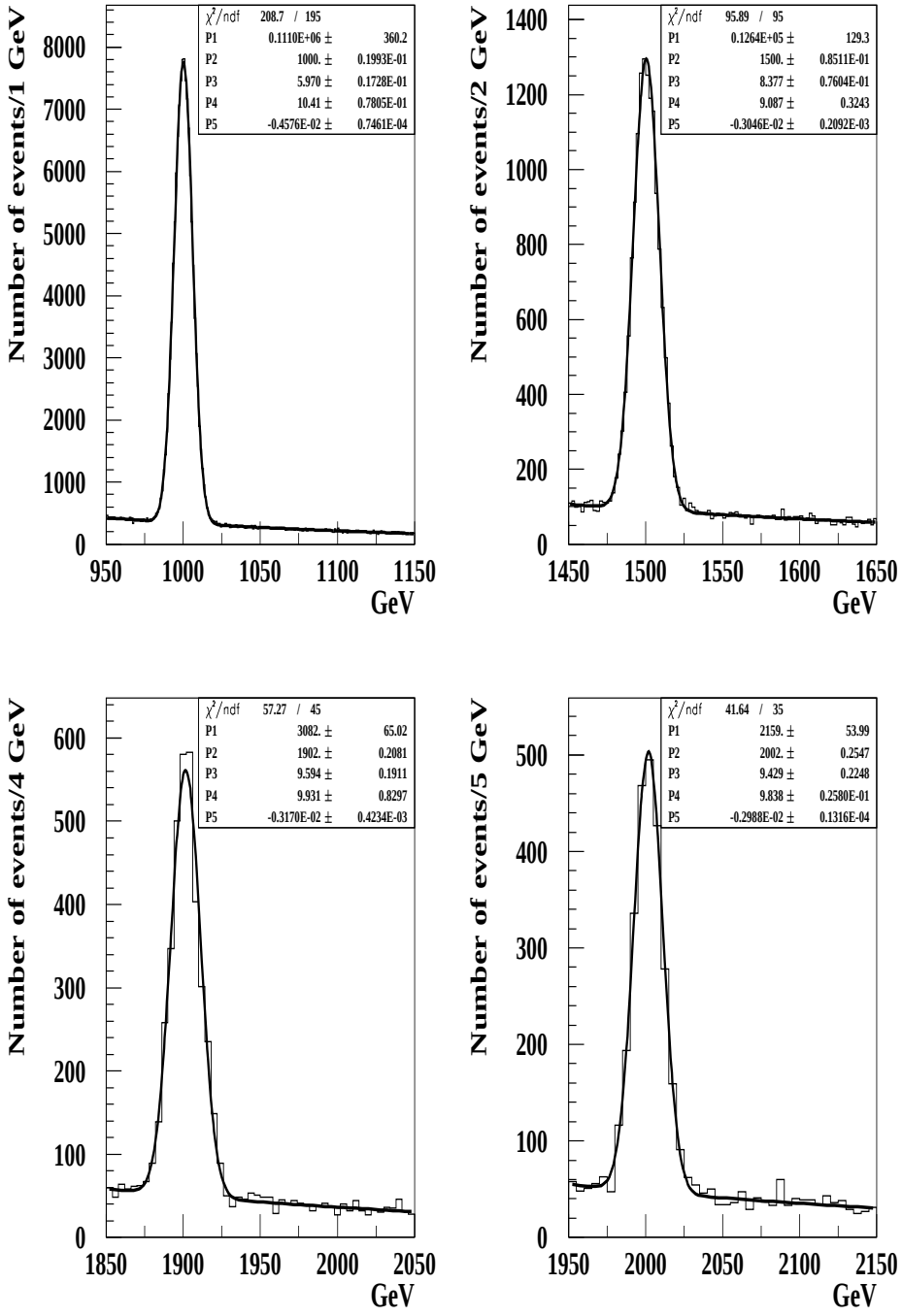

Figure 3.91: Graviton resonances with different mass fitted with a gaussian above the photon background. Cuts specified in the text are applied. ISR and FSR switched on. All the mass points (with backgrounds) are artificially produced with an integrated luminosity of 10000 fb^{-1}.

Radiation	$\epsilon_{accetance}$	$\epsilon_{identification}$	$\epsilon_{overall}$
No Radiation	0.9831	0.64	0.6292
Only ISR	0.9615	0.64	0.6154
Only FSR	0.9855	0.64	0.6307
ISR and FSR	0.9642	0.64	0.6171

Table 3.37: Different efficiencies for different scenarios for the photon background with a cuts on the generator level as specified in the text. $\epsilon_{acceptance}$ is the acceptance, $\epsilon_{identification}$ is the photon identification efficiency and $\epsilon_{overall}$ is the overall efficiency. CTEQ5L used as PDF.

μ **(GeV)**	$MW_{cteq5l}(GeV)$	N_S	N_B	N_S^{min}	ϵ_{cteq5l}	$(\sigma B)^{min}(fb)$
1000	$\pm$18.04	712.3	76.6	43.8	0.6078	0.721
1500	$\pm$25.02	80.6	15.0	19.4	0.5782	0.336
1601	$\pm$25.66	55.6	10.8	16.4	0.5749	0.285
1701	$\pm$27.05	38.8	8.2	14.2	0.5644	0.252
1802	$\pm$27.08	27.1	5.9	12.2	0.5469	0.223
1902	$\pm$28.79	19.9	4.3	10.4	0.5526	0.188
2002	$\pm$28.00	13.7	3.3	10.0	0.5176	0.193
2102	$\pm$30.84	10.7	2.6	10.0	0.5440	0.184
2203	$\pm$31.50	7.8	2.1	10.0	0.5267	0.190

Table 3.38: The mass windows (MW) for different masses, given by $\mu \pm 3\sigma_m$, where the background and signal events are obtained by integration and fitting. The number of signal events beneath a gaussian,N_S. The number of background events inside the mass window, N_B. The minimal signal events needed to detect the resonance, N_S^{min}. The acceptance inside a mass window, ϵ_{cteq5l}, and the minimum cross-section needed to detect the graviton, $(\sigma B)^{min}$.

The efficiency of this channel is higher than the electron and muon channel. The main reason is that the photons do not radiate FSR. But the relatively high efficiency is also due to the fact that ATLFAST does not take into account photon conversions. There is also a possibility that the effects of angular distributions, discussed in the next section, improve the $\gamma\gamma$ efficiency.

The minimum production cross-section needed to detect the graviton at a 5σ sensitivity is smaller at almost every graviton mass compared to the other channels. And the mass resolutions, which are reflected in the size of the mass windows, are similar to the electron channel, as expected. Table 3.38 and figure 3.92 summarizes the results for this channel.

The discovery reach for the photons is about 2.1 TeV. The discovery mass limit for the electrons when there is no radiation or only ISR switched on varies, depending on the PDF and the radiation scenario, between 2000-2125 GeV, see table 3.23. Thus the discovery reaches are compatible when FSR(or FSR and ISR) is switched off.

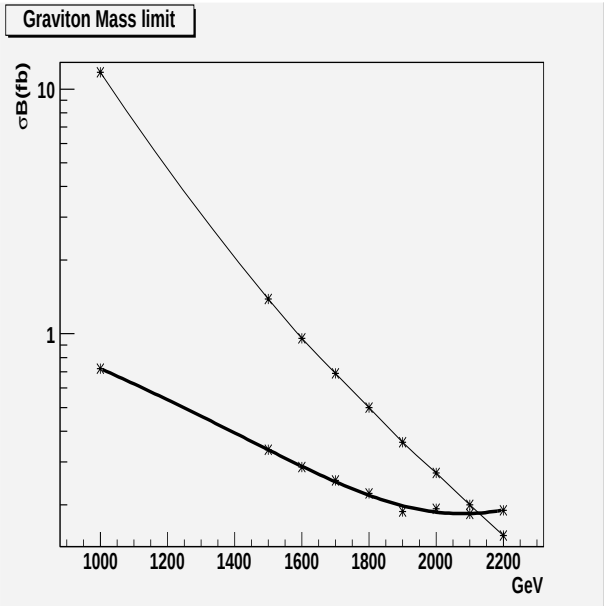

Figure 3.92: Cross-sections for $G \to \gamma\gamma$ in the R-S model (light curve) and the smallest detectable cross-setion (black).

3.10 Graviton Discrimination in ATLAS

We have until now looked at simulated graviton resonances, but in a real experiment we cannot take for granted that such resonances, if observed, are gravitons. There exist a number of possible non-SM scenarios which predict exotic spin-1 particles like the heavy Z'. In order to show that a resonances is a graviton and not some other exotic particle the angular distribution is analyzed. The angular distribution is a function of the spin of the resonance. Since the graviton resonance is a spin-2 particle it can be distinguished from the spin-1 Z', or other exotic particles with spin 0 or 1. This section look at the angular distributions in the electron decay mode. At the end angular distributions in the photon decay mode are shortly discussed.

3.10.1 Angular Distributions

In the electron decay mode, θ^* is defined as the angle, in the graviton center of mass system (cms), between the e^- and the incident quark or gluon. In the rest frame of the graviton the spin is conserved. The spin is not a rotation in ordinary sense because it is quantized [22]. Since the spin property of the resonance is measured in the center of mass frame, a Lorentz transformation is required. The resonance is boosted back into the center of mass frame where the angular distributions are measured. The angular distribution is given by the following equation:

$$cos\theta^* = \frac{\mathbf{p}_{\mathbf{e^-}}^{\mathbf{G^*_{cms}}} \cdot \mathbf{p}_{\mathbf{q,g}}^{\mathbf{G^*_{cms}}}}{|p_{e^-}^{G^*_{cms}}||p_{q,g}^{G^*_{cms}}|} \tag{3.33}$$

However, in a real experiment the quark or gluon direction cannot be determined from p-p collisions. But the quark or gluon direction is approximated by the G^* direction [47]. This is done by looking at the angle between the electron in the cms and dielectron system in the laboratory system. This approximation assumes that the incoming quarks or gluons move in the direction of the resonance. This angular distribution is given by:

$$cos\theta^* = \frac{\mathbf{p}_{\mathbf{e^-}}^{\mathbf{G^*_{cms}}} \cdot \mathbf{p}_{\mathbf{G\to e^+e^-}}^{\mathbf{lab}}}{|p_{e^-}^{G^*_{cms}}||p_{G\to e^+e^-}^{lab}|} \tag{3.34}$$

This approximation is used in this analysis.

There are large differences between the spin 2, spin 1 and spin 0 distributions which make it possible to distinguish the graviton resonances if we have sufficient statistics. Theoretically the graviton and the Drell-Yan background yield distributions with different $\cos\theta^*$ dependencies, see table 3.39.

The distribution of the Drell-Yan background goes as $\sim \cos^2\theta^*$, making it possible to discriminate it from the graviton distributions with higher order of $\cos\theta^*$. Experimentally the distributions are a little different from the theoretical distributions shown in figure 3.93. The cut of $|\eta|<2.5$ in the detector ensures that events at large $|\cos\theta^*|$ are

Channel	Distributions
$q\overline{q} \rightarrow G^* \rightarrow f\overline{f}$	1 - $3\cos^2\theta^*$ + $4\cos^4\theta^*$
gg$\rightarrow G^* \rightarrow f\overline{f}$	1 - $4\cos^4\theta^*$
$q\overline{q} \rightarrow \gamma^*/\mathrm{Z}^0 \rightarrow f\overline{f}$	1 + $\cos^2\theta^*$

Table 3.39: Angular distributions of the graviton in the center of mass rest frame and the Drell-Yan background.

not accepted. For lighter gravitons the effect is relatively strong. Comparing the figures 3.94-3.101 with 3.93 we see that at 500 GeV the majority of the rejected events are at large $|\cos\theta^*|$ values. For heavy gravitons the acceptance loss is more due to lower values of $|\cos\theta^*|$. This is most clearly seen in the figures showing the distribution of $q\overline{q}$ annihilation. The peak around $\theta^*=\frac{\pi}{2}$ is smaller when the graviton is heavier. In gg fusion, the top is flattened for heavy gravitons due to less events removed at high $|\cos\theta^*|$.

In ATLAS the angular distribution of the graviton resonance is a combination of the contributions from the channels $gg, q\overline{q} \rightarrow G \rightarrow f\overline{f}$. As shown in figure 3.102 the angular distributions change with the graviton mass. The process $gg \rightarrow G \rightarrow f\overline{f}$ dominates completly at 1 TeV masses. As the graviton masses rise their production is dominated by $q\overline{q} \rightarrow G \rightarrow f\overline{f}$. The angular distribution of $q\overline{q}$ annihilation pulls up the overall G^* distribution at high values of $|\cos\theta^*|$. At 2 TeV the shape differs from the angular distributions coming from 1 TeV gravitons. In addition the shapes also differ with the choice of PDF.

The 2 TeV resonance given by CTEQ5L differs from the other 2 TeV resonances. It shows that $q\overline{q} \rightarrow G \rightarrow f\overline{f}$ becomes as dominant as the gg process. By closer investigation this is indeed the case. Table 3.40 shows the ratios between the $q\overline{q}$ and gg process. At 2.2 TeV the $q\overline{q}$ process is about 41% and 46% of the gg process when we use OWEN set 1.1 and MRST(h-g) respectively. But with CTEQ5L the $q\overline{q}$ increases to about 82%, and as seen earlier the newer PDFs favour lower overall cross-sections for the resonances. Because of the big differences, a study of PDFs and graviton resonance cross-sections is needed. Either the newer PDFs underestimate contributions from the gg process or the older ones overestimate it. The only thing that is clear from our current PDFs is that $q\overline{q}$ takes bigger part in the production of the gravitons resonances when the masses increase. But it is not clear to what extent. In any case this study shows that information about the production mechanism i.e. the production rate from the gg and $q\overline{q}$, is retrieved from the angular distributions.

In this study the graviton masses were produced with 100 times more statistics than what is achievable at the LHC after four years of running. In real experiments we confront the problem of low statistics if a resonance of large mass is detected. This is already apparent for a graviton at 2 TeV in figures 3.100-3.101 which was produced with 100 times more events. With sufficient data, the spin is determined from a fit to the angular distribution. A likelihood analysis is required in order to evaluate the discovery reach of the experiment, in terms of its ability to determine the spin of the graviton. This is beyond the scope of this study.

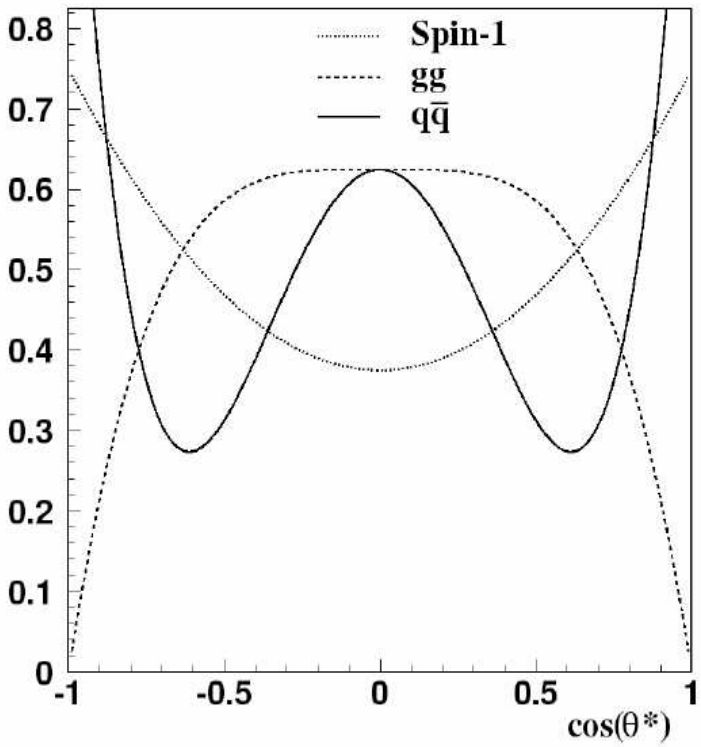

Figure 3.93: Angular distributions of various processes in the electron decay mode. θ^* is the polar angle of the outgoing particle in the graviton rest frame. Plot taken from [1]

However a likelihood analysis was performed in reference [2]. A likelihood function was constructed and evealuated for two simple hypotheses. The spin of the resonance was said to be detectable with 90% confidence for graviton masses as high as 1720 GeV [2]. However this study was done using HERWIG 6.3 which does not include Final State Radiation. This implies that the 90% confidence should be lower because final state radiation yields less data. In addition, a study done by Robert Cousins et al. [38] puts a question mark on the interpretation of the likelihood analysis of [2]. According to them, the inclusion of the possibility of a spin-0 resonance makes identification of spin-1 or spin-2 more difficult, recommending caution when dealing with interpretation of a likelihood ratio of even simple hypotheses.

Finally, angular distributions might contribute to explain the high efficiency of the $\gamma\gamma$ channel compared to the electron channel. Table 3.41 shows the angular distributions of the $\gamma\gamma$ channel. The distribution fron quark annihilation is identical to the gluon fusion distribution in the electron channel.

As in the electron channel the graviton production from quark annihilation increases with higher mass. In fact, the ratios between the cross-sections from quark annihilation and gluon fusion are identical to the case with electrons, see table 3.42. The $q\overline{q}$ initiated photons are more centrally distributed than electrons. This might also explain, in addition to the reasons mentioned in section 3.9, the high efficiency of the $\gamma\gamma$ channel. However, more study is required and this is beyond the scope of this thesis.

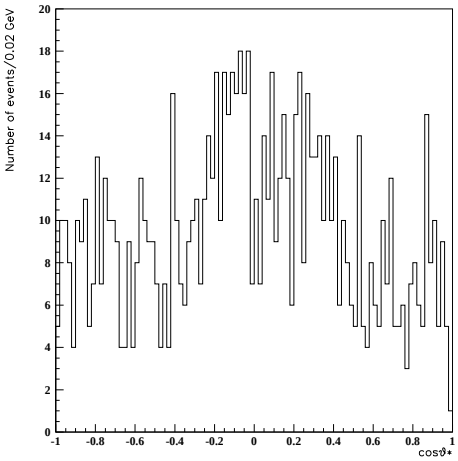

Figure 3.94: Angular distribution for a 500 GeV graviton resonance produced by $q\overline{q}$ annihilation in the electron decay mode.

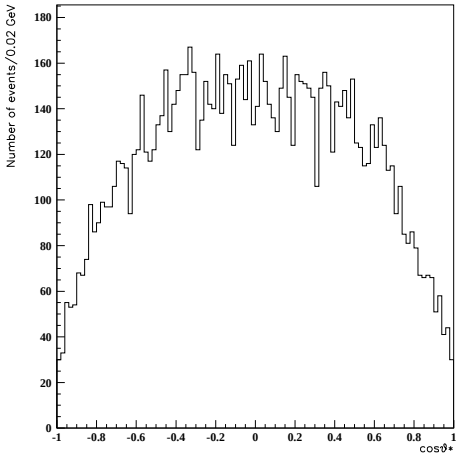

Figure 3.95: Angular distribution for a 500 GeV graviton resonance produced by gg fusion in the electron decay mode.

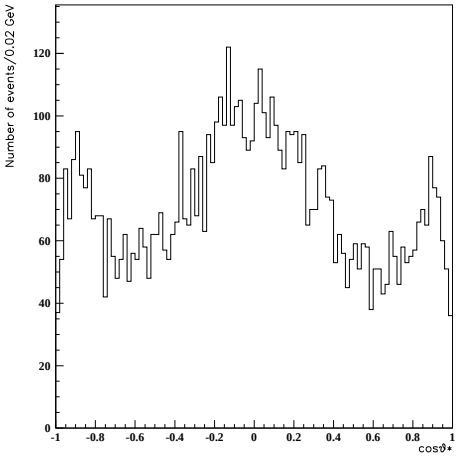

Figure 3.96: Angular distribution for a 1 TeV graviton resonance produced by $q\overline{q}$ annihilation in the electron decay mode. Produced with 100 times more statistics.

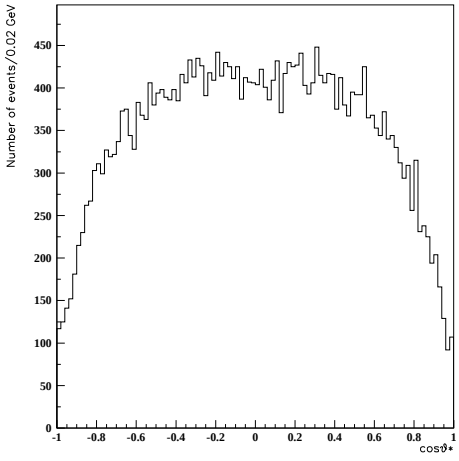

Figure 3.97: Angular distribution for a 1 TeV graviton resonance produced by gg fusion in the electron decay mode. Produced with 100 times more statistics.

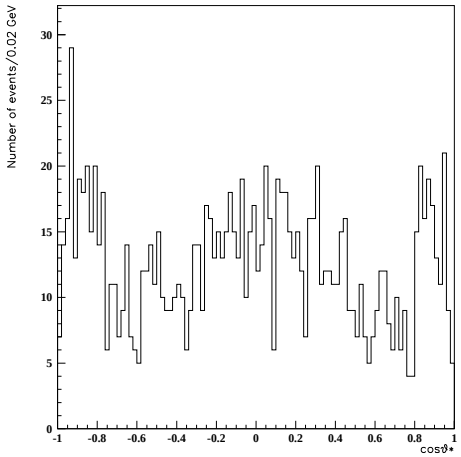

Figure 3.98: Angular distribution for a 1.5 TeV graviton resonance produced by $q\overline{q}$ annihilation in the electron decay mode. Produced with 100 times more statistics.

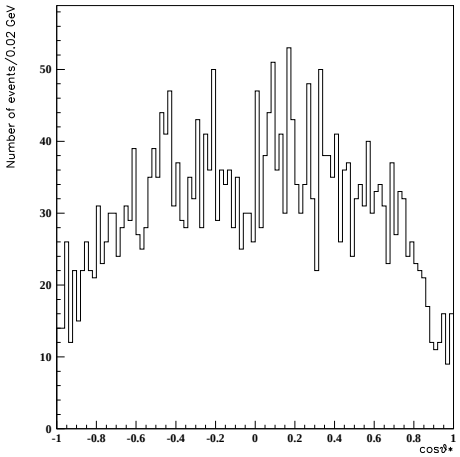

Figure 3.99: Angular distribution for a 1.5 TeV graviton resonance produced by gg fusion in the electron decay mode. Produced with 100 times more statistics.

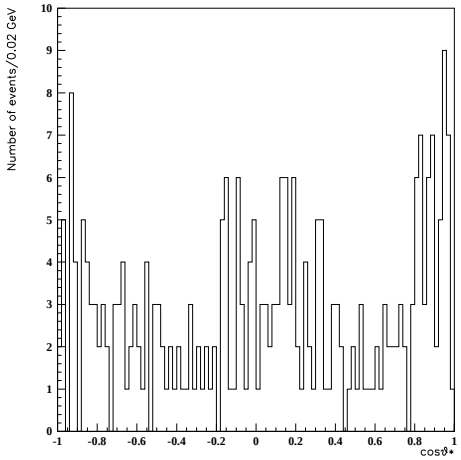

Figure 3.100: Angular distribution for a 2 TeV graviton resonance produced by $q\overline{q}$ annihilation in the electron decay mode. Produced with 100 times more statistics.

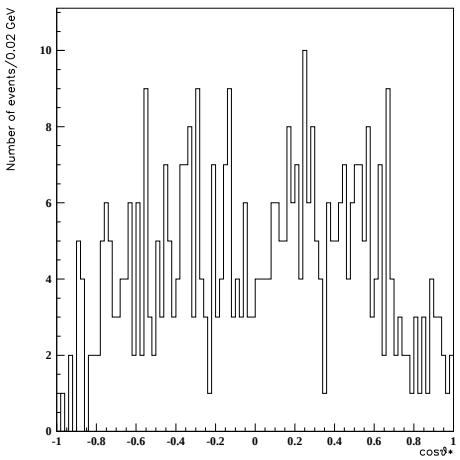

Figure 3.101: Angular distribution for a 2 TeV graviton resonance produced by gg fusion in the electron decay mode. Produced with 100 times more statistics.

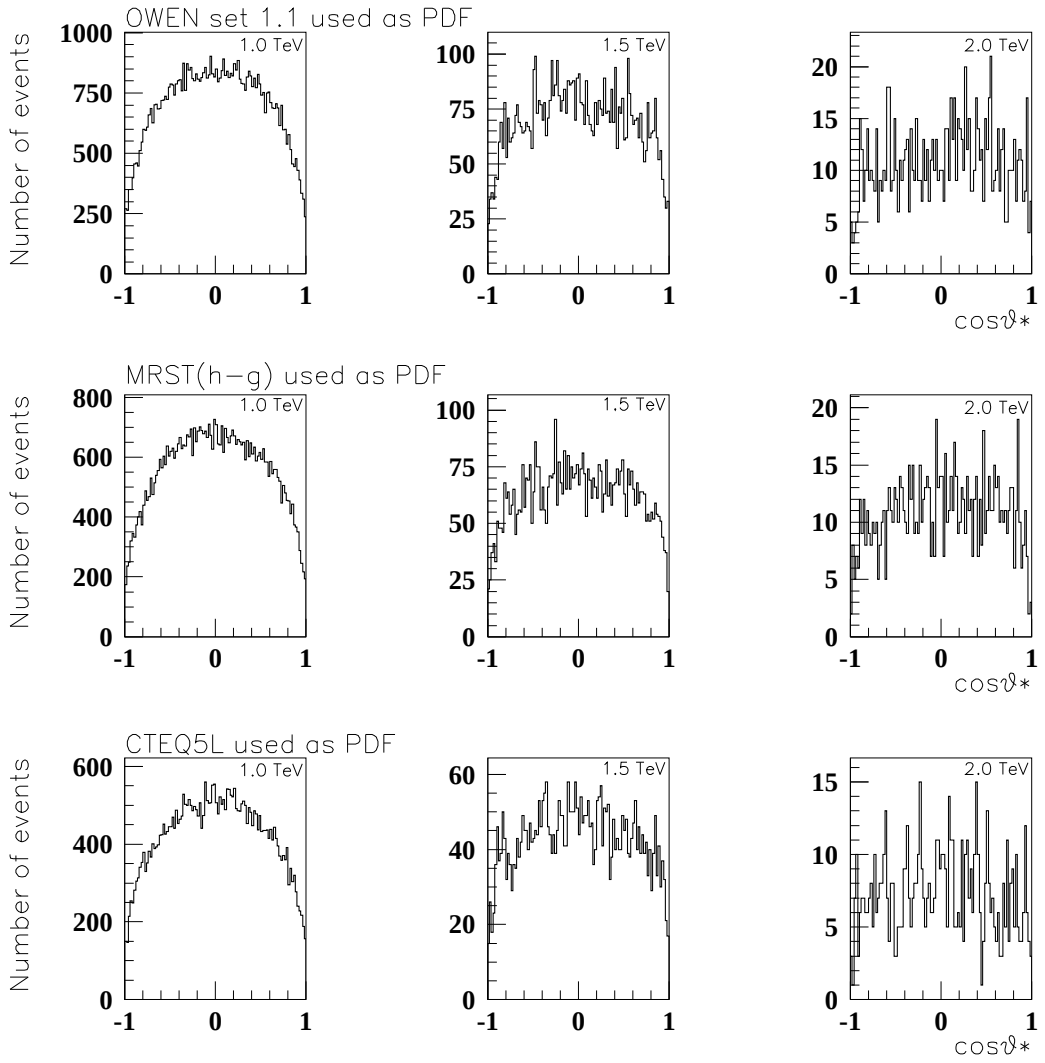

Figure 3.102: Angular distributions of outgoing e^- in the graviton rest frame for different masses and PDFs with 100 times more statistics. No trigger cuts applied.

mG (GeV)	$(\frac{\sigma_{q\overline{q}}}{\sigma_{gg}})_{owen}$	$(\frac{\sigma_{q\overline{q}}}{\sigma_{gg}})_{mrst}$	$(\frac{\sigma_{q\overline{q}}}{\sigma_{gg}})_{cteq5l}$
500	0.0575	0.0872	0.1031
1000	0.1246	0.1771	0.2401
1500	0.2188	0.2827	0.4388
1600	0.2413	0.3013	0.4901
1700	0.2675	0.3370	0.5339
1800	0.2871	0.3559	0.5889
1900	0.3160	0.3780	0.6418
2000	0.3456	0.4113	0.7034
2100	0.3764	0.4319	0.7538
2200	0.4073	0.4588	0.8201

Table 3.40: The ratio between the cross-sections $q\overline{q} \rightarrow G \rightarrow e^+e^-$ and $gg \rightarrow G \rightarrow e^+e^-$ for different PDFs at different resonance masses.

Channel	Distributions
$q\overline{q} \rightarrow G^* \rightarrow \gamma\gamma$	1 - $4\cos^4\theta^*$
gg$\rightarrow G^* \rightarrow \gamma\gamma$	1 + $6\cos^2\theta^*$ + $\cos^4\theta^*$

Table 3.41: Angular distributions of the $\gamma\gamma$ graviton in the center of mass rest frame.

mG (GeV)	$(\frac{\sigma_{q\overline{q}}}{\sigma_{gg}})_{cteq5l}$
500	0.1033
1000	0.2429
1500	0.4377
2000	0.6969

Table 3.42: The ratio between the cross-sections $q\overline{q} \rightarrow G \rightarrow \gamma\gamma$ and $gg \rightarrow G \rightarrow \gamma\gamma$ for CTEQ5L at different resonance masses.

Chapter 4

Conclusion and Outlook

The ATLAS detector is capable of discovering graviton resonances as predicted by the Randall-Sundrum model. The dielectron and diphoton channels are the best for detection, due to their good energy resolution.

In this study we looked at the decay modes $G^* \rightarrow e^-e^+, \mu^-\mu^+$ and $\gamma\gamma$ of a massive graviton. The expected limit in the dielectron mode from [2] was reproduced using PYTHIA without Final State Radiation. PYTHIA and Herwig are compatible when FSR is switched off. Because of lack of realism in omitting FSR, a study of radiation was done, showing a loss of efficiency due to an increase of single lepton events. We saw that FSR reduces the efficiency to such a degree that the mass limit of 2080 GeV from [2] was too optimistic. This limit was then corrected to 1800 GeV for CTEQ5L Parton Distribution Function. But what this limit really is, is not obvious. It was clearly shown that the PDFs affect the results. In addition it seems that the cuts ATLFAST imposes on the leptons, when we turn on FSR, are too severe. Efficiency differences of 25% were shown. Full simulation is required in this issue. As well as taking into account systematic errors from the PDFs and the acceptance. The limits are model independent as long as the widths of the gravitons are much smaller than the experimental resolution, and as long as the couplings are universal.

In the muon and photon channel the expected discovery limit was found to be 1325 and 2100 GeV respectively. For muons the limit is corrected by 375 GeV compared to reference [1]. The limit for the photons has never been determined before.

It was shown that PYTHIA and DIPHOX are compatible at Leading Order. The background from QCD jets will not be a problem for a heavy graviton. The discovery limit of 2.1 TeV seems too optimistic especially since ATLFAST does not take into account photon conversions. Again a full simulation study is required. In all the channels it was shown that a gaussian is a suitable function for the signal regardless of radiation.

Angular distributions can be used to discriminate gravitons from other exotic resonances like the Z'. In addition it was shown that angular distributions can be used to determine the production mechanism of the gravitons.

LHC, with its high center of mass energy, makes it possible to probe a large number graviton masses. Opening up the possibility of detecting the graviton. Such a discovery

would revolutionize physics, answering many unsolved questions in physics, such as Dark Matter or hierarchy problems. Conversely the non-observation of these resonances at LHC would put severe constraints on the Randall-Sundrum model and other therories, if not rejecting them completely.

Bibliography

[1] M.A. Parker *Searching for graviton resonances at the LHC*, Talk presented at ATLAS Exotics Working Group Meeting, November 9. 2001

[2] Allanach, Odagiri, Parker and Webber *Searching for narrow graviton resonances with the ATLAS detector at the Large Hadron Collider*, J. High Energy Phys. 09 (2000) 019 12. October 2000

[3] Sjöstrand, et al. *High-Energy-Physics Event Generation with Phythia 6.1*, Comput.Phys.Commun.135:238-259,2001 October 2000.

[4] Bijnens, Eerola, Maul, Månsson and Sjöstrand, *QCD Signatures of Narrow Graviton Resonances in Hadron Colliders*,Phys. Let. B 503 (2001) 341

[5] Allanach, Odagiri, Palmer, Parker, Sabetfahri and Webber *Exploring small extra deimensions at the Large Hadron Collider*, ATL-PHYS-2002-031 December 17. 2002

[6] B.R. Martin and G. Shaw, *Particle Physics*, John Wiley and Sons, 1997

[7] W. R. Leo, *Techniques for nuclear and particle physics experiments-A how-to approach*, Springer-Verlag, 1994

[8] CERN, *LHC - Challenges in Accelerator Physics*, online, May 2. 2002
`http://press.web.cern.ch/lhc/general/acphys.htm`

[9] Yuriy Pylypchenko, *Study of χ_c production in pA interactions at HERA-B* , Doctor Scientarium thesis, University of Oslo, November 2004

[10] *ATLAS: Detector And Physics Performance Technical Design Report, Vol. 1* ,CERN-LHCC-99-14 May 25 1999

[11] *ATLAS: Detector And Physics Performance Technical Design Report, Vol. 2* ,CERN-LHCC-99-15 May 25 1999

[12] Unni I. Fuskeland, *Simulation of a search for the Standard Model Higgs boson in the $H \to \gamma\gamma$ channel at LHC/ATLAS*, Cand. Scient. tesis, University of Oslo, June 2002

[13] Jean Philippe Guillet *DIPHOX version 1.2* , online

[14] W. Giele et al. *The QCD / SM Working Group: Summary Report*, FERMILAB-CONF-02-410, Apr 2002.

[15] Lisa Randall and Raman Sundrum *A Large Mass Hierarchy from a Small Extra Dimension*, Phys. Rev. Let. 83(1999)

[16] Thomas G. Rizzo *Pedagogical Introduction to Extra Dimensions*, ECONF C040802, 2004

[17] Børge Kile Gjelsten *Mass determination of supersymmetric particles in ATLAS*, Doctor Scientarium thesis, University of Oslo, February 2005

[18] Thomas Binoth, Jean Philippe Guillet et al. *A next-to-leading order study of photon-pion and pion pair hadro-production in the light of the Higgs boson search at the LHC* , Eur.Phys.J.direct C4 (2002) 7

[19] Thomas Binoth, Jean Philippe Guillet et al. *A full Next to Leading Order study of direct photon pair production in hadronic collisions*, Eur.Phys.J. C16 (2000) 311-330

[20] Thomas Binoth, Jean Philippe Guillet et al. *A Next-to-Leading Order Study of Pion pair production and comparison with E706 data.*, Edinburgh-2001-19, LAPTH-873-01, Nov 2001. 34pp.

[21] Herbert Goldstein *Classical Mechanics*, [World Student Series] 1980

[22] PC Hemmer *Quantum Mechanics*, [Tapir Akademisk Forlag] 2000

[23] H. Davoudiasl, J.L. Hewett and T.G. Rizzo *Phenomenology of the Randall-Sundrum Gauge Hierarchy Model*, Phys. Rev. Lett. 84, 2080-2083 (2000)

[24] H. Davoudiasl, J.L. Hewett and T.G. Rizzo *Experimental Probes of Localized Gravity: On and 0ff the Wall*, Phys. Rev. D 63, 075004 (2001)

[25] P. Traczyk and G. Wrochna *Search for Randall-Sundrum graviton excitations in the CMS experiment*, http://arXiv.org/abs/hep-ex/0207061.

[26] J. F. Owens *An updated set of parton distribution parametrizations* Phys. Lett. B266 (1991) 126-130.

[27] A. D. Martin, R. G. Roberts, W. J. Stirling, and R. S. Thorne *Scheme dependence, leading order and higher twist studies of MRST partons* Phys. Lett. B443 (1998) 301-307

[28] H.L. Lai et al. *Global QCD Aanalysis of Parton Structure of The Nucleon: CTEQ5 Parton Distributions.* Eur.Phys.J. C12 (2000) 375-392

[29] I. R. Kenyon *The Drell-Yan Process* Rep. Prog. Phys. Vol. 45 (1982)

[30] http://www-bdnew.fnal.gov/tevatron/

[31] http://www-cdf.fnal.gov/

[32] Tracey Pratt *Searches for New Physics at High Diphoton and Dilepton Masses at CDF*, Department of Physics, University of Liverpool, UK. Paper can be found at: http://www-conf.kek.jp/susy04/

[33] Tracey Pratt *CDF Searches for New Physics at High Photon and Dilepton Masses*, Talk given at The 12th International Conference on Supersymmetry and Unification of Fundamental Interactions, Parallel session 6, June 17-23, 2004.

[34] Gennaro Corcella et. al. *HERWIG 6: an event generator for hadron emission reactions with interfering gluons (including supersymmetric processes)*, J. High Energy Phys. JHEP01(2001)010

[35] Muge Karagoz Unel *Searches for Extra Dimensions at the Tevatron*, AIP Conf.Proc.753:400-409, 2005

[36] E. Richter-Was, D. Froidevaux, L. Poggioli, *ATLFAST 2.0 - a fast simulation package for ATLAS*, ATL-PHYS-98-131

[37] R. Früwirth, *Track fitting with non-Gaussian noice*, Computer Physics Communications 100 (1997) 1-16

[38] Robert Cousins et al., *Spin discrimination of new heavy resonances at the LHC*, JHEP11(2005)046

[39] K. Sridhar, *Constraining the Randall-Sundrum model using diphoton production at hadron colliders*, JHEP05(2001) 066

[40] L. Bourhis, M. Fontannaz and J. Ph. Guillet, Eur. Phys. J. C2 (1998) 529

[41] B.A. Kniehl, G. Kramer and B. Pötter, Nucl. Physics. B582 (2000) 514

[42] I. Golutvin et al., *Search for new heavy resonances at the LHC*, hep-ph/0502009, 12 Feb. 2005

[43] G.F. Giudice, *Physics in Extra Dimensions*, Talk given at NORFA Training school, Helsinki, 23-25 May 2002

[44] http://www-d0.fnal.gov/

[45] The DØ Collaboration, *Search for Randall-Sundrum Gravitons in the Dielectron and Diphoton Channel with 200pb^{-1} of Data with the DØ Detector*, Aug. 9 2004, http://www-d0.fnal.gov/

[46] Greg Landsberg, *Collider Searches for Extra Dimensions*, 10 Dec. 2004, FERMILAB-CONF-04-399-E-T, SSI-2004-MOT006, Dec 2004. 20pp.

[47] Heidi Sandaker, *ATLAS SemiConductor Tracker Development and Physics Simulation*, Doctor Scientarium thesis, University of Oslo, September 2005

Appendix A

Results for no radiation and only FSR switched on

A.1 No Radiation

Tables with parameters obtained with ISR and FSR switched off for MRST(h-g) and CTEQ5L. Discovery limits are derived from the plots in the main text.

μ **(GeV)**	$MW_{cteq5l}(GeV)$	N_S	N_B	N_S^{min}	$\epsilon_{mrst(h-g)}$	$(\sigma B)^{min}(fb)$
500	$\pm$10.51	15365.5	864.7	147.0	0.7269	2.022
1000	$\pm$15.36	657.1	69.7	41.7	0.7611	0.548
1501	$\pm$24.84	77.5	12.1	17.4	0.7236	0.241
1601	$\pm$26.26	54.5	8.7	14.8	0.7198	0.206
1701	$\pm$27.52	38.0	6.4	12.7	0.7021	0.181
1801	$\pm$27.93	26.9	4.6	10.7	0.6913	0.155
1902	$\pm$28.93	19.4	3.4	10.0	0.6814	0.147
2001	$\pm$29.18	14.2	2.7	10.0	0.6739	0.148
2102	$\pm$30.72	10.1	2.1	10.0	0.6417	0.156
2200	$\pm$30.90	7.6	1.5	10.0	0.6414	0.156

Table A.1: The mass windows (MW) for different masses, given by $\mu \pm 3\ \sigma_m$, where the background and signal events are obtained by integration and fitting, respectively. The number of signal events beneath a gaussian, N_S. The number of background events inside the mass window, N_B. The minimal signal events needed to detect the resonance, N_S^{min}. The total efficiency inside a mass window, $\epsilon_{mrst(h-g)}$, and the minimum cross-section needed to detect the graviton, $(\sigma B)^{min}$. MRST(h-g) used as PDF.

μ (GeV)	$MW_{cteq5l}(GeV)$	N_S	N_B	N_S^{min}	ϵ_{cteq5l}	$(\sigma B)^{min}(fb)$
500	$\pm$10.51	13680.9	893.7	149.5	0.7363	2.030
1000	$\pm$18.25	496.3	70.1	41.9	0.7525	0.557
1500	$\pm$24.45	54.4	11.4	16.9	0.7169	0.236
1601	$\pm$26.01	37.6	8.3	14.4	0.7152	0.201
1701	$\pm$27.57	24.9	6.4	12.7	0.6708	0.189
1801	$\pm$28.05	18.4	4.5	10.6	0.6897	0.154
1901	$\pm$29.09	12.7	3.4	10.0	0.6580	0.152
2002	$\pm$29.62	9.6	2.5	10.0	0.6742	0.148
2102	$\pm$30.96	6.7	2.0	10.0	0.6381	0.157
2203	$\pm$36.63	5.1	1.8	10.0	0.6471	0.155

Table A.2: The mass windows (MW) for different masses, given by $\mu \pm 3\ \sigma_m$, where the background and signal events are obtained by integration and fitting, respectively. The number of signal events beneath a gaussian, N_S. The number of background events inside the mass window, N_B. The minimal signal events needed to detect the resonance, N_S^{min}. The total efficiency inside a mass window, ϵ_{cteq5l}, and the minimum cross-section needed to detect the graviton, $(\sigma B)^{min}$. CTEQ5L used as PDF.

A.2 Only FSR

Tables with parameters obtained with ISR switched off and FSR switched on for MRST(h-g) and CTEQ5L. Discovery limits are derived from the plots in the main text.

μ (GeV)	$MW_{cteq5l}(GeV)$	N_S	N_B	N_S^{min}	$\epsilon_{mrst(h-g)}$	$(\sigma B)^{min}(fb)$
498.9	$\pm$12.17	10926.9	790.0	140.5	0.5169	2.718
999.8	$\pm$19.67	428.8	55.5	37.3	0.4966	0.751
1499	$\pm$25.44	46.6	8.3	14.4	0.4351	0.331
1600	$\pm$27.67	33.0	6.2	12.5	0.4358	0.287
1700	$\pm$27.27	23.1	4.4	10.5	0.4268	0.246
1800	$\pm$28.84	15.8	3.4	10.0	0.4061	0.246
1901	$\pm$31.41	11.5	2.5	10.0	0.4039	0.248
2001	$\pm$31.86	8.2	1.9	10.0	0.3892	0.257
2101	$\pm$33.48	6.1	1.3	10.0	0.3875	0.258
2201	$\pm$34.05	4.8	1.0	10.0	0.4051	0.247

Table A.3: The mass windows (MW) for different masses, given by $\mu \pm 3\ \sigma_m$, where the background and signal events are obtained by integration and fitting, respectively. The number of signal events beneath a gaussian, N_S. The number of background events inside the mass window, N_B. The minimal signal events needed to detect the resonance, N_S^{min}. The total efficiency inside a mass window, $\epsilon_{mrst(h-g)}$, and the minimum cross-section needed to detect the graviton, $(\sigma B)^{min}$. MRST(h-g) used as PDF.

μ (GeV)	$MW_{cteq5l}(GeV)$	N_S	N_B	N_S^{min}	ϵ_{cteq5l}	$(\sigma B)^{min}(fb)$
498.8	$\pm$12.37	9728 .1	848.1	145.6	0.5236	2.781
998.8	$\pm$19.57	324.6	54.1	36.8	0.4922	0.616
1500	$\pm$24.96	32.5	8.1	14.2	0.4283	0.332
1600	$\pm$27.05	23.1	6.0	12.3	0.4394	0.280
1700	$\pm$27.66	15.0	4.3	10.4	0.4041	0.257
1800	$\pm$29.05	10.8	3.0	10.0	0.4048	0.247
1900	$\pm$32.01	7.8	2.4	10.0	0.4041	0.247
2001	$\pm$29.36	5.3	1.5	10.0	0.3722	0.269
2101	$\pm$35.67	4.2	1.3	10.0	0.4000	0.250
2201	$\pm$31.83	2.9	0.9	10.0	0.3680	0.272

Table A.4: The mass windows (MW) for different masses, given by $\mu \pm 3\ \sigma_m$, where the background and signal events are obtained by integration and fitting, respectively The number of signal events beneath a gaussian, N_S. The number of background events inside the mass window, N_B. The minimal signal events needed to detect the resonance, N_S^{min}. The total efficiency inside a mass window, ϵ_{cteq5l}, and the minimum cross-section needed to detect the graviton, $(\sigma B)^{min}$. CTEQ5L used as PDF.

mG (GeV)	S	ΔN	ΔS	$\Delta\epsilon$
500	388.8	$\pm$186.3	$\pm$6.63	1.7%
1000	57.6	$\pm$2.9	$\pm$0.39	0.7%
1500	16.2	$\pm$0.4	$\pm$0.14	0.9%
1600	13.3	$\pm$0.3	$\pm$0.12	1.7%
1700	11.0	$\pm$0.1	$\pm$0.05	0.6%
1800	8.6	$\pm$0.4	$\pm$0.22	2.3%
1900	7.3	$\pm$0.1	$\pm$0.06	0.7%
2000	6.0	$\pm$0.4	$\pm$0.29	4.6%
2100	5.4	$\pm$0.1	$\pm$0.09	1.2%
2200	4.8	$\pm$0.4	$\pm$0.4	8.5%

Table A.5: The Significance, the error between the number of signal events obtained by fitting and counting, $\Delta N = |N_{count} - N_{fit}|$ and the resulting errors in significance $\Delta S = \frac{\Delta N}{N_B}$ and in the total efficiency due to fitting $\Delta\epsilon = \frac{\Delta N}{N_{count}}$. MRST(h-g) used as PDF.

mG (GeV)	S	ΔN	ΔS	$\Delta\epsilon$
500	334.1	$\pm$170.1	$\pm$5.84	1.8%
1000	44.1	$\pm$2.5	$\pm$0.34	0.8%
1500	11.4	$\pm$0.6	$\pm$0.21	1.9%
1600	9.4	$\pm$0.2	$\pm$0.08	0.7%
1700	7.2	$\pm$0.6	$\pm$0.29	3.7%
1800	6.2	$\pm$0.2	$\pm$0.12	1.7%
1900	5.0	$\pm$0.1	$\pm$0.07	1.3%
2000	4.3	$\pm$0.2	$\pm$0.16	3.5%
2100	3.7	$\pm$0.1	$\pm$0.09	2.1%
2200	3.1	$\pm$0.0	$\pm$0.00	0.8%

Table A.6: The Significance, the error between the number of signal events obtained by fitting and counting, $\Delta N = |N_{count} - N_{fit}|$ and the resulting errors in significance $\Delta S = \frac{\Delta N}{N_B}$ and in the total efficiency due to fitting $\Delta\epsilon = \frac{\Delta N}{N_{count}}$. CTEQ5L used as PDF